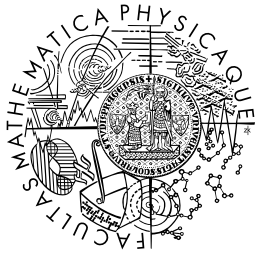

FACULTY
OF MATHEMATICS
AND PHYSICS
Charles University

DOCTORAL THESIS

Jan Premus

Joint inverse modeling of coseismic and postseismic slip of the 2014 South Napa, California, earthquake

Department of Geophysics

Supervisor of the doctoral thesis: prof. František Gallovič

Study programme: Physics

Study branch: Physics of the Earth and Planets

Prague 2023

I declare that I carried out this doctoral thesis independently, and only with the cited sources, literature and other professional sources. It has not been used to obtain another or the same degree.

I understand that my work relates to the rights and obligations under the Act No. 121/2000 Sb., the Copyright Act, as amended, in particular the fact that the Charles University has the right to conclude a license agreement on the use of this work as a school work pursuant to Section 60 subsection 1 of the Copyright Act.

In ..... date ....

Author's signature

First of all, I want to thank my supervisor prof. František Gallovič for his care, patience and erudity in guiding me during the whole Ph.D. (and Masters) adventure and being a diligent first reader and coauthor of both presented papers.

In addition to František, I want to thank my other coauthors, Alice-Agnes Gabriel, Ladislav Hanyk and Jean-Paul Ampuero, for many great inputs and corrections. I also want to thank Alice and Pablo for hosting me during my stays at LMU in Munich and Geoazur in Valbonne, respectively.

I greatly enjoyed my time at the Department of Geophysics and I am grateful to all the people there for creating a friendly and motivating environment filled with great science, stimulating discussions and regular coffee breaks. Special thanks belong to prof. Jiří Zahradník who introduced me to seismology and my fellow students Jakub, Franta, Libor, Martin, and Filip for being good friends both inside and outside of academia.

I am thankful to my family, my mum especially, for their long-term support during my studies and my girlfriend Maggie for being there for me during the months writing this manuscript.

My work was supported from several grants — Charles University Grant SVV n. 15-09/260447 and 115-009/260581 and Grant Agency of the Charles University (GAUK) n. 570120 and used data from several sources. Accelerometric data were downloaded from the freely available online repository, Center for Engineering Strong Motion Data (CESMD; `http://strongmotioncenter.org`). GPS data were downloaded from the freely available online repository, UNAVCO Geodetic Facility for the Advancement of Geosciences (GAGE; `www.unavco.org`). Locations of aftershocks were downloaded from the freely available online repository, Northern California Earthquake Data Center (NCEDC; `www.ncedc.org`)

Title: Joint inverse modeling of coseismic and postseismic slip of the 2014 South Napa, California, earthquake

Author: Jan Premus

Department: Department of Geophysics

Supervisor: prof. František Gallovič, Department of Geophysics

Abstract: Slip at tectonic faults spans a wide range of time scales, from tens of seconds of earthquake coseismic rupture to months of aseismic afterslip, recorded in seismograms and geodetic data. The two slip phenomena are often studied separately, focusing on kinematic aspects. We introduce a Bayesian method for physics-based joint inverse modeling of an earthquake slip and afterslip, employing a unifying rate-and-state friction law. To simulate the rupture propagation, we develop an efficient finite-difference open-source code FD3D_TSN. GPU acceleration of the code yields speed-up by a factor of 10 with respect to a CPU, enabling hundreds of thousands of earthquake simulations in a reasonable time. We also implement a quasi-dynamic afterslip simulation using a boundary integral element method. We apply the Bayesian dynamic inversion to the 2014 Mw 6.0 Napa earthquake. We reveal the dynamics of coseismic and postseismic slip in terms of stress and friction in a unified model, reconciling previous disjunctive analyses of the event. We show that the two types of slip are mostly spatially complementary in the sense that the postseismic slip occurs adjacent to the coseismic regions. Some velocity-strengthening areas that host the afterslip preferably are penetrated by the coseismic rupture, e.g., near the free surface and at depth. Particularly, the deep afterslip is accompanied by aftershocks. We also compare the inversion results with those obtained considering the classical slip-weakening friction law. We demonstrate that the coseismic models share many similarities, especially in the slip and stress drop spatial distribution. Importantly, we show that the joint coseismic and postseismic modeling in the rate-and-state framework better constrains even the coseismic rupture itself because the afterslip formation limits the position of the earthquake rupture.

Keywords: Dynamic earthquake source models, Postseismic slip modeling, Rate-and-state friction, Bayesian inversion

Název: Sdružené inverzní modelování koseismického a postseismického skluzu kalifornského zemětřesení South Napa 2014

Autor: Jan Premus

Katedra: Katedra geofyziky

Vedoucí dizertační práce: prof. František Gallovič, Katedra geofyziky

Abstrakt: Skluz na tektonických zlomech probíhá nejen krátkodobě v průběhu zemětřesení (tzv. koseismicky), ale i v dlouhodobějším měřítku ve formě postseismického dokluzu, jak dokumentují měření pomocí seismogramů a geodetických metod. Oba typy skluzu byly dosud modelovány většinou odděleně a navíc převážně kinematicky. Zde představujeme Bayesovskou metodu pro inverzní fyzikální modelování koseismického a postseismického skluzu, která využívá sjednocující zákon tření typu "rate-and-state". Vyvinuli jsme efektivní otevřený kód FD3D_TSN pro simulaci šíření zemětřesné trhliny metodou konečných diferencí. Využití GPU vede k až desetinásobnému zrychlení kódu oproti CPU, což umožňuje provést stovky tisíc simulací zemětřesení v rozumném čase. Implementovali jsme také kvazidynamickou simulaci dokluzu metodou hraničních prvků. Bayesovskou dynamickou inverzi jsme aplikovali na zemětřesení v kalifornské Napě z roku 2014 (Mw 6,0). Získaný sdružený model vysvětluje dynamiku koseismického a postseismického skluzu řízenou napětím a třením na zlomu a dává tak do souladu předchozí oddělené analýzy. Ukazujeme, že oba typy skluzu se většinou prostorově doplňují tak, že k postseismickému skluzu dochází na hranicích koseismických oblastí. V některých případech koseismická trhlina proniká i do postseismických oblastí, např. v blízkosti volného povrchu a v hloubce. Dokluz v hloubce je pak doprovázen dotřesy. Výsledky modelování také porovnáváme s výsledky inverze s klasickým zákonem tření typu ¨slip-weakening¨. Ukazujeme, že oba koseismické modely mají mnoho společných rysů, a to zejména v prostorovém rozložení skluzu a poklesu napětí. Ukazujeme, že důležitou výhodou sdruženého modelování s ¨rate-and-state¨ třením je zpřesnění samotné koseismické trhliny, jejíž prostorový výskyt je limitována vznikem dokluzu.

Klíčová slova: Dynamic earthquake source models, Postseismic slip modeling, Rate-and-state friction, Bayesian inversion

Contents

1. Introduction

Tectonic faults occur in the Earth's crust as a brittle response to the elastic accumulation of stress, usually at boundaries between tectonic plates. Accumulated stress releases in the form of slip — the mutual movement of both sides of the fault.

Slip can unfold continuously over many decades on the so-called creeping segments of the faults [Harris, 2017]. On other parts of the faults, slip takes place over a wide range of temporal scales, from sub-second to minute scale of seismic slip during earthquakes, up to months and years of aseismic slip [Smith and Wyss, 1968, Marone et al., 1991, Perfettini and Avouac, 2004]. The concept of the tectonic loading of stress, and its release through quasiperiodic earthquakes and aseismic slip is known as the seismic cycle [Perfettini et al., 2003, Hillers et al., 2006, Perfettini and Avouac, 2014, Bunichiro et al., 2019].

Faulting is prominent in the Earth's crust, constrained roughly to maximum depths of 20–50 km as high temperatures at larger depths preclude brittle fracture in favor of viscoelasticity and plasticity [Scholz, 1998]. Exceptions are the intermediate and deep earthquakes that can occur in the colder material of subducted slabs at depths of up to 700 km [Frohlich, 2006].

As the stress preferably releases on preexisting faults, the occurrence of slip is considered to be a more frictional than fracturing phenomenon [Brace and Byerlee, 1966, Scholz, 1998]. Fracture mechanics plays a supporting role mostly during the extension of the existing faults [Cowie and Scholz, 1992], the creation of new ones, or the damage of surrounding material [Yamashita, 2000, Okubo et al., 2019]. Two empirical models of friction are prominent in the seismological community. Slip-weakening friction laws [Andrews, 1976] describe the basic behavior of friction decrease from static to dynamic value during the slipping and is thus suitable for earthquake modeling. It cannot be used to explain the behavior of aseismic slip, or strength recovery during the interseismic phase. Rate-and-state friction models [Dieterich, 1972, Ruina, 1983] encompass these phenomena, with an elegant explanation of the seismic and aseismic slip dichotomy through velocity-weakening and velocity-strengthening frictional rheology. Quasiperiodic occurrence of earthquakes has an analog in simple stick-slip models [Brace and Byerlee, 1966] where the string-pulled object on the velocity-weakening contact alternates between periods of fast slip and longer periods of movement cessation.

Aside from elasticity and friction, additional physical phenomena can occur at faults with varying influence on slip. Rheology of the material can be partially plastic [Dunham et al., 2011, Wollherr et al., 2018], or altered by the damage from earthquakes. Faults also often occur on bi-material interfaces [Dunham and Rice, 2008]. Various thermal effects can contribute to fault weakening, such as temperature-driven changes in frictional rheology [Bizzarri, 2009], flash heating of contacts [Rice, 2006], pore-water pressurization [Rice, 2006], or even contact melting [Nielsen et al., 2008]. Fluid pressure can be further affected by slip-induced changes in porosity and permeability [Bizzarri and Cocco, 2006] and friction can decrease due to lubrication of the fault by gauge [Sammis and Ben-Zion, 2008, Goldsby and Tullis, 2011]. Additionally, complex fault geometry including segmentation [Ulrich et al., 2019, Tinti et al., 2021], or roughness [Shi

and Day, 2013] may impact the slip behavior.

Experimental research of frictional, fracture, or other mechanisms is limited by the spatial scale achievable in laboratory [Viesca and Garagash, 2015]. The typical size of samples in frictional experiments is measured in centimeters to meters [Dieterich, 1979, Latour et al., 2013, Rubino et al., 2017], while the faults in nature span up to tens to hundreds of kilometers. Nevertheless, laboratory experiments led to important advancements, such as the discovery of contact fast-weakening due to flash-heating [Di Toro et al., 2004], which is thought to preclude the complete melting of fault contacts during the earthquake, observed only rarely [Rice, 2006].

Earthquake science is becoming increasingly data-rich, given the increasing number of installed seismic and geodetic stations [Storchak et al., 2020] and the advent of emerging technologies, such as remote sensing [Lohman et al., 2002] or distributed acoustic sensing [Daley et al., 2013]. These observations are limited to the surface effects of burried fault phenomena in the form of ground motions or surface displacements. Direct measurements on active faults are usually inaccessible, with only a few technically difficult exceptions, such as drilling into the fault [Fulton et al., 2019]. Consequent difficulties in discerning relative importance of various physical phenomena is the substantive reason for earthquake science remaining relatively model-poor [Lapusta et al., 2019].

Physics-based dynamic rupture modeling provides a bridge between the small scales of laboratory experiments and the large scales of earthquake observations. It assimilates the results of experimental studies into complex computer simulations, where the slip propagates on pre-existing faults, governed by internal stresses and friction on the fault. This facilitates parametric numerical experiments [e.g., Kaneko et al., 2008, Gabriel et al., 2012, Bai and Ampuero, 2017], or modeling of specific events [e.g., Peyrat et al., 2001, Ando and Kaneko, 2018, Gallovič et al., 2020, Tinti et al., 2021].

Fitting data that carry information about the faulting process is a strongly nonlinear problem termed dynamic earthquake source inversion [Fukuyama and Mikumo, 1993]. For a specific earthquake, the dynamic model is parametrized by the spatial distribution of initial stress and frictional parameters, collectively referred to as dynamic parameters. These parameters are then optimized to minimize the misfit between synthetic and real data. Only a handful of earthquake dynamic inversions were performed [Peyrat and Olsen, 2004, Corish et al., 2007, Ruiz and Madariaga, 2013, Twardzik et al., 2014, Kostka et al., 2022, Gallovič et al., 2019a], all employing slip-weakening friction. The employment of more realistic rate-and-state friction laws in dynamic source inversions is yet to be properly explored.

1.1 State-of-the-art

1.1.1 Kinematic modeling of earthquake source

Mutual movement of tectonic plates is accommodated at faults by the propagation of slip (discontinuity of the displacement), which acts as a source of both static and dynamic parts of the seismic waves we observe. Relationship between stress

and strain is based on the conservation of momentum equation:

$$\rho \frac{\partial^2 u_i}{\partial t^2} = \sigma_{ij,j} + f_i, \tag{1.1}$$

where u_i, σ_{ij}, and f_i are components of the displacement vector, stress tensor, and volumetric forces, respectively. We denote partial derivative with respect to x_i by $,i$ in the lower index. We use Einstein summation rule for index j. For small deformations, we assume that the material of the crust acts as linearly elastic solid, following Hooke's law:

$$\sigma_{ij} = c_{ijkl} e_{kl}, \tag{1.2}$$

where $e_{kl} = 1/2(u_{k,l} + u_{l,k})$ is the strain tensor, and stiffness tensor c_{ijkl} contains the elastic paramters. For isotropic material, the stiffness tensor contains only two independent parameters:

$$c_{ijkl} = \lambda \delta_{ij} \delta_{kl} + \mu(\delta_{ik}\delta_{jl} + \delta_{il}\delta_{jk}), \tag{1.3}$$

called Lame's parameters λ and μ (shear modulus). Kombination of the conservation of momentum law (Equation 1.1) and Hooke's law (Equation 1.2) is referred to as the elastodynamic equation.

Suppose that force f_i is specified as a Dirac delta function in space and time, in a form of a unidirectional impulse in the direction of the p-th Cartesian coordinate axis. The solution of the elastodynamic equation, describing the material response to this unit source, is called the Green's tensor G_{ip}. Solutions for more complicated sources such as earthquakes can be acquired using the representation theorem [Aki and Richards, 2002]:

$$u_i(\vec{x}, t) = \iint_\Sigma m_{pq}(\vec{\xi}, t) * G_{ip,q}(\vec{x}, \vec{\xi}, t) d\Sigma, \tag{1.4}$$

i.e., as an integral of the time convolution of moment tensor density m_{pq} with partial derivatives of the Green's tensor G_{ip} with respect to q-th coordinate over the fault surface Σ. Moment tensor density for a pure shear slip reads

$$m_{pq}(\vec{\xi}, t) = \mu(\vec{\xi}) \Big[s_p(\vec{\xi}, t) n_q(\vec{\xi}) + n_p(\vec{\xi}) s_q(\vec{\xi}, t) \Big], \tag{1.5}$$

where $\vec{s}$ is the fault slip and $\vec{n}$ fault normal unit vector. Green's tensor can be calculated analytically or numerically for different distributions of the Lame's parameters and density in the domain. Semianalytical solution for a material constituting of homogenous layers is frequently used to model the propagation of waves through the Earth's crust [Cotton and Coutant, 1997].

Kinematic models of the earthquake source describe the spatio-temporal distribution of slip $\vec{s}(t, \vec{\xi})$ on the fault. With the exception of simple analytical problems, the modeling is usually done numerically. Numerical implementations are based on the discretization of the fault into many sub-sources. Ground motions can then be calculated as a superposition of the seismograms generated by the sub-sources, due to the additivity of the spatial integral in Equation 1.4. If the size of the sub-source is small enough to satisfy the point-source approximation [Aki and Richards, 2002], only its mean slip function and Green's tensor are sufficient to model its ground motions. The temporal convolution in the sub-source can be also discretized into a sum.

The major shortcoming of the kinematic modeling is the lack of physics of the earthquake source — the physical reason for the slip to occur. Nevertheless, they are still very useful for modeling the seismic wavefield, including its various source-related features such as directivity [Haskell, 1964], or for scenario modeling for seismic hazard applications [e.g., Cultrera et al., 2010], or imaging the slip distribution by solving the kinematic inverse problem [e.g., Wald et al., 1996, Gallovič and Zahradník, 2012].

1.1.2 Dynamic modeling of earthquake source

Dynamic models include two essential ingredients describing the propagation of stress along the fault and the constitutive relation at the fault. Classical dynamic models are embedded in a three-dimensional domain where the evolution of stress and displacement is governed by the elastodynamic equation. We assume the distribution of the material parameters and the position of the fault to be known. The fault is modeled as a surface boundary, where we prescribe the constitutive relation in the form of a friction law, placing the limit on traction. After nucleation [Bizzarri, 2010], the seismic rupture expands spontaneously over the fault. We obtain both the spatio-temporal distribution of slip and ground motions as a part of the solution.

The mathematical formulation of this problem leads to a set of partial differential equations for stress and displacement with mixed boundary conditions on the fault, parametrized by the distribution of initial stresses and frictional parameters. Dynamic models usually require a numerical solution [Andrews, 1976, Das and Aki, 1977, Graves, 1996, Madariaga et al., 1998], with the exception of very simplified models [e.g., Kostrov, 1966].

To maintain a manageable mathematical complexity, the above-presented model contains a series of approximations and assumptions. Confinement of the slip to a pre-set surface is a simplification of the reality where slip is accommodated in fault zones of non-zero thickness [Sibson, 2003]. Also, the damage of material during the earthquake can cause the creation of new fault cracks, or extensions of existing ones [Preuss et al., 2019]. Linear elasticity of the surrounding material is also an approximation because high-stress fields around the rupture tip should onset the plasticity [Dunham et al., 2011]. Additionally, besides dry friction, there is a number of physical phenomena with potential impact on the rupture propagation. We assume the friction laws grasp all major features of the stress evolution during the earthquake and consider their parameters as effective, encompassing the impact of all additional phenomena. Nevertheless, constraining slip and slip-rate by the physical laws represents a major advancement to the kinematic models.

1.1.3 Earthquake source inversions

Inverse modeling of earthquakes inferes parameters of an earthquake model from a set of observations. It encompasses a forward model (kinematic or dynamic), parametrization, and an inversion procedure that optimizes the model parameters to minimize a misfit function. Typical choices of the misfit function involve the L^2 norm of the difference between observed and synthetic data [e.g., Spudich and

Miller, 1990], or their crosscorrelation [e.g., Díaz-Mojica et al., 2014].

Kinematic inverse problems are non-unique, as different spatial and temporal combinations of fault slip (some of them potentially physically unrealistic) can generate the same seismograms [Gallovič and Ampuero, 2015, Shao and Ji, 2012]. There is a large number of kinematic source inversion methods employing various parametrizations of the fault slip, additional constraints and regularizations [see, e.g., Mai et al., 2016]. Linear kinematic inversions [Das and Kostrov, 1994, Delouis et al., 2002, Hartzell et al., 2007, Gallovič et al., 2015] use the discretized distribution of slip rate as model parameters, while nonlinear kinematic inversions prescribe a priori shape of rupture propagation inspired by the general earthquake knowledge [Vallée and Bouchon, 2004, Monelli et al., 2009, Gallovič and Zahradník, 2012], or knowledge from dynamic modeling [Guatteri et al., 2004, Tinti et al., 2005]. Postseismic slip is also studied kinematically, powered by the spread of GPS monitoring and satellite imaging [Twardzik et al., 2019, Caballero et al., 2021, Ragon et al., 2019, Liu and Xu, 2019].

We can get clues about the dynamic model from the results of kinematic inversion, as they provide us with the relationship between slip and stress change [Bouchon, 1997, Ide and Takeo, 1997, Piatanesi et al., 2004, Burjánek and Zahradník, 2007]. Frictional parameters can then be estimated from the evolution of stress, usually for the case of the slip-weakening friction [Tinti et al., 2005]. The resolution of this approach is limited, due to the low temporal resolution of the kinematic inversions [Piatanesi et al., 2004]. The parameters of rate-and-state friction in aseismically slipping ares can be also constrained from postseismic modeling [Twardzik et al., 2021].

Dynamic inversions infer the parameters of the dynamic model from the recorded data directly. So far, only a few attempts have been made due to the high computational burden, driven by the computational severity of the forward model, nonlinear nature of the inversion, and high amount of model parameters [e.g., Fukuyama and Mikumo, 1993]. Several ways to decrease the number of model parameters was explored, such as constraining the shape of the rupture [Ruiz and Madariaga, 2013, Twardzik et al., 2014, Kostka et al., 2022], or keeping some of the dynamic parameters constant [Corish et al., 2007, Peyrat and Olsen, 2004]. Joint dynamic inversion of seismic and aseismic slip has not yet been performed because all inversions employed the slip-weakening friction law only and the modeling across such wide time scales represents a significant challenge.

As the complexity of the source model and the number of model parameters increases, inconsistency and non-uniqueness of the problem gains importance. Coupled with the measuring error in the data set and uncertainty of the velocity model, confining to a single solution of the inversion may lead to biased conclusions. Bayesian framework represents a preferable probabilistic approach. It treats the inversion as an update of prior distributions of model parameters under the constraints provided by observed data and other acquired knowledge. We can then sample the resulting posterior probability density function of model parameters by, e.g., a Markov Chain Monte Carlo algorithm, yielding a discretized set of models. The Bayesian approach was already applied to kinematic inversions [e.g., Sambridge and Mosegaard, 2002, Monelli and Mai, 2008, Duputel et al., 2015, Hallo et al., 2017].

Recently, Gallovič et al. [2019a] introduced a Bayesian method to constrain

fault friction parameters and stress conditions that controlled earthquake rupture. The method was successfully applied to the 2016 Amatrice [Gallovič et al., 2019b] and 2020 Elazığ [Gallovič et al., 2020] earthquakes. In this approach, efficient finite-difference dynamic rupture simulations with the slip-weakening friction law are combined with the parallel tempering Monte Carlo algorithm. Sampling the posterior probability density function in this method requires hundreds of thousands to millions of the dynamic simulations.

1.2 Content of the Thesis

This thesis expands the scope of the dynamic inversion beyond the coseismic rupture and perform the first joint physics-based inverse modeling of an earthquake with its afterslip. The 2014 Napa earthquake offers a perfect case study for the new approach due to the wealth of available recordings of both coseismic and postseismic slip that significantly contributed to the released energy and damage caused to human structures.

We utilize a state-of-the-art laboratory-derived rate-and-state friction law with enhanced fast-velocity-weakening representing a unifying physical framework to capture both the co- and postseismic slip. To this aim, we introduce an efficient finite-difference code FD3D_TSN with GPU acceleration. Our Bayesian inverse modeling is constrained by multiple datasets on diverse timescales from seconds (seismograms and coseismic GPS) to months (postseismic GPS and alignment fields across the surface rupture).

In addition, we compare the results with the dynamic inversion of the same earthquake, which employs the slip-weakening friction law. This allows us to make comparisons between the friction models, determine which properties of the dynamic models are affected by the choice of the friction law, and demonstrate the usefulness of the expansion to postseismic modeling even for constraining the coseismic phase.

The structure of this Thesis is as follows. **Chapter 2** concerns the development of the finite difference code FD3D_TSN. We demonstrate good agreement with other methods in four benchmark exercises from the Southern California Earthquake Center and U.S. Geological Survey dynamic rupture code verification project [Harris et al., 2018]. Additionally, we describe the quasidynamic model used for the modeling of the afterslip. The majority of this chapter was published as Premus et al. [2020] in Seismological Research Letters.

Chapter 3 presents the results of the joint dynamic inversion of the 2014 Napa earthquake and its afterslip, employing the rate-and-state fast-velocity-weakening friction. The chapter was published as Premus et al. [2022] in Science Advances.

Chapter 4 compares the results from the dynamic inversion in Chapter 3 with the results of the dynamic inversion of the same earthquake but employing slip-weakening friction.

Chapter 5 provides conclusions to this Thesis.

2. Dynamic and quasidynamic simulations of earthquake rupture

Majority of this chapter was published as [Premus et al., 2020] in Seismological Research Letters. Minor corrections, including notational and stylistic edits, were made and Section 2.7 about quasidynamic modeling was added.

2.1 Introduction

Earthquakes are caused by the sudden release of accumulated elastic strain energy. Rupture propagates as a discontinuity on a pre-existing fault surface, governed by prestress and friction. The mathematical description of a so-called dynamic rupture model leads to a nonlinear mixed-boundary problem. Although some simple models of rupture propagating at prescribed speeds in 2D have analytical solutions available in closed forms [Kostrov, 1964, Aki and Richards, 2002], more complex models accounting for spontaneous propagation of the rupture require a numerical solver.

Dynamic rupture simulations have been undergoing rapid development in the past decades, starting with finite difference (FD) [e.g., Andrews, 1976, Madariaga, 1976, Mikumo and Miyatake, 1978, Day, 1982] and boundary integral [e.g., Burridge, 1969, Das, 1980, Koller et al., 1992] methods. Later, finite element [e.g., Oglesby et al., 1998, Barall, 2006], spectral element [e.g., Festa and Vilotte, 2005, Kaneko et al., 2008], and discontinuous Galerkin[de la Puente et al., 2009, Pelties et al., 2012, Tago et al., 2012] methods were developed.

Empowered by supercomputing [e.g., Heinecke et al., 2014, Ichimura et al., 2014, Uphoff et al., 2017], 3D dynamic rupture earthquake simulation software has reached the capability of accounting for increasingly complex geometrical [e.g., Ulrich et al., 2019] and physical [e.g., Roten et al., 2014, 2016, Wollherr et al., 2019]) modeling components in high-resolution single-event scenarios. Yet, the computational cost of such dynamic rupture models hinders applications requiring a large number of simulations.

Inverting strong ground motions using dynamic source models is challenging due to the nonlinear relationship between source parameters (prestress and parameters of the friction law) and seismograms. Typical numbers of required trial models are then hundreds of thousands to millions [Gallovič et al., 2019a, Mirwald et al., 2019]. Similarly, high numbers of simulations are needed in physics-based scenario ground-motion modeling or parametric studies in general [e.g., Peyrat et al., 2001, Cui et al., 2013]. Particular examples are seismic cycle simulations that span periods of thousands of years, generating synthetic catalogs of earthquakes [Erickson et al., 2020]. To enable such applications, the computational requirements of the forward simulation have to be reduced not only by simplifying the physical model of the fault and the surrounding medium but also using efficient numerical methods such as presented here. Having simplified and fast rupture dynamics software [Daub, 2016, Krischer et al., 2018] is also useful for

teaching and training purposes and allows the first acquaintance with dynamic rupture simulations. Such codes can be utilized by all researchers interested in earthquake physics even without immediate access to supercomputing power required by the most advanced codes.

The FD operators in FD3D_TSN are adapted and extended from the 3D FD code FD3D by R. Madariaga [Madariaga et al., 1998]. They utilize regular cubic grids, and are relatively simple and computationally efficient [Levander, 1988]. Their use leads to a high speed of the calculation and is allowed by considering a simple fault geometry. Discontinuous velocity components at the fault are antisymmetric, allowing for the simplification of the fault boundary condition. Consequently, only one side of the fault needs to be calculated, cutting the required computational capacities (central processing unit [CPU] time and memory storage) in half. The major factor influencing the accuracy of FD3D_TSN is the here used implementation of the fault boundary condition. We use the traction-at-split-node approach [Dalguer and Day, 2007], which leads to an accuracy comparable with other codes.

Although many rupture propagation codes provide parallelization using OpenMP and Message Passing Interface (MPI), graphic processing units (GPU) acceleration is gaining attention only recently. GPU acceleration of wave propagation codes using FD and finite-element methods was implemented by Michéa and Komatitsch [2010] and Komatitsch et al. [2009] using Compute Unified Device Architecture (CUDA). CUDA is also featured by the publicly available spectral element code SPECFEM3D [Komatitsch et al., 2010] and the FD code AWP-ODC [Zhou et al., 2013]. The RAJA library is used to accelerate the SW4 code [Rodgers et al., 2019].

To foster the GPU acceleration in the field of rupture dynamics, we utilize the easy-to-use OpenACC approach to optionally port the code to GPUs. We demonstrate that the speed-up can be significant, by one order of magnitude when using commonly available GPUs. We note that OpenACC, in comparison to the CUDA framework, allows also for non-Nvidia accelerator support, whichwill become increasingly important as demonstrated by future U.S. exascale machines relying on AMD GPU accelerators.

The present article introduces the main ingredients of FD3D_TSN, namely the FD method and implementation of boundary conditions. We describe the GPU acceleration of the code using OpenACC directives. Then, we perform verification exercises using benchmarks from the Southern California Earthquake Center and U.S. Geological Survey (SCEC/USGS) Spontaneous Rupture Code Verification Project [Harris et al., 2018]. We show that our results are on par with those of other codes and compare the wall clock times of the serial (one core) baseline and GPU-accelerated versions of our code. The code FD3D_TSN is freely available at `https://github.com/JanPremus/fd3d_TSN`, together with a detailed method description and examples.

2.2 Method

Essential ingredients of a dynamic earthquake simulation code are: (1) discrete solver of the elastodynamic equation, (2) implementation of physical boundary conditions (fault and free surface), and (3) nonreflecting (artificial) boundaries

simulating the free flow of energy outside of the computational domain.

The free surface is implemented using the stress imaging technique[Graves, 1996] at the upper boundary of the computational domain. Perfectly matched layers (PMLs; Berenger [1994]) in a classical split form [Kristek et al., 2009] are placed at the remaining borders as artificial absorbing conditions.

The free surface can be optionally turned off and replaced by an absorbing boundary when, for example, a deep event is to be simulated. Although the PMLs are more demanding in terms of both computational power and memory storage, the absence of reflections for a wide range of incidence angles permits a significant reduction of the size of the computational domain in practical applications.

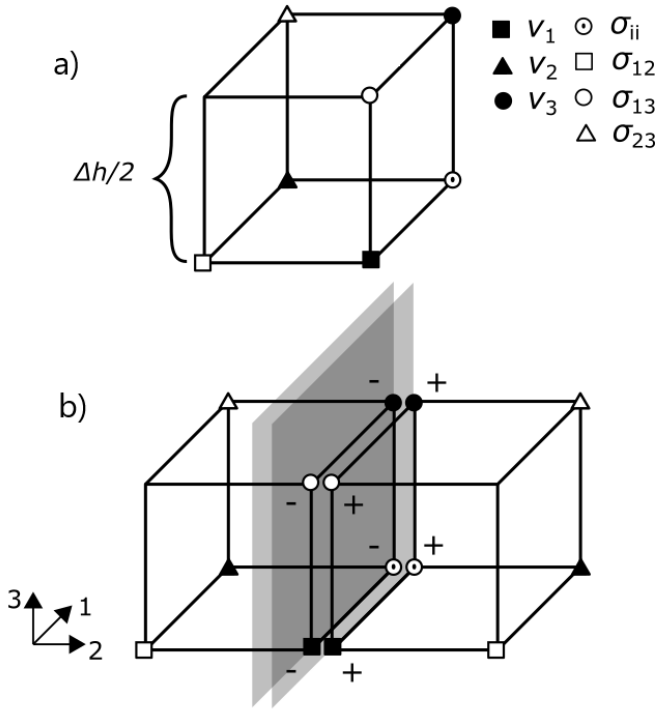

Figure 2.1: (a) Finite-difference (FD) grid cube with staggered positions of components of velocity v and stress σ (symbols). (b) Position of the fault in the staggered grid. The fault (gray plane) overlays with one of the grid planes. Discontinuous components of velocity and stress are treated separately for their '-' and '+' side.

2.2.1 Discretization of the elastodynamic equation

FD3D_TSN solves the elastodynamic equation in the classical velocity–stress formulation, with a derivative of Hook's law with respect to time:

$$\rho \frac{\partial v_i}{\partial t} = \sigma_{ij,j}, \tag{2.1}$$

$$\frac{\partial \sigma_{ij}}{\partial t} = c_{ijkl} \frac{1}{2}(v_{k,l} + v_{l,k}), \tag{2.2}$$

where v denotes the particle velocity.

Central FD operators of the fourth-order in space [Levander, 1988, Madariaga et al., 1998] are used to discretize the elastodynamic equation on a 3D-staggered regular grid, see Figure 2.1a for the respective positions of the components of velocity and stress in a grid cell. FD formulas of the second order read [Moczo et al., 2007]:

$$(D_1^{(2)}\phi)_{I,J,K} = \left[\phi_{I^{\frac{1}{2}},J,K} - \phi_{I^{-\frac{1}{2}},J,K}\right]/\Delta h \tag{2.3}$$

$$(D_2^{(2)}\phi)_{I,J,K} = \left[\phi_{I,J^{\frac{1}{2}},K} - \phi_{I,J^{-\frac{1}{2}},K}\right]/\Delta h \tag{2.4}$$

$$(D_3^{(2)}\phi)_{I,J,K} = \left[\phi_{I,J,K^{\frac{1}{2}}} - \phi_{I,J,K^{-\frac{1}{2}}}\right]/\Delta h. \tag{2.5}$$

And FD formulas of the fourth order read:

$$(D_1^{(4)}\phi)_{I,J,K} = \left[\frac{9}{8}(\phi_{I^{\frac{1}{2}},J,K} - \phi_{I^{-\frac{1}{2}},J,K}) - \frac{1}{24}(\phi_{I^{\frac{3}{2}},J,K} - \phi_{I^{-\frac{3}{2}},J,K})\right]/\Delta h \tag{2.6}$$

$$(D_2^{(4)}\phi)_{I,J,K} = \left[\frac{9}{8}(\phi_{I,J^{\frac{1}{2}},K} - \phi_{I,J^{-\frac{1}{2}},K}) - \frac{1}{24}(\phi_{I,J^{\frac{3}{2}},K} - \phi_{I,J^{-\frac{3}{2}},K})\right]/\Delta h \tag{2.7}$$

$$(D_3^{(4)}\phi)_{I,J,K} = \left[\frac{9}{8}(\phi_{I,J,K^{\frac{1}{2}}} - \phi_{I,J,K^{-\frac{1}{2}}}) - \frac{1}{24}(\phi_{I,J,K^{\frac{3}{2}}} - \phi_{I,J,K^{-\frac{3}{2}}})\right]/\Delta h, \tag{2.8}$$

where ϕ denotes any components of velocity or stress. Indexes I, J, K denote the position of the node in the grid. For convenience, we use I^J instead of $I + J$ to express the complicated indexes. The addition of $1/2$ in the index marks a position moved by $\Delta h/2$ in the given direction. The partial difference is calculated with respect to the axis component given by the lower index (1 for x, etc.). We use the second-order central FD formula to discretize the partial derivative with respect to time:

$$(D_t\phi)_{I,J,K}^{N^{\frac{1}{2}}} = \left[\phi_{I,J,K}^{N} - \phi_{I,J,K}^{N^{-1}}\right]/\Delta t. \tag{2.9}$$

2.2.2 Fault boundary condition

Frictional boundary conditions at the fault surface are implemented using the traction-at-split-node method [Dalguer and Day, 2007], assuming a general 2D slip vector. We consider the same material parameters on both sides of the fault and only the vertical planar fault, dividing the modeling domain into two half-spaces, denoted as $'+'$ and $'-'$ as in Figure 2.2. This simplifies the governing traction-at-split-node equations because discontinuous velocity v_i and stress σ_{ij} components are antisymmetric, whereas the continuous ones are symmetric across the fault. For vertical fault in the plane along the 1 and 3 axes, this reads:

$$v_1^+ = -v_1^- \qquad v_2^+ = +v_2^- \qquad v_3^+ = -v_3^- \tag{2.10}$$

$$\sigma_{11}^+ = -\sigma_{11}^- \qquad \sigma_{22}^+ = \sigma_{22}^- \qquad \sigma_{33}^+ = -\sigma_{33}^- \tag{2.11}$$

$$\sigma_{12}^+ = +\sigma_{12}^- \qquad \sigma_{13}^+ = -\sigma_{13}^- \qquad \sigma_{23}^+ = +\sigma_{23}^- \tag{2.12}$$

Moreover, the wave-propagation FD operators can be calculated on one side of the fault only, which cuts the computational and memory demands of solving the problem in half.

We define the i-th components of slip s_i and slip rate $\dot{s}_i$ as an across-fault discontinuities in the displacement u_i and velocity v_i, respectively:

$$s_i(\vec{x},t) = u_i^+(\vec{x},t) - u_i^-(\vec{x},t), \tag{2.13}$$

$$\dot{s}_i(\vec{x},t) = v_i^+(\vec{x},t) - v_i^-(\vec{x},t). \tag{2.14}$$

We will denote absolute values of slip and slip rate as s and $\dot{s}$, respectively.

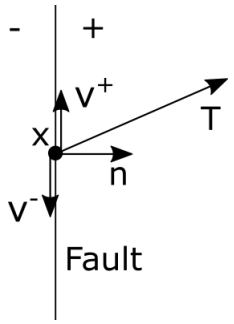

Figure 2.2: Schematic of the fault variables at point $\vec{x}$: normal to the fault n_i, discontinuous velocity v_i^+ and v_i^-, and continuous traction T_i.

Let $\vec{n}$ be a unit fault-normal vector pointing into the '+' half-space. We assume only shear faulting, normal components of displacement u_i^n and velocity v_i^n are thus continuous:

$$0 = u_i^{n+}(\vec{x},t) - u_i^{n-}(\vec{x},t), \tag{2.15}$$

$$0 = v_i^{n+}(\vec{x},t) - v_i^{n-}(\vec{x},t). \tag{2.16}$$

We denote i-th component of traction as $T_i(\vec{x},\vec{n},t) = \sigma_{ij}n_j$, which is continuous across the fault. Fault boundary consists of two conditions on shear traction $T^s(\vec{x},\vec{n},t)$, bounded by the frictional strength $S(\vec{x},t)$ and colinear with slip rate $\dot{s}_i(\vec{x},t)$:

$$T^s(\vec{x},t) \leq S(\vec{x},t). \tag{2.17}$$

$$T_i^s(\vec{x},t)\dot{s}(\vec{x},t) - S(\vec{x},t)\dot{s}_i(\vec{x},t) = 0. \tag{2.18}$$

2.2.3 Traction-at-split-node implementation

First, we provide the traction-at-split-node implementation, assuming all components of velocity and stress are read in the same node. Concrete application, using a specific staggered grid scheme, is then described in the second half of the section.

Every node on the fault plane belongs to both half-spaces $'+'$ and $'-'$. To accommodate the discontinuity of certain variables in these nodes, each fault node is split into two split nodes, where the velocity and stress components are defined separately and denoted by $'+'$ and $'-'$ signs. The mass of the split node is calculated as $M^{\pm} = \Delta h^3 \rho^{\pm}/2$ because the fault is cutting the FD 'cube' (with side length Δh) in half. Traction T_i is continuous across-fault and is therefore the same for both split nodes.

Acceleration at both '+' and '-' split nodes is given by the Newton's 2nd law:

$$\frac{\partial v_i^{\pm}}{\partial t} = (f_i^{\pm} \mp f_i^c)/M^{\pm}, \tag{2.19}$$

where $f_i^{\pm}$ and f_i^c denotes components of body and surface forces, respectively. Body force is equal to the right-hand side of the elastodynamic equation:

$$f_i^{\pm} = \sigma_{ij,j}. \tag{2.20}$$

Surface force f_i^c is calculated from the across-fault continuous traction T_i. This force is of the same magnitude for both split nodes, but of opposite orientation. For the $'-'$ side, it yields

$$f_i^c = \Delta h^2 (T_i - T_i^0), \tag{2.21}$$

where T_i^0 is traction at the initial state of equilibrium.

Acceleration is introduced into the FD equations as the right-hand side of the updating scheme for the velocity components at the fault plane

$$(v_i^{\pm})^{N^1} = (v_i^{\pm})^N + \Delta t \left[(f_i^{\pm})^{N^{\frac{1}{2}}} \mp \Delta h^2 \left((T_i)^{N^{\frac{1}{2}}} - T_i^0 \right) \right] / M^{\pm}. \tag{2.22}$$

The slip rate is calculated from (2.14), as a difference between the velocity values in both split nodes using (2.22). Minor algebra with the terms leads to:

$$(\dot{s}_i)^{N^1} = (\dot{s}_i)^N + \frac{\Delta t\,(M^- + M^+)}{\Delta h^{-2} M^- M^+} \left[\frac{M^-(f_i^+)^{N^{\frac{1}{2}}} - M^+(f_i^-)^{N^{\frac{1}{2}}}}{\Delta h^2 (M^- + M^+)} + (T_i)^{N^{\frac{1}{2}}} - T_i^0 \right]. \tag{2.23}$$

We define trial traction T_i^T as traction when $(\dot{s}_i)^{N^1} = 0$, we express it from Equation 2.23:

$$(T_i^T)^{N^{\frac{1}{2}}} = T_i^0 + \frac{\Delta t^{-1} M^- M^+ (\dot{s}_i)^N + M^-(f_i^+)^{N^{\frac{1}{2}}} - M^+(f_i^-)^{N^{\frac{1}{2}}}}{\Delta h^2 (M^- + M^+)}. \tag{2.24}$$

We can use the trial traction to get the value of the slip-rate in the slipping case by calculating the difference between Equation 2.23 in slipping and non-slipping case:

$$(\dot{s}_i)^{N^1} = \Delta t \frac{\Delta h^2 (M^- + M^+)}{M^- M^+} \left((T_i)^{N^{\frac{1}{2}}} - (T_i^T)^{N^{\frac{1}{2}}} \right). \tag{2.25}$$

Slip-rate is therefore proportional to the difference between trial traction $(T_i^T)^{N^{\frac{1}{2}}}$ and traction $(T_i)^{N^{\frac{1}{2}}}$.

Slip occurs and $(\dot{s})^{n^1} \neq 0$ when the value of the trial shear traction $(T^T)^{N^{\frac{1}{2}}}$ is higher than frictional force $S^{N^{\frac{1}{2}}}$. The value of the shear traction is then set by the conditions (2.15) and (2.16). For the assumed vertical planar fault in the plane along the 1 and 3 axes, the normal component of the trial traction is $(T_2^T)^{N^{\frac{1}{2}}}$, while $(T_1^T)^{N^{\frac{1}{2}}}$ and $(T_3^T)^{N^{\frac{1}{2}}}$ are shear components.

We formulate the collinearity condition from Equation 2.18 for time staggered positions of slip rate $((N + \frac{1}{2})\Delta t)$ and traction $((N + 1)\Delta t)$:

$$(T_i)^{N^{\frac{1}{2}}} \dot{s}^{N^1} - S^{N^{\frac{1}{2}}} (\dot{s}_i)^{N^1} = 0, \tag{2.26}$$

because introducing interpolations can create numerical complications. Inserting Equation 2.25 into Equation 2.26 ties the value of traction with frictional force $S^{N\frac{1}{2}}$:

$$\left(S^{N\frac{1}{2}} + (T)^{N\frac{1}{2}} - (T^T)^{N\frac{1}{2}}\right)(T_i)^{N\frac{1}{2}} = S^{N\frac{1}{2}}(T_i^T)^{N\frac{1}{2}}. \tag{2.27}$$

Expressing the traction

$$(T_i)^{N\frac{1}{2}} = S^{N\frac{1}{2}}\frac{(T_i^T)^{N\frac{1}{2}}}{(T^T)^{N\frac{1}{2}}} \tag{2.28}$$

shows that its value is equal to friction and direction to the direction of trial traction. To finalize, we put together the equations from both slipping and non-slipping cases:

$$(T_i)^{N\frac{1}{2}} = \begin{cases} (T_i^T)^{N\frac{1}{2}}, & \text{if } (T^T)^{N\frac{1}{2}} \leq S^{N\frac{1}{2}} \\ S^{N\frac{1}{2}}\frac{(T_i^T)^{N\frac{1}{2}}}{(T^T)^{N\frac{1}{2}}}, & \text{if } (T^T)^{N\frac{1}{2}} > S^{N\frac{1}{2}}, \end{cases} \qquad i = 1, 3. \tag{2.29}$$

Next, we describe the implementation of the traction-at-split-node method in the staggered grid, following [Dalguer and Day, 2007]. We show the position of the fault plane and split-nodes in the FD grid in Figure 2.1b. We need to modify the FD formulas for components directly at the fault to take into account the division of the space by the fault boundary. The exception is the discontinuous $\sigma_{13}^{\pm}$ as its calculation requires only along-fault differences.

For the fault nodes with position given by indexes I, J_F (position of the fault in the y direction), K, the shear velocity components $(v_1^{\pm})_{I,J_F,K}$ and $(v_3^{\pm})_{I\frac{1}{2},J_F,K\frac{1}{2}}$ are calculated from (2.22). For the purpose of the body force calculation (2.20), the fault acts as a free surface with traction components σ_{12} and σ_{23} considered zero at the fault boundary. We use mixed order FD formulas to calculate the elastodynamic forces at the fault $(f_1^{\pm})_{I,K}$ and $(f_3^{\pm})_{I\frac{1}{2},K\frac{1}{2}}$. Central formulas from Equations 2.6 and 2.8 can be used in the shear directions 1 and 3 but one-sided 2-nd order FD formula needs to be used in the fault normal direction 2:

$$(f_1^{\pm})_{I,K} = \Delta h^2\Big[(D_1^{(4)}\sigma_{11}^{\pm})_{I,J_F,K} + (D_3^{(4)}\sigma_{13}^{\pm})_{I,J_F,K} \pm (\sigma_{12})_{I,J_F^{\pm\frac{1}{2}},K}\Big] \tag{2.30}$$

$$(f_3^{\pm})_{I\frac{1}{2},K\frac{1}{2}} = \Delta h^2\Big[(D_1^{(4)}\sigma_{13}^{\pm})_{I\frac{1}{2},J_F,K\frac{1}{2}} + (D_3^{(4)}\sigma_{33}^{\pm})_{I\frac{1}{2},J_F,K\frac{1}{2}} \pm (\sigma_{23})_{I\frac{1}{2},J_F^{\pm\frac{1}{2}},K\frac{1}{2}}\Big], \tag{2.31}$$

where $D_i^{(k)}$ means finite difference operator of the k-th order in the direction of the i-th axis.

We acquire the final equations for the trial traction and slip rate by inserting these forces into (2.23) and (2.22), applying (2.10) and putting $M^+ = M^- = 1/2\Delta h^3\rho$, leading to:

$$\begin{aligned} (T_1^T)^{N\frac{1}{2}} &= T_1^0 - \frac{1}{2}\frac{\Delta h}{\Delta t}\rho v_1^N - (R_1^-)^{N\frac{1}{2}}, \\ (T_3^T)^{N\frac{1}{2}} &= T_3^0 - \frac{1}{2}\frac{\Delta h}{\Delta t}\rho v_3^N - (R_3^-)^{N\frac{1}{2}}, \\ (v_1^-)^{N1} &= (v_1^-)^N + \frac{2\Delta t}{\Delta h\rho}\left[(R_1^-)^{N\frac{1}{2}} + (T_1)^{N\frac{1}{2}} - T_1^0\right], \\ (v_3^-)^{N1} &= (v_3^-)^N + \frac{2\Delta t}{\Delta h\rho}\left[(R_3^-)^{N\frac{1}{2}} + (T_3)^{N\frac{1}{2}} - T_3^0\right], \end{aligned} \tag{2.32}$$

with

$$
\begin{aligned}
(R_1^-)^{N\frac{1}{2}} &= \frac{1}{4}\Big[(D_1^{(2)}\sigma_{11}^-) + (D_3^{(2)}\sigma_{13}^-)\Big] - (\sigma_{12})_{I,J_F^{-\frac{1}{2}},K},\\
(R_3^-)^{N\frac{1}{2}} &= \frac{1}{4}\Big[(D_1^{(2)}\sigma_{13}^-) + (D_3^{(2)}\sigma_{33}^-)\Big] - (\sigma_{23})_{I^{\frac{1}{2}},J_F^{-\frac{1}{2}},K^{\frac{1}{2}}}.
\end{aligned}
\tag{2.33}
$$

Note that the positions of the components are staggered in space with $'1'$ components at nodes (I, J_F, K), while the $'3'$ components are at $(I^{\frac{1}{2}}, J_F, K^{\frac{1}{2}})$.

Calculation of diagonal components of stress σ_{11} and σ_{33} (both discontinuous across the fault) and σ_{22} (continuous) require FD of v_2 along the 2-th axis across the fault. We calculate the value of v_2 directly at the fault and then can use one-sided differences. As σ_{22} and v_2 are continuous across the fault, we can equate the right sides of the elastodynamic equation (in the case of v_2) and Hooke's law (in the case of σ_{22}) on the $'+'$ and $'-'$ sides. For spatially constant λ and μ, we get:

$$
\begin{aligned}
&\frac{4(\lambda+2\mu)}{\Delta h}(v_2)_{I^{\frac{1}{2}},J_F,K} = \frac{2(\lambda+2\mu)}{\Delta h}\Big[(v_2)_{I^{\frac{1}{2}},J_F^{-\frac{1}{2}},K} + (v_2)_{I^{\frac{1}{2}},J_F^{\frac{1}{2}},K}\Big]\\
&+\frac{\lambda}{\Delta h}\Big[-(D_1^{(4)}v_1^-)_{I^{\frac{1}{2}},J_F,K} - (D_3^{(4)}v_3^-)_{I^{\frac{1}{2}},J_F,K} + (D_1^{(4)}v_1^+)_{I^{\frac{1}{2}},J_F,K} + (D_3^{(4)}v_3^+)_{I^{\frac{1}{2}},J_F,K}\Big].
\end{aligned}
\tag{2.34}
$$

We now can use the 2-nd order one-sided FD of v_2 on the halved spatial interval $\Delta h/2$ to get the rest of the stress components at the fault:

$$
\begin{aligned}
\frac{(\sigma_{11}^{\pm})^{N\frac{1}{2}}_{I^{\frac{1}{2}},J_F,K} - (\sigma_{11}^{\pm})^{N^{-\frac{1}{2}}}_{I^{\frac{1}{2}},J_F,K}}{\Delta t} &= (\lambda+2\mu)(D_1^{(4)}v_1^{\pm})^N_{I^{\frac{1}{2}},J_F,K}\\
&+ \lambda(D_3^{(4)}v_3^{\pm})^N_{I^{\frac{1}{2}},J_F,K} \pm \lambda\frac{(v_2)^N_{I^{\frac{1}{2}},J_F,K} - (v_2)^N_{I^{\frac{1}{2}},J_F^{\pm\frac{1}{2}},K}}{\Delta h/2},
\end{aligned}
\tag{2.35}
$$

$$
\begin{aligned}
\frac{(\sigma_{22})^{N\frac{1}{2}}_{I^{\frac{1}{2}},J_F,K} - (\sigma_{22})^{N^{-\frac{1}{2}}}_{I^{\frac{1}{2}},J_F,K}}{\Delta t} &= \lambda(D_1^{(4)}v_1^{\pm})^N_{I^{\frac{1}{2}},J_F,K}\\
&+ \lambda(D_3^{(4)}v_3^{\pm})^N_{I^{\frac{1}{2}},J_F,K} \pm (\lambda+2\mu)\frac{(v_2)^N_{I^{\frac{1}{2}},J_F,K} - (v_2)^N_{I^{\frac{1}{2}},J_F^{\pm\frac{1}{2}},K}}{\Delta h/2},
\end{aligned}
\tag{2.36}
$$

$$
\begin{aligned}
\frac{(\sigma_{33}^{\pm})^{N\frac{1}{2}}_{I^{\frac{1}{2}},J_F,K} - (\sigma_{33}^{\pm})^{N^{-\frac{1}{2}}}_{I^{\frac{1}{2}},J_F,K}}{\Delta t} &= \lambda(D_1^{(4)}v_1^{\pm})^N_{I^{\frac{1}{2}},J_F,K}\\
&+ (\lambda+2\mu)(D_3^{(4)}v_3^{\pm})^N_{I^{\frac{1}{2}},J_F,K} \pm \lambda\frac{(v_2)^N_{I^{\frac{1}{2}},J_F,K} - (v_2)^N_{I^{\frac{1}{2}},J_F^{\pm\frac{1}{2}},K}}{\Delta h/2}.
\end{aligned}
\tag{2.37}
$$

Second order one-sided FD formulas can cause unwanted high frequency oscillations. To suppress them, we add an artificial viscous damping term to the volumetric forces $f_i^{\pm}$:

$$
\acute{f}_i^{\pm} = f_i^{\pm} + \eta\dot{f}_i^{\pm} \tag{2.38}
$$

used to calculate shear velocity components at the fault. The damping coefficient η depends on the time dicretization $\eta = \eta_s \Delta t$. Dependence on Δt ties damping to the spatial discretization via the CFL criterion and damps amplitudes at frequencies close to the grid's Nyquist limit. Ideal value of $\eta_s = 0.3$ was determined experimentally by Dalguer and Day [2007] to optimize the impact on the rupture velocity.

2.2.4 Friction law

FD3D_TSN features two friction laws: (1) classical slip-weakening law [Ida, 1972, Andrews, 1976] and (2) rate-and-state law with rapid velocity weakening at high slip rates [Ampuero and Ben-Zion, 2008, Beeler et al., 2008], as proposed by Dunham et al. [2011]. Although the numerical implementation of the former is straightforward, the latter needs a specific approach as it is complicated by the need to solve an additional set of two ordinary differential equations at every node along the fault.

Linear slip-weakening friction

The linear slip-weakening friction law [Ida, 1972] is widely used in dynamic rupture simulations. The value of the effective friction coefficient depends only on the slip s:

$$S = \sigma_n f(s). \tag{2.39}$$

We consider the linear slip-weakening relationship in the form introduced by Andrews [1976]:

$$f(s) = \begin{cases} f_s - (f_s - f_d)s/D_c, & \text{if } s < D_c \\ f_d, & \text{if } s \geq D_c, \end{cases} \tag{2.40}$$

where f_s, f_d and D_c are initial model parameters. During the sliding frictional coefficient linearly decreases from the static value f_s to the dynamic value $f_d < f_s$ over a characteristic slip-weakening distance D_c as shown in Figure 2.3.

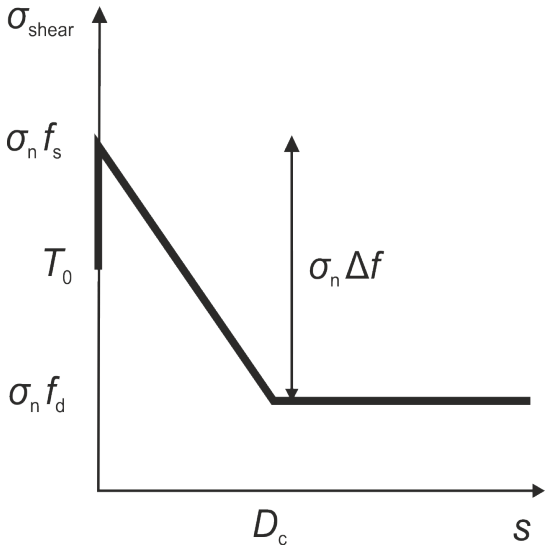

Figure 2.3: Illustrative plot of SW friction, thick black line shows the development of friction with slip.

The calculation of the frictional force during the dynamic rupture simulation requires tracking the value of slip at every time step by integrating the slip rate $\dot{s}$:

$$s^{N\frac{1}{2}} = s^{N^{-\frac{1}{2}}} + \Delta t \dot{s}^N. \tag{2.41}$$

The staggered grid complicates the enforcement of the fault boundary condition slightly because the horizontal and vertical components of the slip rate are calculated at different nodes. To correct this, we use bilinear interpolation of the missing components when evaluating the absolute values of slip rate and traction in the friction law. The frictional strength needed in Equation 2.29 can then be directly calculated as

$$S^{N\frac{1}{2}} = \begin{cases} \sigma_n[f_s - (f_s - f_d)s^{N\frac{1}{2}}/D_c], & \text{if } s^{N\frac{1}{2}} < D_c \\ \sigma_n f_d, & \text{if } s^{N\frac{1}{2}} \geq D_c. \end{cases} \tag{2.42}$$

Rate-and-state friction with fast-velocity-weakening

Rate-and-state friction depends on sliding velocity $\dot{s}$ and state variable ψ:

$$S = \sigma_n f(\dot{s}, \psi). \tag{2.43}$$

State variable, that describes the state of the contacts at the surface boundary, behaves according ti the evolution law, which takes the form of an ordinary differential equation:

$$\frac{d\psi}{dt} = F(s, \dot{s}, \psi). \tag{2.44}$$

Dynamic models employing the rate-and-state laws usually require the fault to continue sliding at all times. Traction is thus set to be always equal to the frictional strength, meaning that only the second case in (2.17) applies and we need to prescribe the initial non-zero slip rate $\dot{s}_{ini}$.

In FD3D_TSN, we implement the formulation of fast-velocity-weakening rate-and-state friction used in SCEC/USGS benchmark suite [Harris et al., 2018] that consists of five interlinked equations:

$$\begin{aligned} S &= \sigma_n a \ \text{arcsinh}\Big[\frac{\dot{s}}{2\dot{s}_0}\exp\Big(\frac{\psi}{a}\Big)\Big], \\ \frac{d\psi}{dt} &= -\frac{\dot{s}}{L}[\psi - \psi_{SS}], \\ \psi_{SS} &= a \log\Big[\frac{2\dot{s}_0}{\dot{s}}\ \sinh\Big(\frac{f_{SS}}{a}\Big)\Big], \\ f_{SS} &= f_w + \frac{f_{LV} - f_w}{\Big[1 + (\dot{s}/\dot{s}_w)^8\Big]^{1/8}}, \\ f_{LV} &= f_0 - (b - a)\log\Big(\frac{\dot{s}}{\dot{s}_0}\Big). \end{aligned} \tag{2.45}$$

Frictional parameters in 2.45 consist of direct effect parameter a, state evolution parameter b, reference friction f_0 at slip rate $\dot{s}_0$, characteristic slip distance L, weakening velocity s_w, and weakened friction f_w, see Chapter 3 for details. Dynamic rupture simulations using rate-and-state friction are complicated by the

need to solve two coupled differential equations at every node at the fault boundary, one for the shear velocity components (slip rate) and the other for the state variable.

Following Rojas et al. [2009], we consider the state variable and slip rate staggered in time and extend their method to 3D. The time-staggered distribution of slip rate and state variable (see Figure 2.4) is a natural choice for our staggered FD method and it leads to more easily solvable differential equations while having practically the same accuracy as higher order methods Rojas et al. [2009]. Basis of the method is the analytical integration of the evolution equation for the state variable over one time-step, while considering the slip rate constant and equal to its value in the middle of the discrete-time interval. A similar approach to the differential equation for the slip rate leads to a nonlinear equation requiring the application of a nonlinear solver.

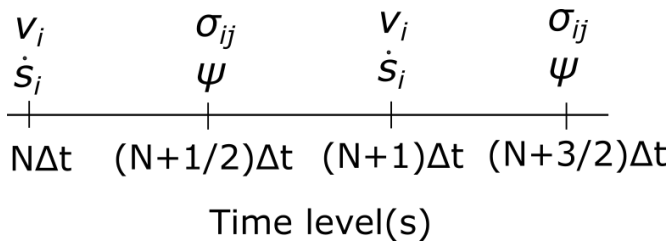

Figure 2.4: The time staggered position of slip rate and state variable.

Time-staggered distribution of slip rate and state variable means that slip rate is calculated in the middle of the time interval between two successive time steps $(N-1/2)\Delta t$ and $(N+1/2)\Delta t$. We assume that the time-step interval is small enough that the slip rate does not change significantly over the duration of the time step and can be thus approximated by that one value over the whole interval: $\dot{s}(t) = (\dot{s})^N, \forall t \in \big((N-1/2)\Delta t, (N+1/2)\Delta t\big)$. We can then integrate the evolution law for ψ (last four equations in Equation 2.45) over the same time interval:

$$
\begin{aligned}
\psi^{N^{\frac{1}{2}}} &= (\psi^{N^{-\frac{1}{2}}} - \psi_{SS}(\dot{s}^N)) \exp(-\frac{\dot{s}^N \Delta t}{L}) + \psi_{SS}(\dot{s}^N), \\
\psi_{SS}(\dot{s}^N) &= a \log\Big[\frac{2s_0}{\dot{s}^N} \sinh\Big(\frac{f_{SS}(\dot{s}^N)}{a}\Big)\Big], \\
f_{SS}(\dot{s}^N) &= f_w + \frac{f_{LV}(\dot{s}^N) - f_w}{\Big[1 + (\dot{s}^N/s_w)^8\Big]^{1/8}}, \\
f_{LV}(\dot{s}^N) &= f_0 - (b-a) \log\Big(\frac{\dot{s}^N}{s_0}\Big).
\end{aligned}
\tag{2.46}
$$

The second step is the calculation of slip rate $(\vec{\dot{s}})^{N^1}$ from (2.33), which is complicated by the spatially staggered position of the slip rate components along the fault (see Figure 2.1a). We first update the total value of slip rate $\dot{s}^{N^1}$ in both nodes where slip rate components $\dot{s}_1$ and $\dot{s}_3$ are positioned. The equation for $\dot{s}^{N^1}$ makes use of collinearity of traction and slip rate (2.26), leading to

$$
(\dot{s})^{N^1} = -\frac{4\Delta t}{\Delta h \rho}(T)^{N^{\frac{1}{2}}} + \left| (\vec{\dot{s}})^N - \frac{4\Delta t}{\Delta h \rho}\left[(\vec{R}^-)^{N^{\frac{1}{2}}} - \vec{T}_1^0\right]\right|. \tag{2.47}
$$

We need to perform a bilinear interpolation of missing components of $(R_i^-)^{N^{\frac{1}{2}}}$ in both staggered nodes.

Since the fault is assumed to be always sliding, the absolute value of shear traction $(T)^{N^{\frac{1}{2}}}$ is equal to friction S from the first equation of (2.45):

$$(\dot{s})^{N^1} = -\frac{4\Delta t}{\Delta h \rho} S(\dot{s}^?, \psi^{N^{\frac{1}{2}}}) + \left| (\vec{\dot{s}})^N - \frac{4\Delta t}{\Delta h \rho} \left[(\vec{R}^-)^{N^{\frac{1}{2}}} - \vec{T}_1^0 \right] \right|. \tag{2.48}$$

We need to choose an appropriate method to discretize the nonlinear equation for $\dot{s}$ in time, which boils down to the choice of $\dot{s}^?$. Forward Euler method is the easiest choice, setting $\dot{s}^? = (\dot{s})^N$, but the resulting scheme is highly unstable, especially for small values of the slip rate, where $\text{arcsinh}(x)$ changes quickly. A backward Euler scheme ($\dot{s}^? = \dot{s}^{N^1}$) or trapezoidal scheme ($\dot{s}^? = (\dot{s}^N + \dot{s}^{N^1})/2$) needs to be used instead. We found only negligible accuracy improvement when using the higher order trapezoidal scheme and thus use the simpler Backward Euler scheme in FD3D_TSN, setting $\dot{s}^? = \dot{s}^{N^1}$:

$$(\dot{s})^{N^1} = (\dot{s}_C)^N + C \ \text{arcsinh}\Big[\frac{(\dot{s})^{N^1}}{2s_0} \exp\Big(\frac{\psi^{N^{\frac{1}{2}}}}{a}\Big)\Big], \tag{2.49}$$

where

$$(\dot{s}_C)^N = \left| (\vec{\dot{s}})^N - \frac{4\Delta t}{\Delta h \rho} \left[(\vec{R}^-)^{N^{\frac{1}{2}}} - \vec{T}_1^0 \right] \right| \tag{2.50}$$

denotes the part of the Equation 2.47 already explicitly calculated before the time step $(n+1)\Delta t$, and

$$C = \frac{4\Delta t}{\Delta h \rho} \sigma_n a. \tag{2.51}$$

We use Newton's method to solve the nonlinear Equation 2.49. Finding a new slip rate value $(\dot{s})^{N^1}$ that satisfies Equation 2.49 is equivalent to finding a root of the function

$$F\left((\dot{s})^{N^1}\right) = (\dot{s}_C)^N - (\dot{s})^{N^1} + C \ \text{arcsinh}\Big[\frac{(\dot{s})^{N^1}}{2s_0} \exp\Big(\frac{\psi^{N^{\frac{1}{2}}}}{a}\Big)\Big]. \tag{2.52}$$

We modify the Equation 2.52 to simplify the founding of the analytical derivative of the function F by substituting

$$w = \ \text{arcsinh}\Big[\frac{(\dot{s})^{N^1}}{2s_0} \exp\Big(\frac{\psi^{N^{\frac{1}{2}}}}{a}\Big)\Big], \tag{2.53}$$

to get a new function

$$F(w) = (\dot{s}_C)^N + Cw - \exp\Big(\frac{-\psi^{N^{\frac{1}{2}}}}{a}\Big) 2s_0 \text{sinh}(w) \tag{2.54}$$

with simpler derivative

$$F'(w) = C - \exp\Big(\frac{-\psi^{N^{\frac{1}{2}}}}{a}\Big) 2s_0 \text{cosh}(w). \tag{2.55}$$

We start the iterative process from the value of w in the previous time step:

$$w_0 = \operatorname{arcsinh}\Big[\frac{(\dot{s})^N}{2s_0}\exp\Big(\frac{\psi^{N\frac{1}{2}}}{a}\Big)\Big]. \tag{2.56}$$

We find the root w of the function $F(w)$ approximately by iteration of

$$w_{n+1} = w_n - \frac{F(w_n)}{F'(w_n)}, \tag{2.57}$$

where w_n is the approximate value of the root at the n-th iteration. This is done until the difference between successive values of w (the error of the approximation) is lower than 10^{-5} and 10^{-10} for single and double precision computations, respectively. We get the value of slip rate from the substitution (2.53):

$$(\dot{s})^{N1} = 2s_0 \sinh(w)\exp\Big(-\frac{\psi^{N\frac{1}{2}}}{a}\Big). \tag{2.58}$$

Components of the updated slip rate are found from collinearity of the slip rate and the traction (2.18):

$$(\vec{\dot{s}})^{N1} = (\dot{s})^{N1}\frac{(\vec{T})^{N\frac{1}{2}}}{(T)^{N\frac{1}{2}}}. \tag{2.59}$$

The discrete solution of the fault boundary conditions with the fast-velocity-weakening rate-and-state law using the traction-at-split-node method consists of updatng the value of the state variable from Equations 2.46 and Newton's method solution of Equation 2.49 to update the slip rate. This is done at every node at the fault surface independently at every time-step. As the Newton's method converges rather quickly, the additional computational cost for solving the nonlinear equation at every node on the fault surface is negligible, being just a few percent of the computational time for the cases presented in the Section 2.5 Verification Exercise and Performance.

2.3 GPU acceleration

GPU acceleration of the FD3D_TSN code employs the OpenACC programming model (for details, see `https://www.openacc.org`). OpenACC is a standardized directive-based system for parallel processing on heterogeneous platforms that consist of a host (CPU) and compute accelerators, in particular, GPUs. OpenACC directives make it possible to parallelize the code and offload computationally intensive parts to the accelerators, whereas the possibility to compile the same code for a serial run is retained, similarly to the OpenMP programming model (for details, see `www.openmp.org`). OpenACC has been implemented in a few C, C++, Fortran compilers. For x86-64 hardware architecture and Linux and Windows systems, Nvidia Corporation offers no-cost community edition of compilers and tools, besides commercial professional edition, and also the free GNU compiler collection (GCC) is reaching with OpenACC mature state. Nvidia not only targets Nvidia accelerators solely but also allows running OpenACC-parallelized programs on multicore CPUs. GCC can offload to Nvidia GPUs already and plans to target AMD GPUs (`https://gcc.gnu.org/wiki/OpenACC`).

The FD3D_TSN code optimizes data locality to minimize relatively slow data transfers between the host and GPU memory through the PCIe interface. Specifically, input data are moved into the GPU memory by one single transfer using the OpenACC directive !$ACC DATA COPYIN; substantially, smaller output data are copied back to the host memory every timestep using the directive !$ACC DATA COPY, and no more data between the host and GPU are transferred in the course of computation. Parallelizable regions of nested loops are surrounded by the directives !$ACC PARALLEL and !$ACC LOOP COLLAPSE (3). Being more specific, for example, specifying more clauses of the LOOP directive or proposing nondefault values of gang and worker sizes and vector length (i.e., CUDA grid and block sizes for controlling the distribution of threads among GPU multiprocessors) did not improve the performance. On the other hand, the clause COLLAPSE (3) is essential for performance, as it allows accumulating a large number of iterations into one collapsed loop, which is a desirable feature for the GPU acceleration.

2.4 Using the code

The Fortran source code with documentation, several examples, and basic MATLAB plotting tools are freely available in a public repository on GitHub (`https://github.com/JanPremus/fd3d_TSN`). The examples on GitHub comprise four SCEC/USGS benchmark exercises, specifically TPV5, TPV8, TPV9, and TPV104, offering the possibility of verification of the code. In addition, a dynamic rupture model of the 2016 Amatrice earthquake [Gallovič et al., 2019b] is shown, to demonstrate the use of a general input file forwardmodel.dat containing spatially varying dynamic parameters.

2.4.1 Compilation and input files

Slip-weakening and fast-velocity-weakening friction use different sets of dynamic parameters. Moreover, the slip rates are calculated by two different algorithmic implementations. The user can thus select between the friction laws by preprocessor flag -DFVW, switching from the default slip-weakening to the fast-velocity-weakening friction.

There are two ways to generate input parameters for a dynamic model in FD3D_TSN—using a hardcoded function or input dynamic parameters through the file forwardmodel.dat. Hardcoded function needs to be specified during compilation, using preprocessor flags. SCEC/USGS benchmarks require a combination of two flags: -DSCEC and a chosen problem (-DTPV5, -DTPV8, -DTPV9, or -DTPV104). When none of these flags are present, forwardmodel.dat file is used as the input instead. This file contains a spatial distribution of dynamic parameters in the form of one line of values of prestress, static friction coefficient, and characteristic slip-weakening distance on an equidistant grid at the fault, starting in the left corner. The grid can be coarser than the FD grid; the values are bilinearly interpolated to the FD grid [Gallovič et al., 2019a,b]. The size of the coarser grid (amount of points in the horizontal and vertical directions) only needs to be set in the file inputinv.dat.

FD3D_TSN works with any horizontally layered 1D velocity model; its parameters are saved in the file crustal.dat. File inputfd3d.dat contains the information necessary for the initialization of the FD discretization and the PMLs, namely the size of the grid, discretization intervals in space and time, and PML thickness and damping. Because the source geometry is simple (2D planar and vertical), hard-coding another model, including its potential parameterization, is straightforward. This way, the code can be easily adapted for various user's needs such as a specific parametric study or a particular dynamic inversion. Code FD3D_TSN_PT represents an example of the latter following the inversion strategy of Gallovič et al. [2019a,b], which uses FD3D_TSN as the forward solver.

2.4.2 Output files

On-fault slip rate and shear stress time series are stored in files sliprateX.res, sliprateZ.res, shearstressX.res, shearstressZ.dat, that is, for the horizontal (X) and vertical (Z) components separately. When the fast-velocity-weakening friction is enabled, the time series of the state variable is stored in file psi.res. Given the amount of data stored, these files are in binary format. Two MATLAB files are provided to demonstrate the retrieval of data from the binary files. User can acquire and plot time series of components of slip rate and shear stress at a given position (PrintSeries.m), or their spatial distribution at a given time (PrintSnapshot.m).

Spatial distributions of slip, rupture time, rise time, rupture velocity, and stress drop are generated and stored in separate text files. Besides, a local estimate of the cohesive zone (the area behind the rupture front in which shear stress decreases from its static to its dynamic value [Day et al., 2005, Wollherr et al., 2018] is provided in the file czone.dat for inspection of the numerical accuracy.

Synthetic seismograms are generated at chosen nodes in the form of time series of separate velocity components stored in files stan%i.dat, in which %i numbers the node. The user needs to set the number of nodes and their position on the grid in the file inputfd3d.dat before simulation. A more detailed and upto-date description of the input and output files can be found in the online documentation at the GitHub repository.

2.5 Verification exercise and performance

We have performed several exercises from the community benchmark suite of the SCEC/USGS Spontaneous Rupture Code Verification Project [Harris et al., 2018]. Their main webpage (`http://scecdata.usc.edu/cvws/`) contains descriptions of the exercises and results generated by 5—20 different solvers, depending on the exercise. There are three types of results for comparison: time evolution of physical quantities at prescribed points on the fault (slip, slip rate, shear stress, and state variable if applicable), seismograms at off-fault positions, and rupture time contour plots, that is, lines showing the rupture tip position at every half second. Here, we present our results for benchmarks TPV5 (slip-weakening friction) and TPV104 (fast-velocity-weakening friction). In addition, the results for the TPV8 and TPV9 benchmarks can be found on the SCEC/USGS webpage.

For the TPV5 benchmark, the size of the computational domain is 31 × 10 × 15:5 km, whereas, for the TPV104 benchmark, it is larger (40 × 10 × 20 km) because the model contains additional velocity-strengthening layers around the fault following the benchmark definition. Figures 2.5 and 2.6 display results for TPV5 (spatial grid step $\Delta h = 100$ m) and TVP104 (spatial grid step $\Delta h = 50$ m), respectively. They are presented in terms of the rupture time contours along the fault and the on-fault slip rate and shear–stress time series at two locations. To better illustrate the TPV5 simulation, Figure 2.7 shows snapshots of both slip rate and wavefield around the fault at equidistant times.

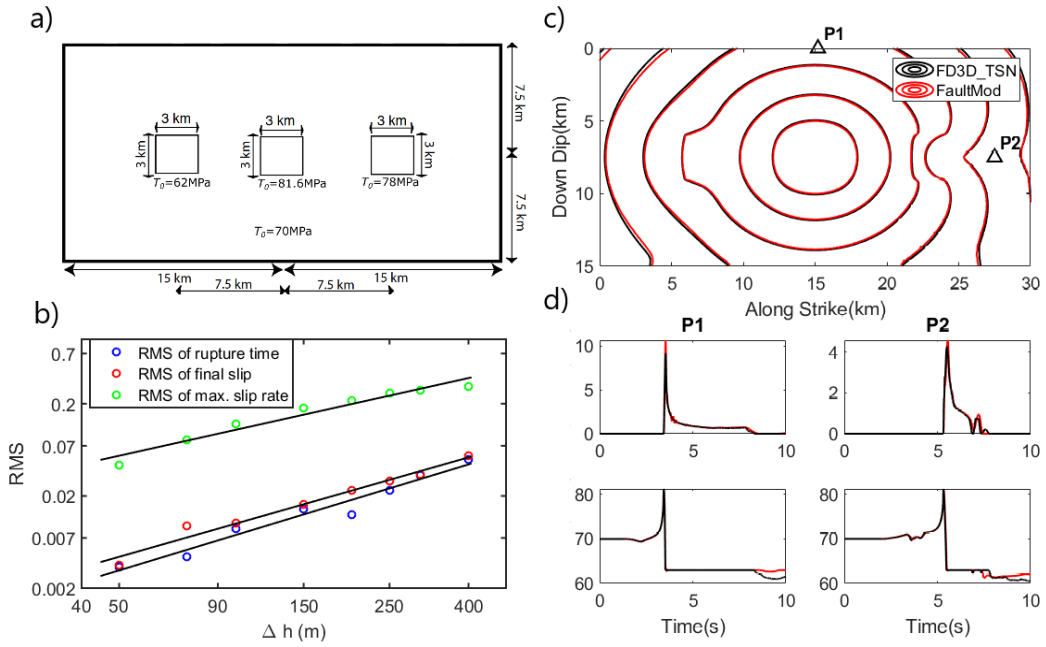

Figure 2.5: Results for the TPV5 benchmark (heterogenous prestress). (a) Schematic showing dimensions of the fault and positions of prestress heterogeneities T 0 (adopted from the Southern California Earthquake Center and U.S. Geological Survey [SCEC/USGS] benchmark webpage). (b) A plot of the root mean square (RMS) difference of the rupture time, slip, and maximum slip rate relative to a solution with $\Delta h = 25$ m as a function of Δh for FD3D_TSN. (c) Rupture front contours on the fault plane every 1 s. (d) Slip rates and shear stress (equal to the horizontal component of traction) at points P1 and P2, corresponding to fault receivers 'st000dp000' and 'st120dp075' in Harris et al. [2018]. For their position, see panel (a). Simulation results for FD3D_TSN with $\Delta h = 100$ m and SeisSol [Pelties et al., 2012] are denoted by black and red lines, respectively.

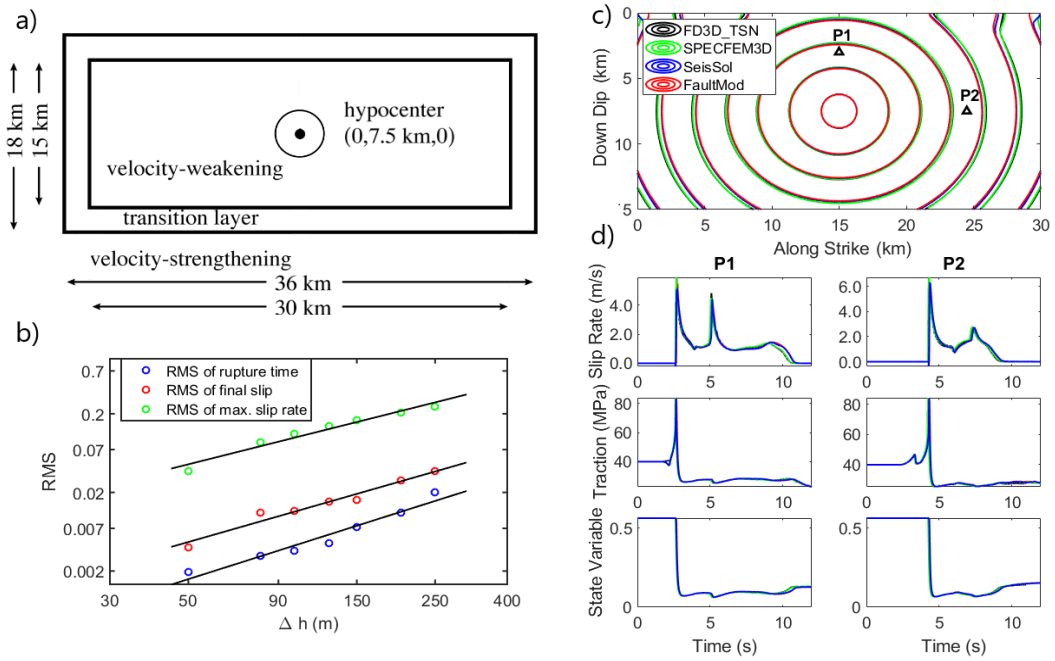

Figure 2.6: Same as Figure 2.5 but for the rate-and-state friction TPV104 benchmark. (a) Schematic diagram of the dimensions of the fault and positions of the velocity-weakening and strengthening zones (rectangles) and the nucleation zone (circle), as adopted from the SCEC/USGS webpage. (b) A plot of the root mean square (RMS) difference of the rupture time, slip, and maximum slip rate relative to a solution with $\Delta h = 25$ m as a function of Δh for FD3D_TSN. (c) Rupture front contours on the fault plane every 1 s. (d) The time evolution of the state variable. Solutions of FD3D_TSN with $\Delta h = 50$ m (black line), SPECFEM3d (green line), SeisSol (red line), and FaultMod (blue line) are shown. Nodes P1 and P2 correspond to fault receivers 'faultst000dp030' and 'faultst090dp075', respectively.

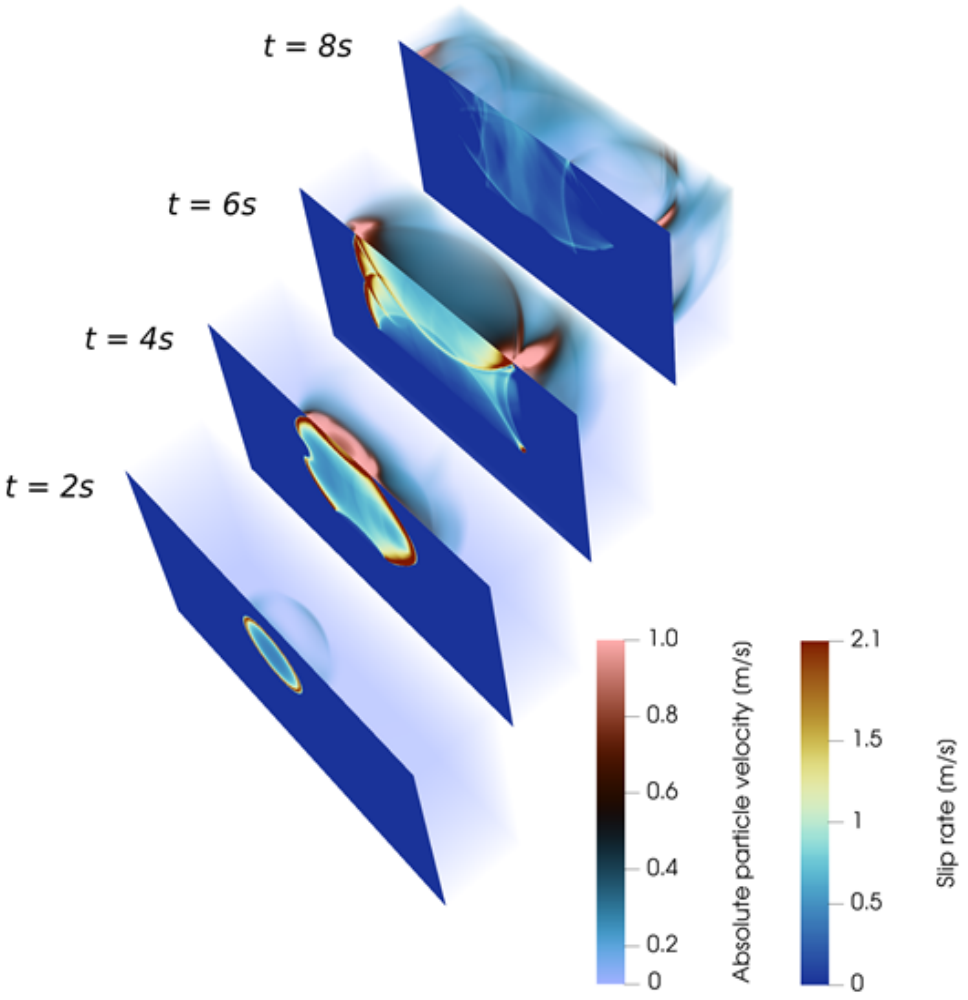

Figure 2.7: 3D plot animating the slip rate along the fault and the radiated wavefield for the TPV5 benchmark with heterogeneous initial stress at equidistant times, after the rupture nucleation in the middle of the fault. See also Figure 2.5 for more information on the problem setup.

In both TPV5 and TVP104, the difference between the results of FD3D_TSN and code SeisSol [Heinecke et al., 2014, Pelties et al., 2014, Uphoff et al., 2017] are well within the typical variation among other solvers [Harris et al., 2009, 2011, 2018, Barall and Harris, 2015]. We note that the full set of the FD3D_TSN simulation results are uploaded in the benchmark database of solutions. At the benchmark website, our solutions can be compared with other code outputs and physical quantities on and off the fault.

We note small differences in rupture times for different solvers in the fast-velocity-weakening friction benchmark TPV104. The solution of FD3D_TSN agrees very well with that of SPECFEM3D [Kaneko et al., 2008], whereas the solutions of FaultMod [Barall, 2006] and SeisSol show slightly slower rupture (Figure 2.5). These differences remain visible with mesh refinement (compare to the $\Delta h = 50$ m solution). We understand these differences as an expression

Discrete Step (m)	**Degrees of Freedom × Timesteps (RAM Requirement)**	**Single-Core Wall Clock Time (s)**	**GPU-Accelerated Wall Clock Time (s)**
100	54,558,900 × 3000 (210 MB)	0:3:12	0:0:22
50	389,491,200 × 6000 (1490 MB)	0:39:13	0:3:47

Table 2.1: Wall clock times of the FD3D_TSN code for the TPV5 benchmark model, shown for two finite-difference (FD) spatial discretizations and for single core (Intel i9-9900K) and GPU-accelerated versions (Nvidia RTX 2700)

Discrete step (m)	**Degrees of freedom × Timesteps (RAM requirement)**	**Single-core wall clock time (s)**	**GPU-accelerated wall clock time (s)**
100	88,149,600 × 3000 (340 MB)	0:4:28	0:0:22
50	638,517,600 × 6000 (2440 MB)	0:57:46	0:4:56

Table 2.2: Same as Table 2.1 but for the TPV104 Benchmark

of differences in the implementation of rate-and-state friction evolution, but not restricted to staggered grid-specific choices.

Following Day et al. [2005], we calculate the root mean square (RMS) difference of the spatially averaged slip, rupture time, and peak slip rate for various grid sizes Δh relative to a high-resolution reference solution with $\Delta h = 25$ m, see b panels in Figures 2.5 and 2.6. Spatial discretizations $\Delta h = 100$ m and $\Delta h = 50$ m for benchmarks TPV5 and TPV104, respectively, are chosen for providing results sufficiently close to the reference solution (both rupture time and slip RMS measures are less than 1%). The slopes of the RMS misfits from both benchmarks are $-1/1$, $-1/2$, and $-1/3$ for maximum slip rate, slip, and rupture time, respectively.

Wall clock times of the code for both grid spacings Δh and problems are shown in Tables 2.1 and 2.2, respectively, both for the serial (running on one CPU core) and GPU-accelerated versions. We used CPU Intel i9-9900K and GPU Nvidia RTX 2070 hardware to run these tests. When using the GPU, it is essential to keep all variables in the GPU memory, because any data transfer to and from GPU memory is the major bottleneck affecting the overall speed of simulation. The amount of GPU memory is generally smaller (several GB) than the computer RAM, which limits the maximum size of the model. Memory requirements of these simulations were comfortably below this limit of 8 GB for Nvidia RTX 2070, see Tables 2.1 and 2.2 for details.

2.6 Discussion and conclusions

This article presents FD3D_TSN, a simple-to-use FD code for dynamic earthquake source modeling assuming slip-weakening and fast-velocity-weakening rate-and-

state friction laws. The code is written in the Fortran programming language and is freely available under the GNU General Public License license. The optional GPU acceleration using OpenACC compiler directives (currently provided in NV Fortran and GNU Fortran) can shorten the wall clock time by a factor of 10 compared to the same version of the code running on a single CPU core (for the hardware configuration with CPU Intel i9-9900K and GPU Nvidia RTX 2070).

FD3D_TSN is original in its high precision and fast speed. The latter is achieved by simplifying the geometry of the problem. At present, FD3D_TSN is limited to a vertical planar fault geometry, orthogonal to the planar free surface, embedded in an elastic medium with homogeneous or depth-dependent velocities and density. The planar fault orthogonal to the free surface is optimal for the regular grid discretization. Moreover, the consequent antisymmetry of the velocity and stress permits the calculations on one side of the fault only.

We admit that the model simplifications may restrict the range of possible applications of the code. However, in some cases, the simplified model can be considered as an approximation of the true model. For example, if the rupture does not reach the Earth's surface, a dipping fault geometry can be approximated by stretching the velocity model vertically to respect the original along-dip position of the fault intersections with the velocity model layers [Gallovič et al., 2019b]. In other cases, it may be straightforward to extend the code to incorporate specific features. For example, the effect of a low-velocity fault zone could be modeled by introducing velocity reduction around the fault, when obeying the model symmetry across the fault. Nevertheless, there are many more possible further developments such as the implementation of dipping free-surface topography (e.g., Robertsson [1996]) to correctly model the interaction between the free surface and the rupture propagating along a dipping fault.

Despite the simplification, FD3D_TSN has already proven useful in several applications. It is implemented as a new forward solver in Bayesian dynamic source inversion code FD3D_TSN_PT, see Gallovič et al. [2019a,b]. Gallovič and Valentová [2020] utilized FD3D_TSN to simulate a large number of rupture scenarios complying with ground-motion prediction equations for stress-drop analysis. We foresee its usability also in parametric studies and in teaching the fundamentals of rupture dynamics to students, as it can be used without access to supercomputing facilities. Generally speaking, we believe that having such an efficient code and making it available to the community will boost research toward data-driven dynamic earthquake source studies and physics-based scenario modeling.

2.7 Quasidynamic modeling of postseismic slip

Full dynamic simulations described in the preceeding sections are computationally very demanding. Our GPU accelerated code FD3D_TSN is capable of modeling 1 s of earthquake simulation in 1–2 s of GPU time. Long term modeling using this method would be thus unfeasible, as, e.g., one month of afterslip simulation would take $\sim$ 1000 hours.

Radiation and propagation of seismic waves in the vicinity of the fault occurs only in a limited time during and right after the seismic slip. Fault then continues to slip aseismically, without producing any significant seismic waves. Inertial term on the left-hand side of the elastodynamic equation 1.1 is therefore close to zero

during the aseismic period of calculations.

Omission of the inertial term greatly reduces the complexity of the problem as Green's tensor solution will consist only of the static response of the material. We apply the boundary integral element method, discretize the fault into patches and assume only horizontal slip s^i and traction T^i, where upper index i denotes the patch number [Gallovič, 2008]. The linear relationship between slip and displacement leads also to a linear relationship between slip and stress written as:

$$T^i(t) = T_0^i + K_{ij}s^j(t) - \frac{\mu}{2\beta}\dot{s}^i \tag{2.60}$$

where $T^i(t)$ and T_0^i are current and initial values of traction, s^j is slip in the patch j, and kernel tensor K_{ij} consists of the material responseat i-th patch to the unit slip in patch j [Perfettini et al., 2003]. The last term on the right side represents the approximate decrease of energy due to seismic radiation, which we use to stabilize the method [Rice, 1993]. Kernel for 3-D vertical strike-slip fault in halfspace can be found in Gallovič [2008]. Additionally, the traction needs to be equal to the value of friction at the fault:

$$T^i(\dot{s}^i, \psi^i) = \sigma_n^i f^i(\dot{s}^i, \psi^i), \tag{2.61}$$

where $\dot{s}^i$, ψ^i, and σ_n^i are values of horizontal slip rate, state variable, and normal stress at fault patch i. We calculate the friction coefficient from the fast-velocity-weakening rate-and-state friction law:

$$\begin{aligned}
f^i &= \sigma_n^i a^i \operatorname{arcsinh}\Big[\frac{\dot{s}^i}{2\dot{s}_0}\exp\Big(\frac{\psi^i}{a^i}\Big)\Big],\\
\frac{d\psi^i}{dt} &= -\frac{\dot{s}^i}{L^i}[\psi^i - \psi_{SS}^i],\\
\psi_{SS}^i &= a^i \log\Big[\frac{2\dot{s}_0}{\dot{s}^i}\,\sinh\Big(\frac{f_{SS}^i}{a^i}\Big)\Big],\\
f_{SS}^i &= f_w^i + \frac{f_{LV}^i - f_w^i}{\Big[1 + (\dot{s}^i/\dot{s}_w^i)^8\Big]^{1/8}},\\
f_{LV}^i &= f_0^i - (b^i - a^i)\log\Big(\frac{\dot{s}^i}{\dot{s}_0}\Big),
\end{aligned} \tag{2.62}$$

where variables with upper index i denote the value at patch i.

By equating 2.60 and 2.61, differentiating with respect to time, we can express the time drivative of the slip rate as:

$$\frac{d\dot{s}^i}{dt} = \frac{\sum K^{ij}\dot{s}^j - \sigma_n^i\dot{\psi}(\partial f^i/\partial\psi)}{\sigma_n^i(\partial f^i/\partial\dot{s}^i) + \mu/(2\beta)}. \tag{2.63}$$

Coupled with the evolution equation for state variable:

$$\frac{d\psi^i}{dt} = -\frac{\dot{s}^i}{L^i}[\psi^i - \psi_{SS}^i], \tag{2.64}$$

we get a series of ordinary differential equations. This is a major simplification in comparison with the fully dynamic model formulated as a set of partial differential equations.

We solve the ODE set by the 5th-order Runge-Kutta method with adaptive time step. For our afterslip modeling case of an application with only small slip rate (such as the afterslip modeling in this Thesis), the step prolongs up to a day, which further reduces the computational demands. Additionally, the sum in Equation 2.63 can be written as a spatial convolution, and quickly evaluated by means of the 2D Fast Fourier Transform [Gallovič, 2008]. By our experience, one month of postseismic modeling takes approximately 1–2 s of calculation time on a CPU, which is significantly less than the time required to simulate the seismic phase, even using the GPU acceleration.

The boundary integral method is implemented in inversion code fd3d_tsn_pt. The dynamic simulation switches into the quasidynamic one after a set amount of time, or when slip rate drops below 1cm/s everywhere at the fault. A certain level of numeric error is introduced into the numerical simulation by the transition from dynamic to quasidynamic modeling. Error is proportional to the amplitude of seismic waves in the vicinity of the fault that are discarded in the boundary integral method.

In the case of the 2014 Napa earthquake models, we set a maximum lenght of the dynamic simulation to 10 s. As the duration of the earthquake is approximately 8 s, the seismic waves should be minimal after the 10 s time period. We assess the level of numerical error introduced into the simulation by prolonging the dynamic simulation for the chosen 2014 Napa earthquake model from 10 s to 25 s. Figure 2.8 shows the development of the maximum slip rate in both simulations, showing that the difference between models after 100 s of simulation is smaller than 1%. Major source of this error is the presence of lower-amplitude seismic waves that reflected from the free surface and expanded along the fault. We find the 1% error acceptable as it is comparable with the numerical error related to the FD discretization.

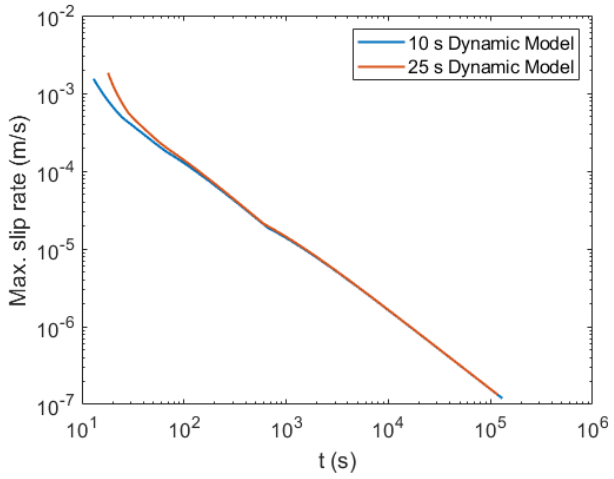

Figure 2.8: Evolution of maximum slip rates on the fault in the postseismic phase. Blue and red line denotes simulations, where the dynamic code simulates 10 s and 25 s of the coseismic rupture, respectively.

3. Bridging time scales of faulting: from coseismic to postseismic slip of the 2014 South Napa earthquake

This chapter was published as [Premus et al., 2022] in Science Advances. We made only minor corrections, notational and stylistic edits.

3.1 Introduction

Seismic and aseismic slip are two primary modes of fault behavior whose spatial distribution controls the earthquake potential of a fault and may inform on its mechanical properties. Seismic and aseismic slip tend to occur on separated areas of a fault [Marone et al., 1991], as manifested in the large-scale division of faults into creeping and locked segments and in the modest spatial overlap between coseismic slip and afterslip. Earthquakes occur in the locked portion of faults and originate in the seismogenic zone, surrounded by predominantly aseismic slip at the top and bottom. Several physical mechanisms might determine the seismic or creep behavior of a fault. For example, aseismic behavior close to the surface has been attributed to the presence of fault gouge with low confining stresses [Marone and Scholz, 1988], and the seismogenic depth is bounded by a temperature-controlled transition to plastic sliding [Scholz, 2012]. In addition, changes in lithology [Ma et al., 1997] or pore pressure [Moore, 1992, Harris, 2017] can influence the preferred type of slip.

A commonly observed form of transient aseismic slip is the afterslip that follows earthquakes in areas adjoining their seismic rupture [Marone et al., 1991, Heki et al., 1997]. There is a large variability in the amount of afterslip following different earthquakes [Melbourne et al., 2002], which indicates a complicated relationship between physical conditions on the fault and coseismic and postseismic slip. Postseismic slip can occur close to the surface [Marone et al., 1991], in areas that show a coseismic slip deficit [Kaneko and Fialko, 2011]. A well-known example of a fault that generates ample seismic and postseismic slip is the Parkfield segment of the San Andreas fault, which produced a series of Mw (moment magnitude) 6 earthquakes in the 19th and 20th centuries [Murray and Langbein, 2006]. The most recent event occurred in 2004, releasing twice as much moment postseismically than coseismically, and was a subject of physics-based studies of transient slip [Barbot et al., 2012].

Physics-based modeling, including dynamic source inversion, is one approach to advance our fundamental understanding of the partitioning between seismic and aseismic slip. Rate-and-state friction laws [Dieterich, 1979, Ruina, 1983, Rice and Tse, 1986, Nagata et al., 2012], based on laboratory experiments at relatively low slip rates, offer a framework that allows explaining both seismic and aseismic phenomena in dynamic models. A fault can be partitioned into seismic and aseismic portions by its spatially heterogeneous frictional properties [Marone et al.,

1991, Ruina, 1983, Kame et al., 2015]. In particular, steady-state friction can be velocity weakening (potentially unstable, seismic) or velocity strengthening (dominantly aseismic). The framework can be extended to higher slip rates, relevant to coseismic slip, by introducing a fast-velocity-weakening mechanism. High-speed friction experiments [Tsutsumi and Shimamoto, 1997, Di Toro et al., 2004] show that a range of fault materials weakens substantially at slip rates above 0.1 m/s [Chen et al., 2017], which has been attributed to thermally activated processes such as flash heating [Rice, 2006]. Incorporating fast-velocity-weakening friction into the rate-and-state earthquake model [Dunham et al., 2011, Ulrich et al., 2019, Harris et al., 2018] leads to qualitative changes in its behavior as dynamic strength is close to zero, and the difference between prestress and static strength increases [Rice, 2006]. Moreover, fault areas that are velocity strengthening at low slip rate may switch to velocity-weakening behavior at fast slip rates, as was suggested for the Tohoku earthquake [Noda and Lapusta, 2013] and observed in laboratory experiments under conditions with increasing normal stress [McLaskey and Kilgore, 2013]. A primary goal of the dynamic source inversion proposed here is to infer the friction properties of a fault based on observations of coseismic and postseismic slip.

The 24 August 2014 Mw 6.0 South Napa, California earthquake has a particularly well-documented abundance of coseismic and postseismic slip, making it a good target for dynamic source inversion. It ruptured one of the recently mapped branches of the West Napa fault [Wesling and Hanson, 2008]. The earthquake's right-lateral strike-slip mechanism is consistent with the orientation of this fault. The shallow part of the fault (<3 km depth) span two lithological units [Graymer et al., 2005]: The northern half is positioned on the contact between Cretaceous rocks (sandstone, melange, etc.) from the Franciscan Complex and Cenozoic sediments, while the southern half of the fault goes below the Napa River and is embedded in a layer of Quaternary sediments [Graymer et al., 2005, Floyd et al., 2016, Langenheim et al., 2010] whose thickness increases in the southward direction from 1.5 km to more than 2 km (see Figure 3.1a for the fault position with respect to the regional geology).

The 2014 South Napa earthquake is well studied, including measurements of surface slip and afterslip over the whole length of the rupture [Lienkaemper et al., 2016, DeLong et al., 2016]. Kinematic studies of coseismic and postseismic slip [Floyd et al., 2016, Dreger et al., 2015, Ji et al., 2015, Melgar et al., 2015] agree on the main source characteristics. The rupture nucleated at 10 km depth and propagated up-dip and northward for 8 to 10 s along a 13-km distance, generating strong seismic waves amplified toward the north due to the source directivity and a sedimentary basin [Ji et al., 2015]. The event produced a 12-km-long surface rupture and rapid shallow afterslip [Floyd et al., 2016, Brooks et al., 2017]. It was also followed by approximately 1000 aftershocks that occurred mostly below the coseismic rupture [Hardebeck and Shelly, 2016]. While most of the shallow coseismic slip was concentrated in the northern half of the rupture, an unusually large shallow afterslip occurred on the southern half, starting 3 hours after the earthquake and continuing over the next several months [Brooks et al., 2017]. This spatial difference in the release of shallow slip has been attributed to spatial variability of either the local geology [Floyd et al., 2016, Brooks et al., 2017] or the coseismic stress changes [Wei et al., 2015].

This paper provides a unifying dynamic model of the 2014 South Napa coseismic rupture and subsequent afterslip based on rate-and-state friction with fast-velocity-weakening effect [Dunham et al., 2011] included. To this aim, we extend the Bayesian dynamic inversion method [Gallovič et al., 2019a] to integrate seismic and geodetic data on diverse time scales from seconds to months. The inferred rupture properties reconcile and refine previous independent studies. In addition, the dynamic inversion results enable previously unexplored physical interpretations of the connection between lithology and friction properties, and insights into the role of enhanced weakening in rupture propagation and on the mechanisms of coexistence of seismic and aseismic slip on a fault. We further examine the effects of heterogeneous dynamic parameters on the rupture propagation and arrest, showing that heightened prestress drove coseismic rupture at depth, while velocity strengthening was the main arresting mechanism near the surface. We also show how spatially heterogeneous frictional rheology affects the development of both coseismic and postseismic slip in the shallow zone, affecting the time scale over which slip is released. In addition, we suggest that spatially limited afterslip had a role in triggering off-fault aftershocks, which were mainly observed below the coseismic rupture.

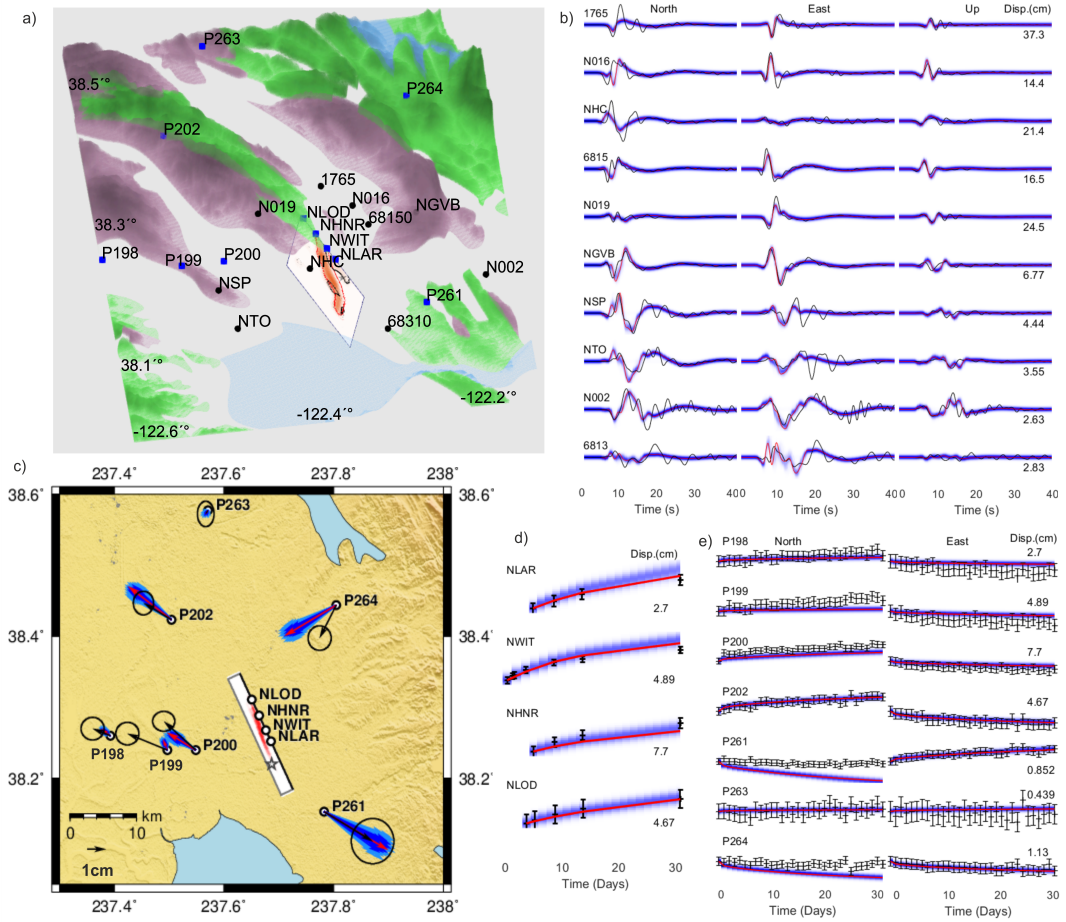

Figure 3.1: Maps and fits of coseismic and postseismic data. (a) Position of the fault with respect to the local geologic conditions (white, Quaternary sediments; green, Cretaceous rocks; purple, Cenozoic volcanic rocks), based on (27, 71) and seismic (black circles) and GPS (blue squares) stations. (b) Comparison between observed seismograms (black) and our best-fitting model seismograms (red). Kernel density estimates (KDEs) of the posteriors are displayed in blue. Station names and maximum displacements are indicated on the left and right, respectively. (c) Fit between observed coseismic GPS displacements (black arrows) and synthetic data (red arrows); KDEs are displayed in blue. Positions of the stations with their names are shown on the map (black circles) with respect to the fault (white rectangle), with total slip color-coded in white to red. Star denotes the epicenter. (d) Comparison between observed postseismic surface displacement (black) and our best-fitting model GPS (red). KDEs are displayed in blue, while errors of real data are shown as error bars. Station names are indicated on the left, and maximum displacements in centimeters are indicated on the right. (e) Comparison between observed postseismic GPS displacements (black) and our best-fitting model synthetics (red). KDEs are displayed in blue, while errors of real data are shown as error bars. Station names and maximum displacements are indicated on the left and right, respectively.

3.2 Methods

3.2.1 Friction law

In our model, coseismic and postseismic slip are governed by rate-and-state friction with fast-velocity-weakening [Dunham et al., 2011]

$$S = \sigma_n a \, \mathrm{arcsinh}\Big[\frac{\dot{s}}{2\dot{s}_0}\exp\Big(\frac{\psi}{a}\Big)\Big] \tag{3.1}$$

$$\frac{d\psi}{dt} = -\frac{\dot{s}}{L}[\psi - \psi_{SS}] \tag{3.2}$$

$$\psi_{SS} = a \log\Big[\frac{2\dot{s}_0}{\dot{s}} \, \sinh\Big(\frac{f_{SS}}{a}\Big)\Big] \tag{3.3}$$

$$f_{SS} = f_w + \frac{f_{LV} - f_w}{\Big[1 + (\dot{s}/\dot{s}_w)^8\Big]^{1/8}} \tag{3.4}$$

$$f_{LV} = f_0 - (b - a) \log\Big(\frac{\dot{s}}{\dot{s}_0}\Big) \tag{3.5}$$

Equation 3.1 gives a value of friction S for given slip rate $\dot{s}$ and frictional state variable ψ. It is in the regularized form to avoid divergence at zero slip rate [Rice and Ben-Zion, 1996, Lapusta et al., 2000], with only minor difference from the classical formulation for $\dot{s} > 0$ [Ruina, 1983]. The evolution equation (Equation 3.2) for the state variable ψ is the slip law, in which the time derivative of the state variable is proportional to its distance to a steady-state value ψ_{SS} and ratio of $\dot{s}$ and characteristic slip L. The steady-state value is calculated in Equation 3.3 from steady-state friction f_{SS} as an inverse function of Equation 3.1. The steady-state friction is defined by Equation 3.4, where it decreases from low-velocity friction f_{LV} to fully weakened friction f_w with growing slip rate $\dot{s}$, as $\sim 1/\dot{s}$ for $\dot{s} > \dot{s}_w$ due to the fast-velocity-weakening effect, following the flash-heating model [Rice, 2006]. The low-velocity steady-state friction coefficient f_{LV} defined by Equation 3.5 increases or decreases with slip rate $\dot{s}$ following the sign of the difference between the state evolution b and direct effect a coefficients. The difference $(b - a)$ in Equation 3.5 thus distinguishes the velocity-weakening $(b-a > 0)$ and velocity-strengthening $(b-a < 0)$ modes of friction [Scholz, 2012].

3.2.2 Forward problem

We simulate the coseismic rupture with the code FD3D_TSN [Premus et al., 2020]. It uses a fourth-order finite-difference method to solve the 3D elastodynamic equation. The fault boundary condition (friction) is applied on a vertical fault with the traction-at-split-nodes method [Dalguer and Day, 2007]. Free surface conditions are applied using a stress imaging technique [Graves, 1996]. We use perfectly matched layers [Collino and Tsogka, 2001] as absorbing boundary conditions. All computationally expensive routines are GPU-accelerated using OpenACC directives, yielding a speedup by a factor of 10 when comparing single GPU and single CPU runs. Accuracy of the code was tested [Premus et al.,

2020] by using community Southern California Earthquake Center/U.S. Geological Survey (SCEC/USGS) benchmarks for both slip-weakening and fast-velocity-weakening friction laws [Harris et al., 2018]. Earthquake nucleation is induced by a second-long gradual increase of prestress in a circular zone. We use a spatial grid size of 100 m, providing a sufficient resolution of the cohesive zone, and a time step of 0.003 s satisfying the Courant–Friedrichs–Lewy stability criterion. The computational domain on one side of the fault is 10 km thick. Synthetic seismograms are obtained by convolving the resulting slip rates with Green's functions precalculated using the Axitra code [Cotton and Coutant, 1997].

Postseismic slip is simulated in a quasidynamic approximation, replacing the inertial term of the elastodynamic equation by a radiation damping on the fault [Rice, 1993]. We use a boundary element approach with a precalculated velocity-stress interaction kernel between fault nodes, assuming a vertical fault in a homogeneous medium [Okada, 1985]. This reduces the problem to a set of ordinary differential equations for displacements and state variables [Perfettini et al., 2003, Gallovič, 2008, Galvez et al., 2021]. We solve it by a Runge-Kutta method of fifth order with variable time steps on an undersampled grid with a 400 m spatial step. This quasidynamic postseismic modeling is used after the maximum slip rate in the finite-difference coseismic simulation falls below 1 mm/s. We tested the viability of the transition by postponing it by 10 s to 1 min, yielding only a negligible (below 1%) difference in the simulated long-term slip. Both predicted coseismic and postseismic GPS displacements are obtained by convolving the slip with precalculated Green's functions. We note that the positions of the alignment arrays, NLAR, NWIT, NHNR, and NLOD, that measure the surface slip directly above the fault would not fit with our simplified planar geometry. Therefore, we artificially moved their positions to coincide with the position of the surface rupture on our planar fault, preserving their distance from the epicenter. We model the arrays as if they were GPS stations located at a 50 m distance from the fault with displacement equal to half of the measured slip.

3.2.3 Parameterization

The fast-velocity-weakening rate-and-state friction law involves a challenging number of potentially free parameters in the dynamic inversion, increasing the dimension of the model parameter space and increasing computational requirements. These include parameters of the rate-and-state friction a, b, f_0, s_0, and L; additional parameters governing the fast-velocity-weakening effect f_w and s_w; stressing conditions at the fault σ_n and T_0; and initial values s_{ini} and ψ_{ini}. We assume a purely strike-slip fault so that T_0 and s_{ini} are non-zero only in the horizontal direction. All parameters are thus spatially heterogeneous 2D scalar fields across the fault.

We use several relations and assumptions to limit the actual number of model parameters in the inversion and keep the inversion computationally tractable. Normal stress σ_n is set to be depth dependent, rising from 1 MPa at the surface to 100 MPa at 5 km depth and held constant at greater depth, where further depth increases in pore pressure and hydrostatic pressure are assumed to balance out [Rice, 1993]. Nonzero normal stress at the surface substitutes the cohesion we did not include directly in the modeling. Models with friction coefficient

f are equivalent to models with cohesion c and friction coefficient $\tilde{f}$ such that $f = \tilde{f} + c/\sigma_n$, provided that cohesion weakens in the same way as friction. At shallow depth (low σ_n), $f_0 > 1$ can thus be accommodated with reasonable values of c ($\sim$1 MPa) and $\tilde{f} < 1$.

The fully weakened friction coefficient f_w is set to 0.2, as observed in laboratory experiments [Boulton et al., 2017]. Any other value of f_w can be accommodated a posteriori by a straightforward modification of the results; the adjusted initial stress T_0 would, in that case, be calculated by addition of the factor $\sigma_n[f_{w(new)} - 0.2]$ to the initial shear stresses constrained by our inversion.

The reference slip velocity s_0 is associated with a steady-state friction coefficient equal to f_0. Since it is an arbitrary reference, we set it to 10^{-6} m/s as in other rate-and-state dynamic models [e.g., Dunham et al., 2011, Ulrich et al., 2019, Pelties et al., 2014]. The initial value of the state variable ψ_{ini} is related to T_0 and s_{ini} through Equation 3.1. We calculate ψ_{ini} at the beginning from Equation 3.1, following the approach in the SCEC/USGS benchmark TPV104 [Harris et al., 2018]. We fixed $s_w = 0.1$ m/s and $s_{ini} = 10^{-12}$ m/s in velocity-weakening ($b - a > 0$) areas of the fault. The former is supported by experiments, and the latter stems from the assumption that the coseismic region is locked before the onset of the earthquake. In contrast, in the velocity-strengthening areas, where the fault is supposed to creep at higher slip rates before the start of the earthquake (at least at 10^{-10} m/s) [Evans et al., 2012], we let s_{ini} free. Similarly, we let s_w free in the strengthening zone to allow the rupture to stop.

In the end, the reduced set of dynamic model parameters to be determined by the inversion procedure are T_0 , a, b, f_0 , and L as 2D fields, and s_w and s_{ini} as 2D fields on the smaller (velocity-strengthening) portion of the fault. For the purposes of the inversion, we parametrize the spatial distribution on an equidistant grid of 12 $\times$ 9 control points, from which the parameters are bilinearly interpolated onto the grids for the dynamic and quasidynamic simulations. The 2D fields are supplemented by four more free parameters describing our nucleation procedure realized by a 1-s-long gradual increase of prestress in a circular zone—the position of its center, its radius, and the added stress.

3.2.4 Inverse problem

We formulate the inverse problem in the Bayesian framework [Gallovič et al., 2019a, Gallovič et al., 2020, Kostka et al., 2022]. We assume uniform prior PDFs for the model parameters in wide intervals of permissible values (Table 3.1). The data are considered to have Gaussian distributions of errors with SDs of 5 cm and 2.5 mm for seismograms and GPS, respectively. We sample the posterior probabilities using the Markov chain Monte Carlo (MCMC) parallel tempering algorithm [Sambridge, 2013], accepting proposed models according to the Metropolis-Hastings rule. We used a modified version of the inversion code fd3d_tsn_pt. This code has been previously validated for slip-weakening friction law and only seismic data using synthetic tests [Gallovič et al., 2019a] and applied to the 2016 Amatrice [Gallovič et al., 2019b] and 2020 Elazığ earthquakes [Gallovič et al., 2020]. The present application required implementing the modified forward model and parameters.

We accelerated the inversion progress by starting from a reasonable model

Quantity	**Label**	**Minimum value**	**Maximum value**
Shear prestress (horizontal)	T_0	10^3 Pa	10^9 Pa
Direct effect parameter	a	0.001	0.1
State evolution parameter	b	0.001	0.1
Reference friction at velocity	f_0	0.1	2
Characteristic slip distance	L	0.1 m	2 m
Weakening velocity	$\dot{s}_w$	0.1 m/s	3 m/s
Initial velocity (horizontal)	$\dot{s}_{ini}$	10^{-13} m/s	10^{-7} m/s
Along-strike position of the nucleation	h_x	14.5 km	16.5 km
Depth of the nucleation	h_y	10 km	14 km
Radius of the nucleation patch	r_{nucl}	400 m	1000 m
Stress increase in the nucleation patch	σ_{nucl}	1%	20%

Table 3.1: Minimum and maximum values of prior uniform distributions of inverted parameters. Note that $\dot{s}_w$ and $\dot{s}_{ini}$ have uniform prior distribution in the velocity-strengthening regions only, being constant in the velocity-weakening areas.

that was relatively homogeneous with velocity-weakening friction at the central square-shaped portion of the fault and velocity-strengthening friction on all edges. From there, we allowed the parallel tempering MCMC approach to explore the model space. We manually intervened several times by optimizing the prestress, nucleation, and frictional parameters to find a model with positive variance reduction. After that, we explored the model space by running the MCMC sampling on an IT4I cluster with four Nvidia Tesla V100 GPUs and in-house computers with three GPUs (Nvidia 2080Ti), with each forward simulation taking about 40 s in both cases. The total number of visited models was high (∼500,000). The final set consists of ∼7500 accepted models with a posterior probability density value larger than 5% of the pPDF maximum.

3.3 Results

Our Bayesian dynamic inversion aims at constraining the friction parameters and initial fault stresses that govern the space-time evolution of both seismic and postseismic slip and produce ground motions consistent with seismic and geodetic data. We assume a vertical planar fault of 20 km × 15 km size that reaches the surface and has a strike of 165° (Figure 3.1a), which is a simplified representation of the geometry constrained by the position of the surface rupture and relocated aftershocks [Hardebeck and Shelly, 2016]. The set of dynamic model parameters determined by the inversion procedure is shear prestress T_0, direct effect parameter a, state evolution parameter b, reference friction f_0, and characteristic slip distance L as two-dimensional (2D) fields, and weakening velocity s_w and initial velocity s_{ini} as 2D fields on the smaller (velocity-strengthening) portion of the fault. The friction law, simulation techniques, data errors, model parameterization, and sampling of the posterior probability density function (pPDF) are

described in Methods (Section 3.2). The result of the inversion is an ensemble of models with spatially varying dynamic rupture parameters, statistically representing samples of the pPDF.

We model data from 10 near-source strong-motion accelerometers, seven continuous GPS stations, and four alignment arrays capturing surface fault offsets [Lienkaemper et al., 2016, McFarland et al., 2015] at vineyards crossing the fault (see Figure 3.1a for their position with respect to the fault). In addition, forward modeling of a larger dataset of coseismic GPS displacements is used for verification of the inversion results. We use a 1D layered crustal velocity profile based on the GIL-7 model [Stidham et al., 1999] with added low-velocity surface layers. We consider the frequency range of 0.05 to 0.5 Hz for the seismograms and daily sampled GPS displacements (the original dataset from UNAVCO; `www.unavco.org`). Alignment array measurements were irregular in time, so we use all accessible data points from four sites where substantial afterslip was detected (initial measurements were 2 to 5 days after the earthquake, two more in the first 10 days, and two more between 10 and 30 days). Data from both GPS and alignment arrays are considered in the first 30 days after the earthquake.

Figure 3.1 (b and c) compares the coseismic data with our best-fitting model, which has a variance reduction of 0.49 for seismograms. The figure also displays the statistical variability of the simulated data due to the model uncertainty using kernel density estimates (KDEs) of the posteriors, representing histograms smoothed by a Gaussian function [Zambom and Dias, 2013]. The fit is generally good; we attribute the major portion of the data misfit to unmodeled 3D Earth structure in the velocity model and nonplanar nonvertical geometry of the real fault. Postseismic displacements at GPS stations and alignment arrays are displayed in Figure 3.1, d and e, respectively. We note that the displacements recorded by the GPS stations are of the order of 1 cm only due to the rather large distance of the stations from the fault and the moderate size of the earthquake. Nevertheless, the fit is still good despite postseismic displacement amplitudes being much lower than amplitudes of seismograms or alignment array displacements. The fit of the coseismic GPS displacements used for verification is comparable with the fit of those used for inversion (see Figure 3.2). The surface slip measurements provide major constraints on afterslip. They are fitted very well due to their relatively high implicit weights in the inversion and lack of direct trade-offs with the other data. The total variance reduction of all GPS data is 0.63.

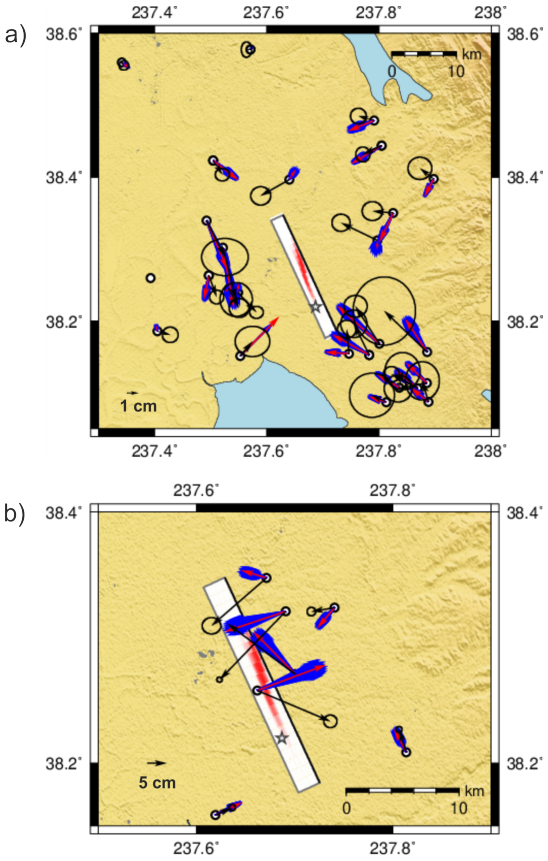

Figure 3.2: Comparison of observed coseismic GPS displacements of stations (black arrows with ellipse denoting 95% confidence interval) from the dataset in (29) and synthetic data (red arrow for MAP and KDEs in blue). Positions of the stations shown on the map (black circles) with respect to the fault (white rectangle) with total slip color-coded in white-to-red. Star denotes the epicenter. (a) Stations farther from the fault; (b) stations closer to the fault.

3.3.1 Kinematic properties and stress drop

Coseismic ruptures in our model ensemble nucleate at a mean depth of 10.46 ± 0.30 km and propagate upward and to the north. They create two major patches of coseismic slip at 3 and 6 km depths (Figure 3.3a), coinciding with the maximum stress drop areas, which locally reach 50 MPa (Figure 3.3d). The coseismic rupture propagates for about 8 s at an average speed of ∼2.4 km/s, releasing a seismic moment of (1.97 ± 0.10) × 10^{18} Nm. More than 90% (1.9 × 10^{18} Nm) of the moment is released within the first 5 s. Rise time fluctuates between 0.5 and 1 s and increases above 1 s in the shallowest 2 km (Figure 3.4). The rupture reaches the surface, over a length of more than 5 km. The final ruptured area attains a ribbon-like shape of width ∼5 km and length ∼12 km, and its major axis shows an unusual oblique orientation. Areas of shear stress increase (Figure 3.3d) concentrate around the rupture edges.

Postseismic slip evolves continuously after the coseismic slip around most of the rupture area. In particular, shallow afterslip starts within 20 to 24 hours from the southern side of the coseismic rupture (∼8 km along strike; see Figure 3.3b) and expands rapidly in the first 3 days at ∼1.5 km/day toward the south. Expan-

sion continues over the whole modeled period of 30 days, albeit with decreasing rate. This produces a substantial (∼14 MPa) postseismic stress drop comparable with coseismic stress drop at the same depths. We also observe ∼10 cm of shallow postseismic slip even at the northern (coseismically ruptured) portion of the fault (Figure 3.3, a and b), in agreement with the shallow slip measurements [Lienkaemper et al., 2016].

Smaller patches of notable afterslip (with a maximum of ∼0.4 m) are located at about 7.5 km depth, partially overlapping with coseismic rupture. Some of our models show additional patches of afterslip further away from the earthquake, which we consider unconstrained due to their highly variable occurrence among models and minimal impact on synthetic data. Overall, the postseismic slip increases the total seismic moment of the earthquake by ∼40%, with a ∼15% increase happening during the first day after the earthquake (see Figure 3.5). Deep postseismic slip mostly happens in the first week after the earthquake, while shallow slip unfolds over a longer period of time (see Figure 3.5).

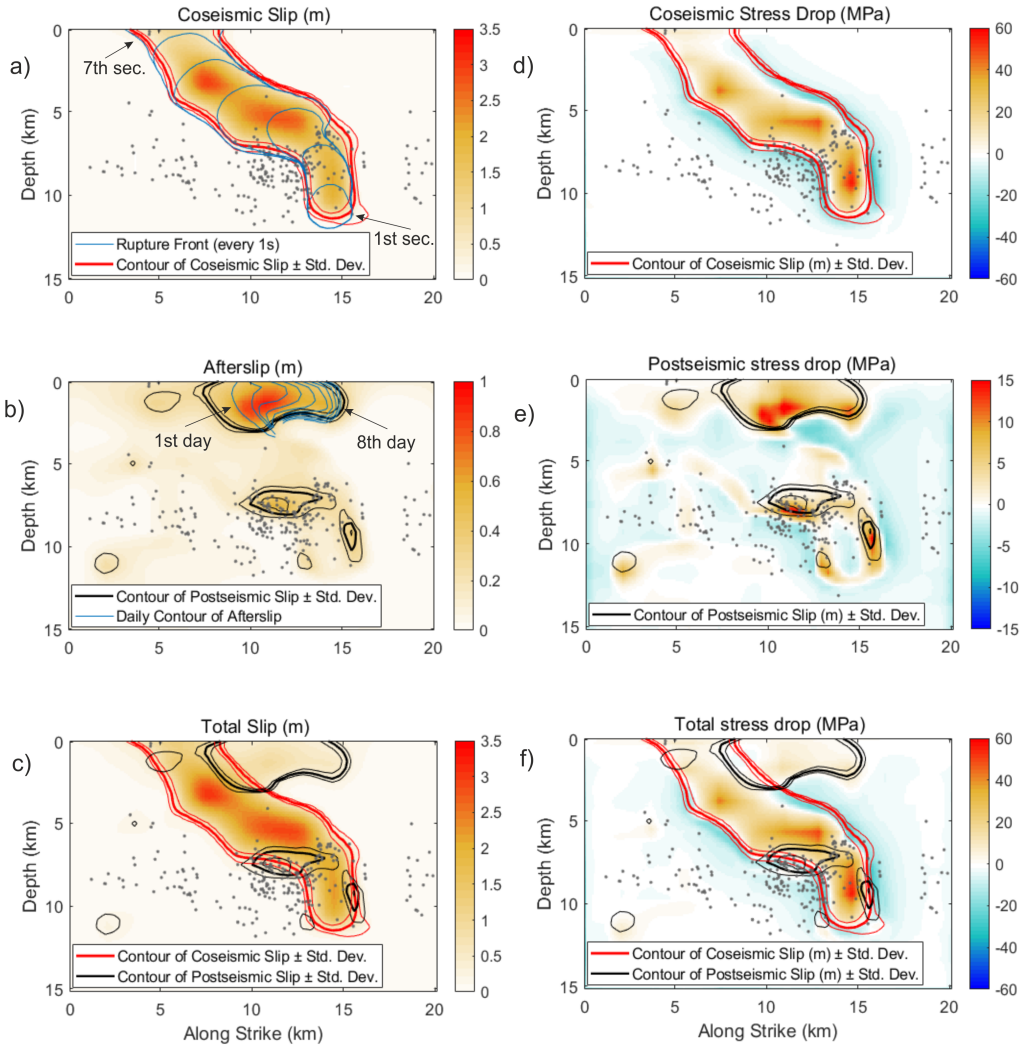

Figure 3.3: Kinematic rupture parameters and their statistics. Ensemble averages of (a) coseismic slip, (b) afterslip, and (c) total slip on the fault. Blue lines in the coseismic slip and afterslip map indicate the rupture front and the tip of the shallow afterslip in 1-day increments after the coseismic rupture, respectively. Ensemble averages of (d) coseismic, (e) postseismic, and (f) total stress drop. Contours (threshold of 0.3 m) of slip (red) and afterslip (black) with thinner lines denoting SD are displayed in all six panels. Gray dots represent aftershocks (Northern California Earthquake Data Center) with a fault-perpendicular distance of <5 km.

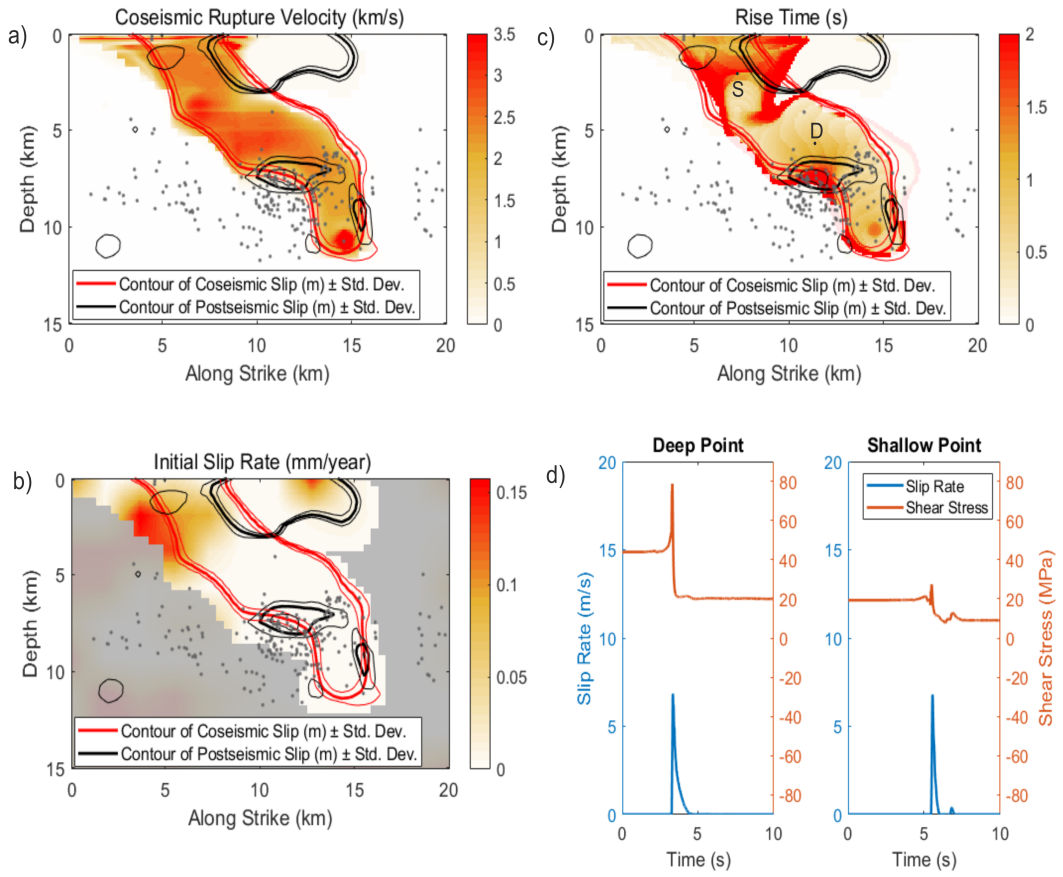

Figure 3.4: (a-c) Ensemble average of coseismic rupture velocity (calculated from the eikonal equation), initial velocity $\dot{s}_{ini}$, and rise time (calculated as difference between times when 5% and 95% of slip is achieved). Gray dots denote the aftershocks. Red and black lines denote contours of slip and afterslip, respectively. Points in (c) denote positions of the Deep (D) and Shallow (S) points where slip rates and stresses are shown in panel d. (d) Time evolution of horizontal shear stress (red line) and horizontal slip rate (blue line) in points shown in panel c.

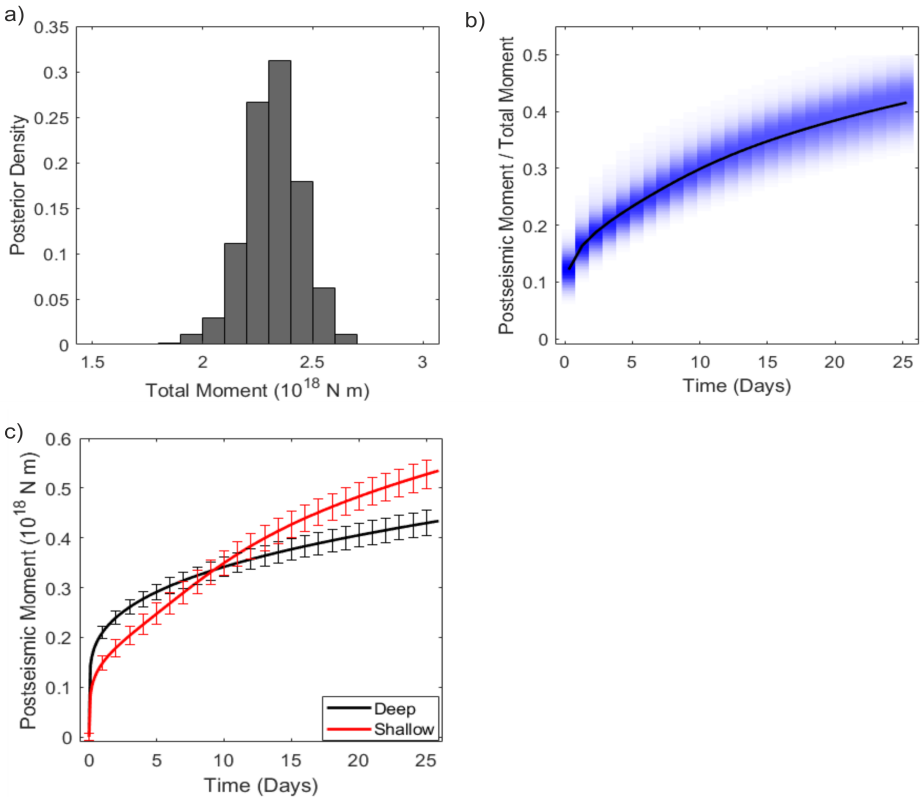

Figure 3.5: (a) Histogram of the ensemble total scalar moments. (b) Time evolution of the ratio between postseismic and coseismic scalar moments. Black line denotes ensemble average, kernel density estimates are shown in blue. (c) Time development of the shallow (red, upper 4 km of the fault) postseismic moment and deeper (black, below 4 km depth). Lines denote ensemble average, error bars denote standard error.

3.3.2 Frictional properties

The rupture properties described above stem from the dynamic rupture models, whose parameters are constrained by the inversion. A parameter of particular interest is $(b - a)$, which quantifies the relative importance between direct and evolution effects of rate-and-state friction, and controls the stability of slip: Positive values are associated with velocity-weakening frictional behavior and unstable slip, while negative values imply velocity strengthening and stable slip. Another important dynamic parameter is initial shear stress T_0. We show ensemble averages of spatial distributions of $(b - a)$ and $T0$ along the fault in Figure 3.8 (a and b) and their uncertainties in Figure 3.8 (c and d), respectively. Figures 3.6 and 3.7 show all the other inverted parameters. We discuss only dynamic parameters in the slip area and closely adjoining regions of the fault, where we can consider them well constrained by data. The along-fault width of this zone of interest expands from 5 to 6 km at depth to 15 km near the surface due to the presence of substantial shallow afterslip. To facilitate discussion about the depth dependence of friction, we also show depth profiles of selected parameters in Figure 3.8e, calculated as horizontal averages over the slip region.

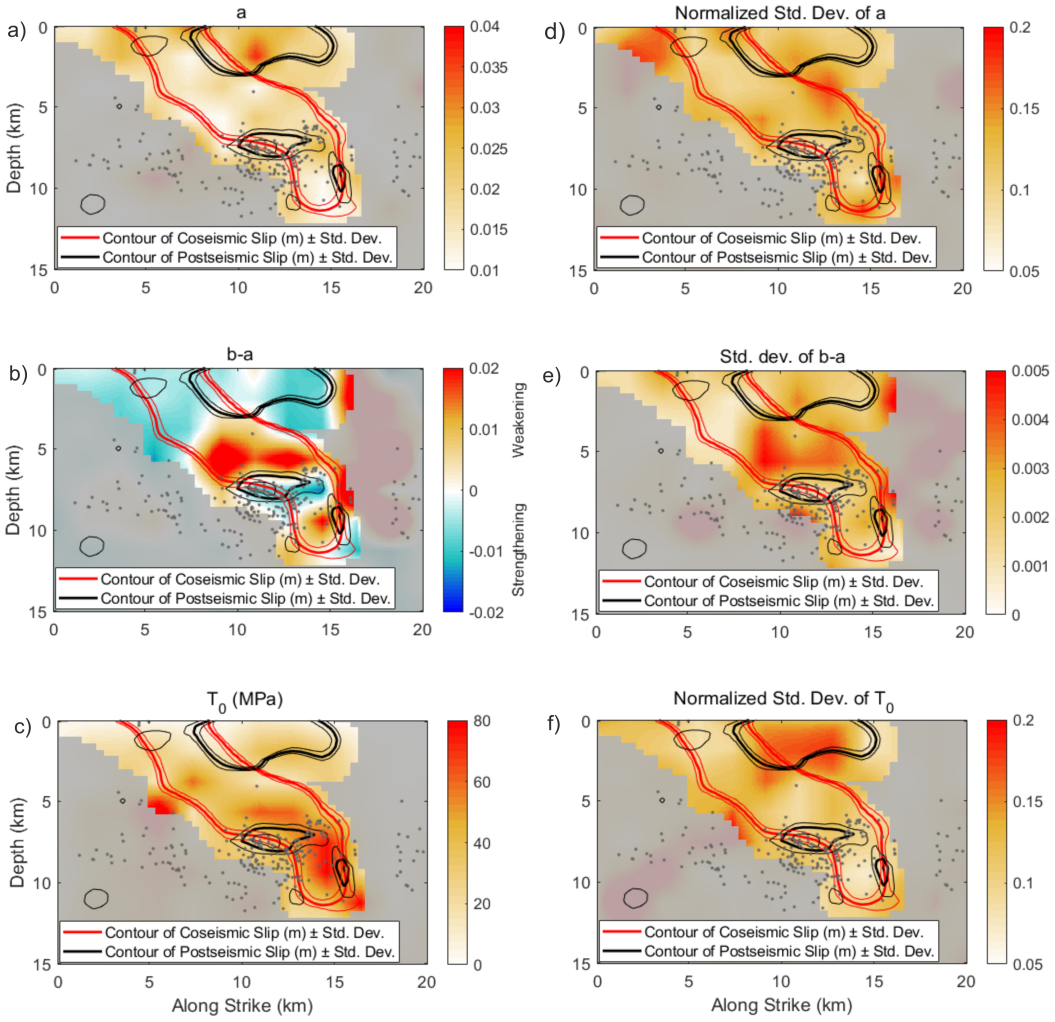

Figure 3.6: (a-c) Ensemble average of a, $(b-a)$, and T_0. Gray dots denote the aftershocks. Thick red and black lines denote contours of mean slip and afterslip, respectively, while thin lines denote standard deviation contours of the same. (d) Normalized standard deviation of a. (e) Standard deviation of $(b-a)$. (f) Normalized standard deviation of T_0.

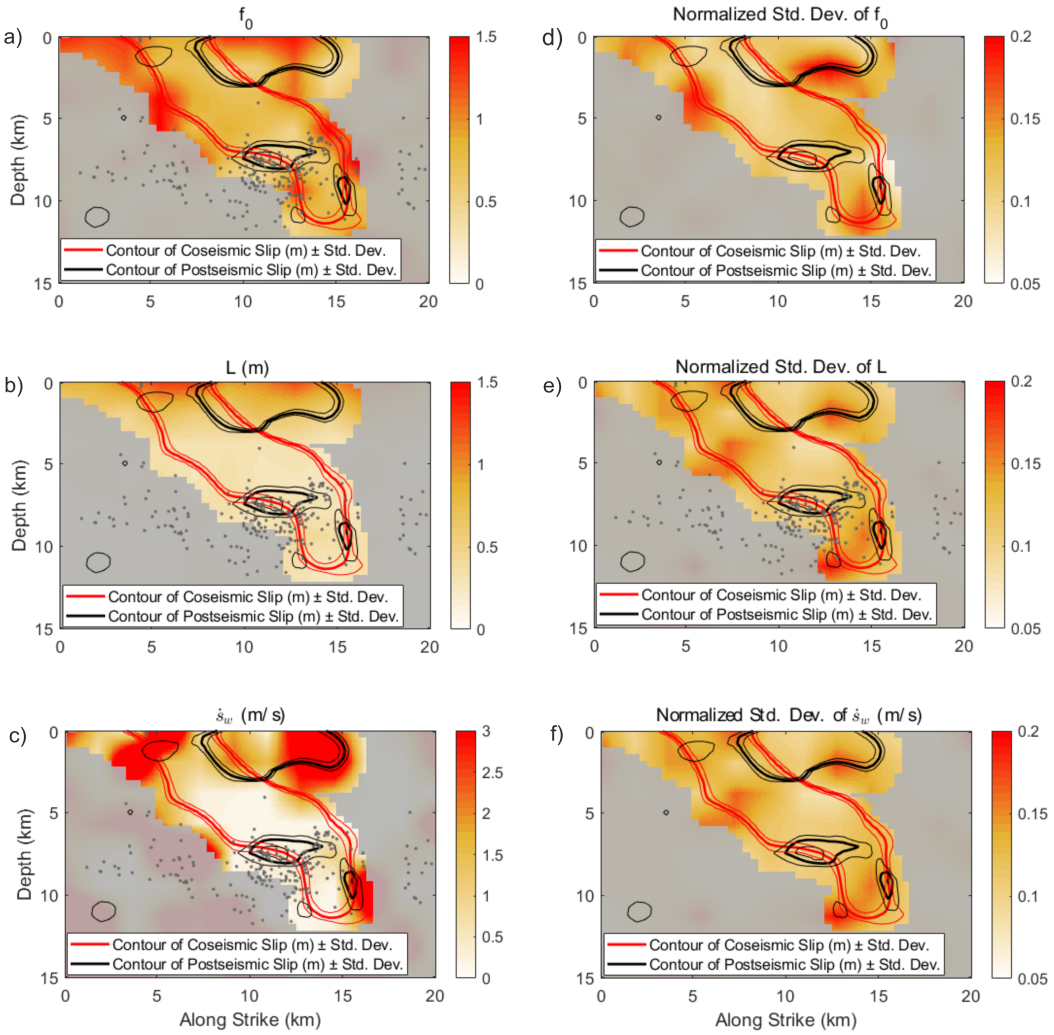

Figure 3.7: (a-c) Ensemble average of reference friction, L (m), and weakening velocity (m/s). Gray dots denote the aftershocks. Red and black lines denote contours of slip and afterslip, respectively. (d-f) Normalized standard deviations of reference friction,L (m), and weakening velocity (m/s).

Stresses in the shallow zone, above 5 km depth, decrease with decreasing depth. This is the case for both the normal stress set a priori (see Section 3.2 Methods for details) and the shear stress constrained by the inversion. The shallow zone hosts a combination of frictional parameters that limit rupture propagation and stabilize the fault, reducing both rupture speed and peak slip rates: velocity-strengthening rheology, increasing characteristic slip distance L up to $\sim$1.5 m, weakening velocity up to 3 m/s, and values of reference friction f_0 above 1. We note that the large values of f_0 found at shallow depth are unusual for rocks but can be attributed to cohesion (see Section 3.2 Methods). The horizontal transition zone between coseismic and postseismic rupture areas (7 to 12 km along strike) is characterized by low prestress and more velocity-neutral friction ($b - a$ close to zero), and overlaps with both a change in lithology and a geometrical feature where the mapped fault starts to bend more toward the west. The strengthening rheology of the afterslip area is more pronounced in the south with

$(b-a)$ ∼-0.01 as opposed to -0.005 in the northern part. The high relative SD of T_0 in the shallow postseismic zone is a manifestation of a strong trade-off between T_0 and f_0 (Figure 3.9a)—we note that the two apparent clusters in Figure 3.9a are caused by imperfect posterior sampling.

At greater depths (Figure 3.8e), the main coseismic rupture area is dominated by velocity-weakening friction ($b-a>0$), low values of the rate-and-state characteristic slip distance L ∼0.25 m, and weakening velocity 0.1 m/s, while reference friction f_0 is still relatively high (∼0.75). The $(b-a)$ parameter has higher uncertainty here than in other (strengthening) parts of the fault, most likely due to the dominant fast-velocity-weakening effect at high slip rates. On the other hand, the relative SD of prestress (∼0.01) is minimal in the coseismic zone, as it is well constrained by seismic waves originating from this area.

Substantial heterogeneity in dynamic parameters exists around the 7.5 km depth overlapping with the patch of notable deep afterslip. Friction becomes velocity strengthening due to the increase in a, while f_0 decreases to 0.55. Other dynamic parameters (L,weakening velocity) have values similar to those in the coseismic region. The fracture and radiated energies are (9.2 ± 0.8) and (4.5 ± 0.7) MJ/m 2, respectively. The radiation efficiency of the earthquake is thus 0.33 ± 0.11.

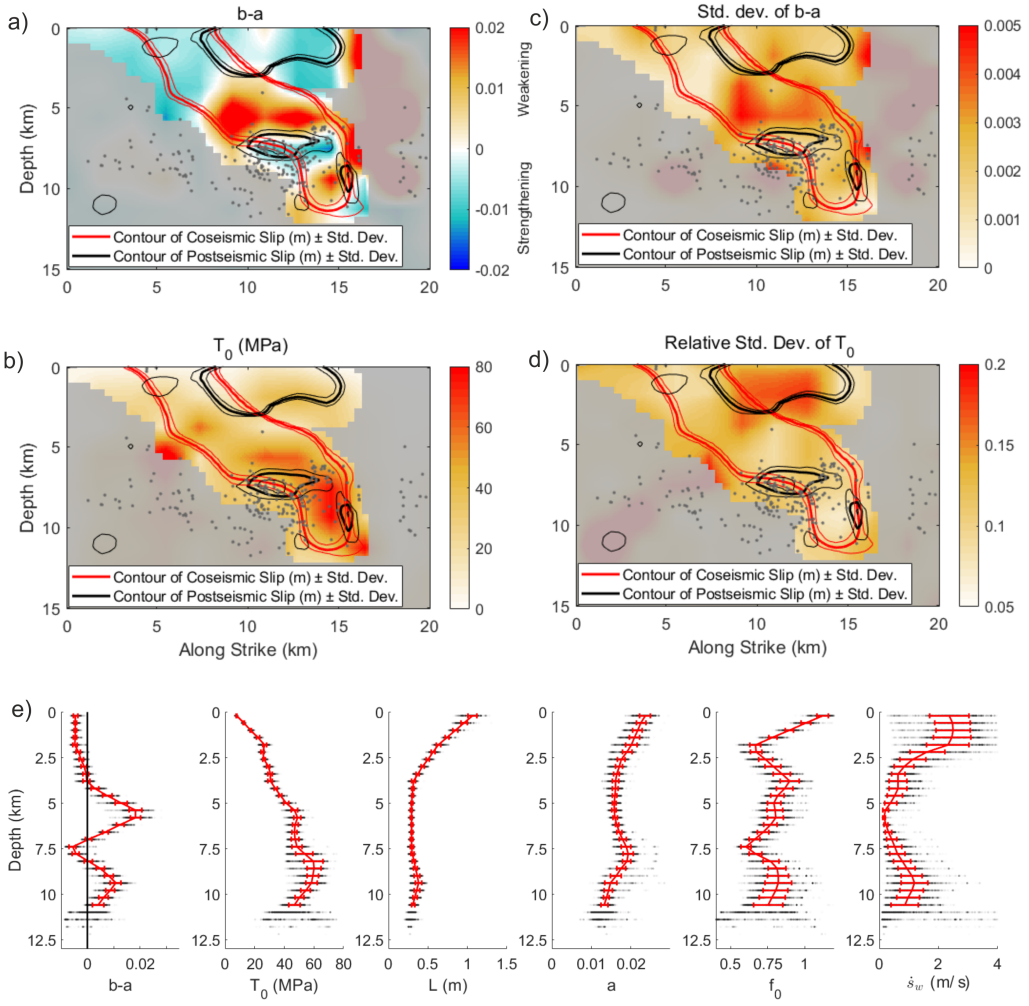

Figure 3.8: Selected dynamic parameters and their statistical properties. (a) Ensemble average of $(b-a)$. Gray dots denote the aftershocks as in Figure 3.3. Red and black lines indicate contours of slip and afterslip, respectively. (b) SD of $(b-a)$. (c) Same as (a) but for prestress T_0 . (d) Same as (b) but for relative SD of T_0. (e) Horizontal averages of $(b-a)$, T_0, characteristic slip L, a, reference friction f_0, and weakening velocity $\dot{s}_0$ on the ruptured part of the fault. Black dots denote averages of individual ensemble models, while the red line with error bars show ensemble mean and SD, respectively. Vertical black line denotes $(b-a) = 0$. For the remaining parameters, see Figure 3.7

3.4 Discussion

We have conducted a Bayesian dynamic inversion of the 2014 South Napa earthquake, creating a set of ∼7500 models that help explain both coseismic and postseismic data in a unified framework of the rate-and-state fast-velocity-weakening friction law. The model describes frictional behavior over a wide range of time scales, from coseismic seconds to postseismic weeks. The simulations are enabled by a combination of fully dynamic and quasidynamic modeling of the coseismic

and postseismic phases, respectively. The resulting main source features are consistent with those identified by previous analyses of the coseismic and postseismic data. In particular, the inferred coseismic upward and northward rupture propagation with two main patches of slip and the position of substantial shallow afterslip are consistent with published measurements [Lienkaemper et al., 2016, DeLong et al., 2016, Brooks et al., 2017] and kinematic models [Floyd et al., 2016, Dreger et al., 2015, Ji et al., 2015, Wei et al., 2015, Barnhart et al., 2015].

The joint modeling of earthquake slip and afterslip allows us to constrain dynamic parameters on larger portions of the fault than only coseismic dynamic inversion would. This is enabled by the fact that inferred coseismic and postseismic slip are spatially complementary, although some afterslip takes place in the coseismic area, especially near its border. The central part of the coseismic zone is dominated by velocity-weakening ($b - a > 0$) friction. Still, the rupture also propagates through velocity-strengthening ($b - a < 0$) areas near the free surface and above the hypocenter at about 7.5 km depth. The shallow zone is of particular interest because it hosts a transition from seismic to aseismic slip, which occurs over a short distance of 1 km, in agreement with the surface measurements. In addition, the shallow afterslip rate is spatially heterogeneous, being faster near the coseismic zone than further away. These complexities are encoded in the dynamic parameters, in particular $(b - a)$. The deeper strengthening zone not only ruptured coseismically but also hosted notable afterslip, triggering aftershocks off the fault and below the coseismic rupture. Below we discuss and interpret those important features in detail.

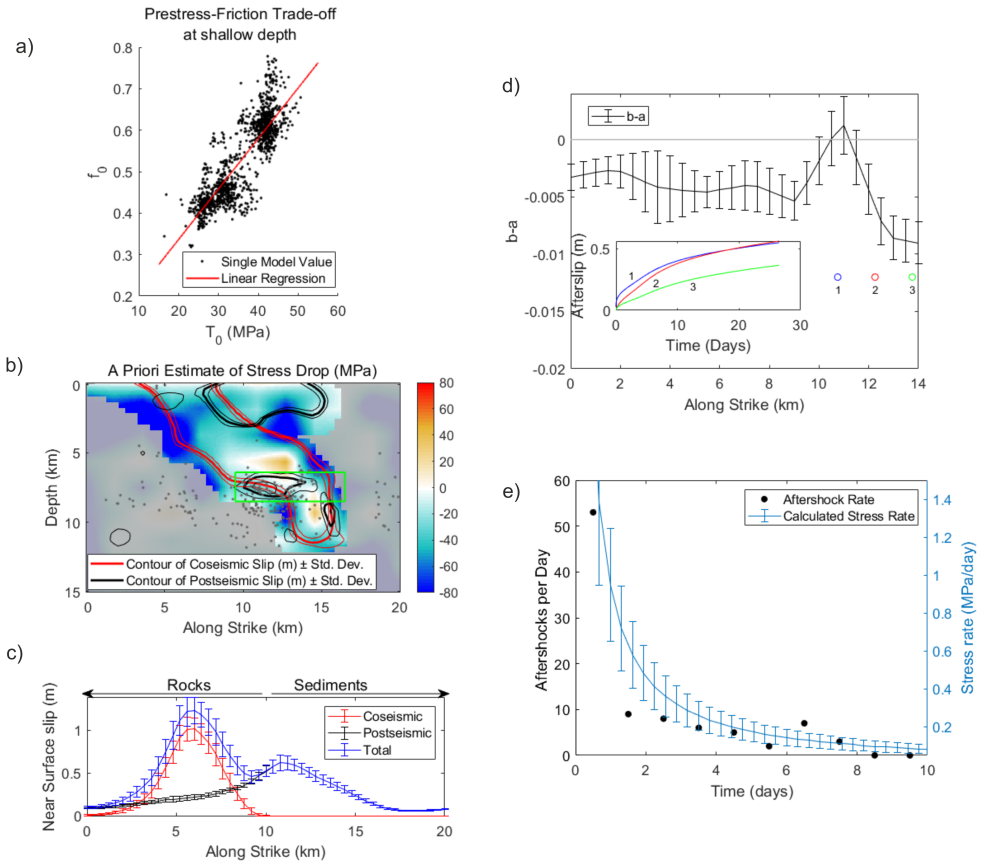

Figure 3.9: Plots documenting various modeling features for discussion. (a) Scatter plot of local dependence between T_0 and f_0 at a position located 11.5 km along strike and at 1.5 km depth. (b) A priori estimate of dynamic stress drop calculated as prestress T_0 minus steady-state friction with f_{SS} at $\dot{s} = 0.1$ m/s as friction coefficient. (c) Along strike distribution of coseismic slip (red), afterslip (black), and total slip (blue) at 200 m depth. Error bars denote the ensemble mean and SD. (d) Ensemble mean and SD of $(b - a)$ at 200 m depth. Circles denote the along-strike position of three points, for which the inset shows the afterslip development. (e) Development of stress rate (error bars showing ensemble mean and SD) and the number of aftershocks per day (black points) in the deep postseismically slipping area denoted by the green rectangle in (b).

3.4.1 Coseismic rupture arrest

We find evidence for different mechanisms driving rupture arrest at deep and shallow depths. At seismogenic depths, in areas between 5 and 10 km depth that are well within the rupture, slip rates exceed the weakening velocity, and thus, friction drops close to the fully weakened friction coefficient f_w. This is not the case close to the rupture edges as we demonstrate in Figure 3.9b, which shows an estimate of the dynamic stress drop assuming slip rate lower than the weakening velocity. The large negative stress drop values at the edges suggest that the arrest is primarily driven by low prestress T_0 with respect to the residual strength. As the rupture approaches the low-prestress barrier, it slows down, and

its peak slip rate diminishes [as expected from theoretical arguments [Gabriel et al., 2013]], which eventually prevents the fast-velocity-weakening effect. Closer to the surface, the strength excess decreases, and the velocity-strengthening effect gains importance as the rupture arrest mechanism by keeping the peak slip rates below the fast-velocity-weakening limit. This is especially the case in the shallow southern portion of the fault.

The velocity-strengthening zone at 7.5 km depth is an exception to this picture, as the difference between initial stress and reference friction is much lower there (see also the small stress drop estimate in Figure 3.9b). This feature not only slows down the coseismic rupture but also produces a patch of large afterslip (Figure 3.3e). Low prestress is our preferred rupture arrest mechanism at large depth because the alternative, velocity-strengthening friction, would induce larger deep afterslip that would be inconsistent with the GPS data.

3.4.2 Interplay between coseismic and postseismic ruptures at shallow depths

The unique feature of our modeling is to adopt a single friction law for both the coseismic and postseismic ruptures, in contrast to their independent treatment in previous works [e.g., Langbein et al., 2006, Fukuda et al., 2009, Twardzik et al., 2021]. In the case of the South Napa earthquake, the shallow zone above 3 km depth hosts an abrupt horizontal change from seismic to aseismic rupture. The northern portion of the shallow fault ruptured coseismically, switching within $\sim$1 km to the south to primarily postseismic rupture (Figure 3.8b). The total shallow slip (coseismic and postseismic) has two local maxima, one in the coseismic zone at around 6 km along strike and one in the postseismic zone at 11 km along strike (Figure 3.9c). The local minimum ($\sim$9 km along strike) coincides with the border between the coseismic and postseismic slip areas and is associated also with nearly zero total stress drop (Figure 3.3f). These characteristics are well constrained by data from the alignment arrays and are in good agreement with previous models of shallow slip [e.g., Lienkaemper et al., 2016].

The distribution of frictional properties in our results (Figures 3.8b and 3.9b) shows that the whole shallow part of the fault is velocity strengthening, including the coseismic portion. This feature of rate-and-state dynamic models is implied by physical mechanisms (low normal stresses, temperature, and unconsolidated gouge) described in Introduction. Further modeling investigations [Kaneko et al., 2008] suggest that this shallow layer substantially reduces the potential for large coseismic surface rupture and accompanying large seismic wave radiation (unusual for natural earthquakes) in comparison with purely velocity-weakening models.

The along-strike distribution of $(b-a)$ (Figures 3.9d) shows a clear difference between the coseismic ($\sim$-0.005) and postseismic ($\sim$-0.01) areas. This change in $(b-a)$ coincides with the transition between Cretaceous rocks to the north and younger Quaternary sediments in the south (Figures 3.1a and 3.9a). As the unusual properties of the 2014 South Napa earthquake (shallow afterslip, position of the coseismic slip) are at least partially governed by this change in frictional rheology, the rupture propagation was clearly affected by the transition between the two lithological units. This division between Cretaceous rocks and Quaternary sediments happens only in the near surface region, while the rest of coseismic slip

occurred at larger depths where the lithology is composed of Cretaceous rocks [Graymer et al., 2006]. After the coseismic rupture propagates through this deeper area and arrives at the shallow layer, it continues only in the rock (northern) part of the fault, being impeded in the (southern) sedimentary part of the fault where a complementary afterslip develops subsequently. We suggest this mechanism to be responsible for the ribbon-like shape of the coseismic rupture.

3.4.3 Variability in the shallow postseismic slip

The evolution of shallow postseismic slip is spatially heterogeneous. Figure 3.9d shows the afterslip at three nearby points located from 10 to 15 km along strike. The temporal behavior varies in both amplitude and characteristic decay time. This is well constrained by the surface data and was also identified in kinematic inversions of afterslip [Floyd et al., 2016]. In our dynamic model, the difference is facilitated by along-strike variations of $(b-a)$ (see Figure 3.9d). The value of $(b-a)$ affects the time scales over which afterslip develops, as can be seen from a simple spring slider model [Marone et al., 1991, Perfettini and Avouac, 2004, Perfettini and Ampuero, 2008], for which afterslip $s(t)$ develops logarithmically with time t

$$s(t) = \sigma_n \frac{a-b}{k} log(\frac{v_i t}{\sigma_n \frac{a-b}{k}} + 1) \tag{3.6}$$

In addition to $(b-a)$, the temporal evolution of afterslip depends on effective normal stress σ_n, stiffness k (that scales with shear modulus μ and the inverse of patch size), and initial velocity v_i. The normal stress and stiffness can be assumed constant in the horizontal direction (with the potential exception of lateral variations in fluid pressure that are beyond the scope of this paper), while the initial velocity is higher at the northern part, where the slip initiated during the coseismic phase.

We show the development of shallow afterslip in Figure 3.9d, as calculated at three points near the surface (at 200 m depth) located from 10 to 15 km along strike. The positions were chosen to show the impact of different values of $(b-a)$ changing from $\sim$0 to -0.01 over 2 km. Afterslip starts much quicker close to the coseismic rupture where $(b-a)$ is close to zero. The characteristic decay time of afterslip then clearly increases further to the south as $(b-a)$ approaches -0.01. The afterslip develops under non–steady-state conditions in 3D models, and therefore does not entirely conform to the simplified logarithmic formula derived for a 1D spring slider, but its basic properties do hold. This short-distance variability in afterslip is a further example of the strong impact of fault lithology on rupture development. Whether it is driven by small-scale changes in mineral composition or pore pressure along the boundary between rocks and sediments remains an open issue.

3.4.4 Interplay between coseismic and postseismic rupture in the deep velocity-strengthening zone

The velocity-strengthening zone at 7.5 km depth (Figure 3.8b) is a major finding of our modeling. The zone manages to rupture coseismically due to the lowered

friction f_0. Coseismic slip (and stress drop) is notably lower here than in other (velocity-weakening) parts, which is consistent with coseismic kinematic inversions [Dreger et al., 2015, Ji et al., 2015]. Upward propagating coseismic rupture was followed by substantial deep afterslip (up to 0.4 m; see Figure 3.3b) that also expanded out of the coseismic area. It is still concentrated to a relatively small patch, making its signature in the postseismic data relatively weak. Removing this afterslip patch from the model results in only a minimal change of the misfit (1 to 2%). On the basis of this, we suggest that the appearance of this velocity-strengthening zone is constrained by the dynamics of the coseismic rupture, whereas its afterslip is rather a by-product.

The deep afterslip can be indirectly corroborated by the appearance of off-fault aftershocks [Hardebeck and Shelly, 2016] that appear below the coseismic rupture with notable concentration around the area (Figure 3.3b). Figure 3.9e shows the time development of the aftershock rate obtained by counting the aftershocks in the area outlined in Figure 3.9b. The temporal decay of aftershock rate follows Omori's law and is very similar to the evolution of stress rate obtained from the middle of the strengthening area, pointing to their possible driving by the deeper afterslip. While we use the aftershock rate to only confirm a stress trend in the strengthening zone, the addition of aftershock rate in the inversion directly as a measure of stress rate can be an additional piece of data to further constrain the postseismic model [Inbal et al., 2017].

4. Comparative analysis of results from dynamic source inversions with different friction laws

We presented two different friction laws in Chapter 2 – the rate-and-state with fast-velocity-weakening (FVW) and the linear slip-weakening (SW). Only the FVW friction was suitable for the dynamic inversion presented in Chapter 3, because one of the main goals was to model the long-term postseismic slip. The FVW friction law features the healing effect and can thus model the longer-term development of faults during which the fault friction can again strengthen and the fault heals.

The SW friction is a standard in the dynamic modeling community due to its relative simplicity (low amount of parameters, linear dependence of friction on slip). We are thus interested in how the dynamic inversion employing the SW friction compares with the FVW one. To that end, F. Gallovič performed a dynamic inversion of the same 2014 South Napa earthquake employing the SW friction with as similar set-up as possible. This puts us in a unique position to compare dynamic models employing either SW or FVW friction law to model data from the same earthquake.

In this chapter, we aim to present and compare the results of both SW and FVW dynamic inversions. In Section 4.1, we make introductory remarks on how slip-dependence of friction implicitly appears in the FVW friction. Section 4.2 presents the unpublished dynamic inversion using the SW friction law. Sections 4.3 and 4.4 contain the comparison of the results of both the SW and FVW inversions.

4.1 Slip-weakening in FVW friction law

Slip-dependence of friction in the seismic phase is corroborated by ample experimental evidence and can be also derived from theoretical models [Scholz, 2012]. While rate-and-state models of friction (such as the FVW friction law used in this work) do not include slip-dependence explicitly, but only implicitly as part of the state-dependent term and state evolution equation. We will demonstrate that for a simplified case for $\dot{s} = \text{const.}$ at seismic values (1-10 m/s). We also consider typical values of the remaining friction parameters: $a = 0.01$, $\dot{s}_0 = 10^{-6}$ m/s, $L = 0.5$ m. For these values, the formula for friction (Equation 3.1),

$$S = \sigma_n a \ \text{arcsinh}\Big[\frac{\dot{s}}{2\dot{s}_0}\exp\Big(\frac{\psi}{a}\Big)\Big], \tag{4.1}$$

can be simplified considering that the inner term of arcsinh is a large number and $\text{arcsinh}(x) \sim \log(2x)$ for $x >> 0$, leading to

$$S = \sigma_n\Big[a\log\Big(\frac{\dot{s}}{\dot{s}_0}\Big) + \psi\Big)\Big]. \tag{4.2}$$

The first (logarithmic) term is constant with respect to state variable ψ and the friction thus follows it linearly- State variable ψ develops according to the slip-law evolution law (Equation 3.2):

$$\frac{d\psi}{dt} = -\frac{\dot{s}}{L}[\psi - \psi_{SS}], \tag{4.3}$$

where $\psi_{SS}(\dot{s})$ from Equation 2.45 is constant with respect to ψ. From here we can write the equation for infinitesimal $d\psi$ and ds ('multiply' by dt):

$$d\psi = -\frac{ds}{L}\psi + \frac{ds}{L}\psi_{SS}. \tag{4.4}$$

The first term on the right-hand side is clearly slip-weakening, causing an exponential decrease of the state variable and thus friction with increasing slip. The second term is slip-strengthening and corresponds to the healing term dominating the equation when the steady-state value of the state variable ψ_{SS} is higher than ψ.

4.2 Dynamic inversion with SW friction law

We use the method of Gallovič et al. [2019a] to perform the SW dynamic inversion. We maintain as many features of the presented FVW problem as possible (see Chapter 3 for details), including the finite difference setup (discretization, domain size), fault geometry (size and orientation of the fault), velocity model, and the positions of both seismic and GPS stations. We exclude the postseismic data as SW friction cannot model the postseismic phase. We include zero coseismic displacements at the positions of the southern alignment fields NLAR and NWIT, where no coseismic rupture was observed.

Following Gallovič et al. [2019a], we parametrize the dynamic model by spatial distributions of three dynamic parameters: shear (horizontal) prestress T_0, breakdown friction drop $\Delta f = f_s - f_d$ and slip-weakening distance D_c, while the dynamic friction is set constant $f_d = 0.4$. See Figure 2.3 and the related commentary for more details about the SW friction law and its parameters. The dynamic parameters are sought on the fault in a coarse 12x9 grid of control points at the same positions as in the FVW inversion, and the values on the finer finite difference grid are acquired by bilinear interpolation. We note that the inversion constrains both prestress and breakdown friction drop only relative to the dynamic friction as dynamic models with prestress $T_0 - \sigma_n f_d$ and $\Delta f = f_s - f_d$ generate the same rupture propagation for different values of f_d, assuming $f_d >> 0$ [Kostka, 2022]. In addition, we include a constant cohesion $f_c = 0.5$ MPa over the whole fault.

The Bayesian dynamic inversion started from an independently prepared initial model and with wide homogeneous prior distributions of dynamic parameters, see Table 4.1. We note that slip-strengthening friction is not permitted with this choice of intervals. The Monte Carlo sampling method visited a large set of hundreds of thousends trial models, out of which $\sim$ 60000 were accepted by the Metropolis-Hastings algorithm, where the probability of acceptance of the model was proportional to the misfit between synthetic and real data (both seismograms and coseismic GPS). For this comparative analysis, we picked only models with

seismogram variance reduction (VR) > 0.43, which further restricted the model ensemble to $\sim$45000 models. All models in the restricted ensemble model fit the seismograms similarly, with VR = 0.43-0.47. The seismogram fit reached by the models with SW friction is very similar to the results of the inversion using the FVW friction presented in Chapter 3. We demonstrate this on best-model seismograms from both the SW and FVW inversions in Figure 4.1.

Dyn. Parameter	Min, Value	Max. Value
Prestress T_0	0 Pa	10^8 Pa
Breakdown friction Δf	0	1.0
Weakening distance D_c	0.1 m	2.0 m

Table 4.1: Minimum and maximum values of the prior homogenous distributions of the dynamic parameters considered in the SW inversion.

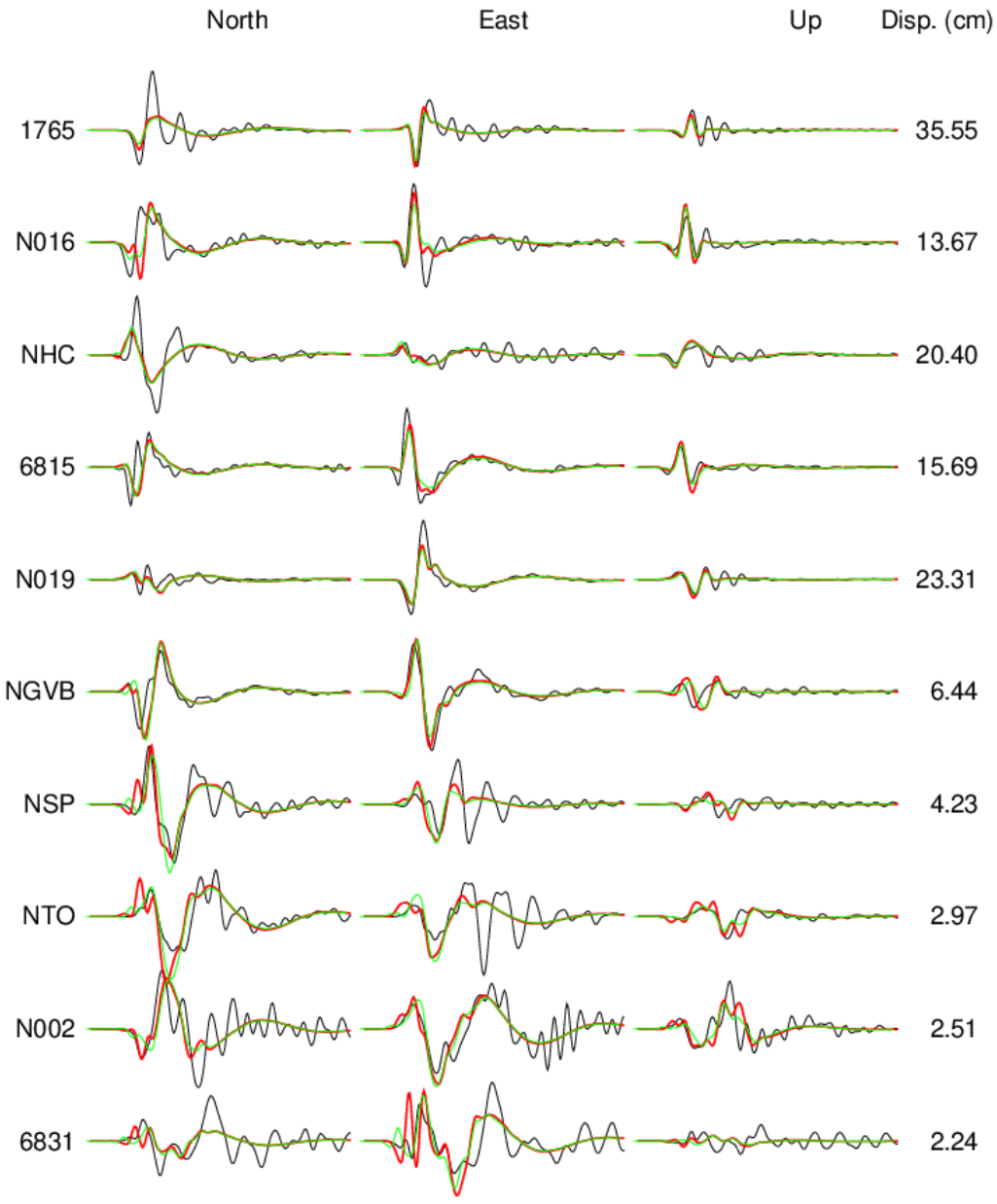

Figure 4.1: Best-model seismograms from inversions with the SW (green) and FVW (red) friction. The panels show three components (north, east, and up) of displacement on seismic stations, whose names are written on the left side. Real seismograms are denoted by black lines. Numbers on the right side show maximum amplitude of displacement in centimeters.

Spatial distributions of the ensemble averages of coseismic kinematic parame-

ters are presented in Figure 4.2. The earthquake nucleated at the depth of 8.5 km and propagated towards the surface and north (opposite to strike). Two patches of concentrated slip and stress drop are clearly visible in Figure 4.2 with maxima at 6 km and 3 km depths. Rise time decreases with depth from ∼5 s at 7.5 km depth to ∼1 s near the surface. We note that this image roughly agrees with the results of the FVW inversion (see Figures 3.3 and 3.4). The main difference is in the rise times, that are significantly higher in the SW case.

Figure 4.3 shows the spatial distribution of ensemble averages (left column) and relative standard deviations (SDs, right column) of the three dynamic parameters - prestress T_0, breakdown stress drop Δf and slip-weakening distance D_c. Patches of maximum slip and stress drop from Figure 4.2 overlay here with patches of high T_0, low Δf, and low D_c, while the edges of the rupture are characterized by lower T_0, and higher Δf and D_c. The relative SD of the dynamic parameters is systematically lower in places with higher slip.

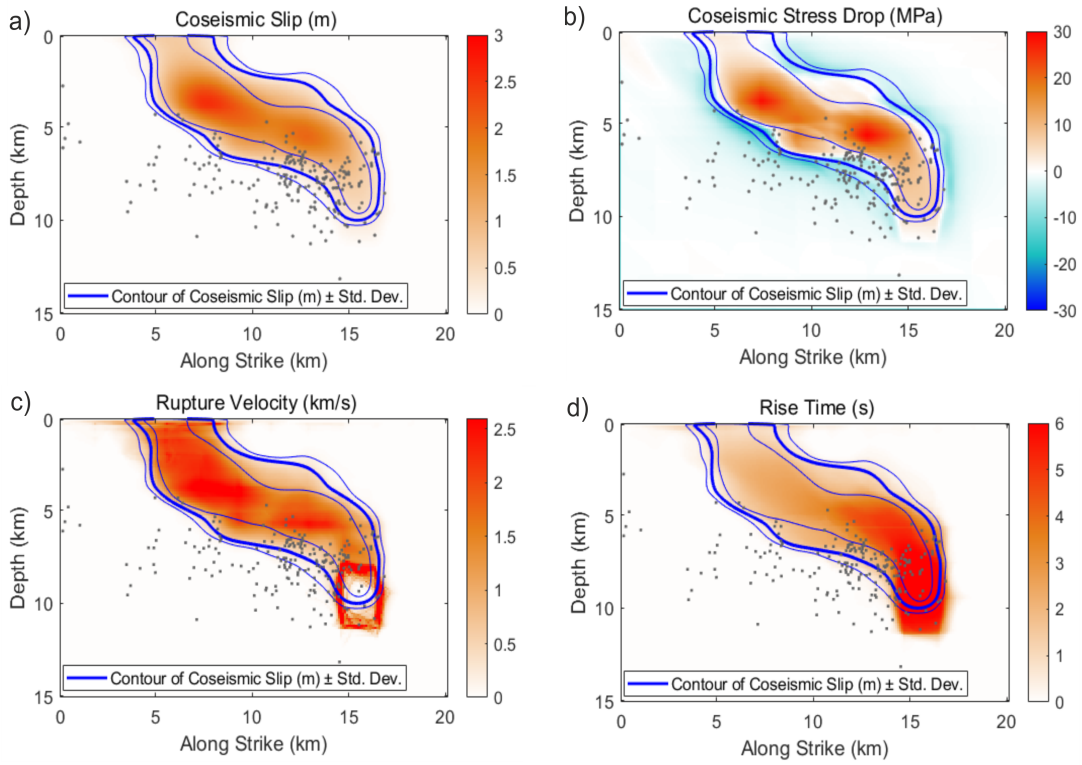

Figure 4.2: Spatial distribution of selected kinematic parameters from the SW inversion. Panels show ensemble averages of (a) slip, (b) stress drop, (c) rupture velocity, and (d) rise time. Gray dots represent aftershocks (NCEDC) with fault-perpendicular distance <5 km. Blue lines indicate contours of coseismic slip (bold line) and its SD as thin lines.

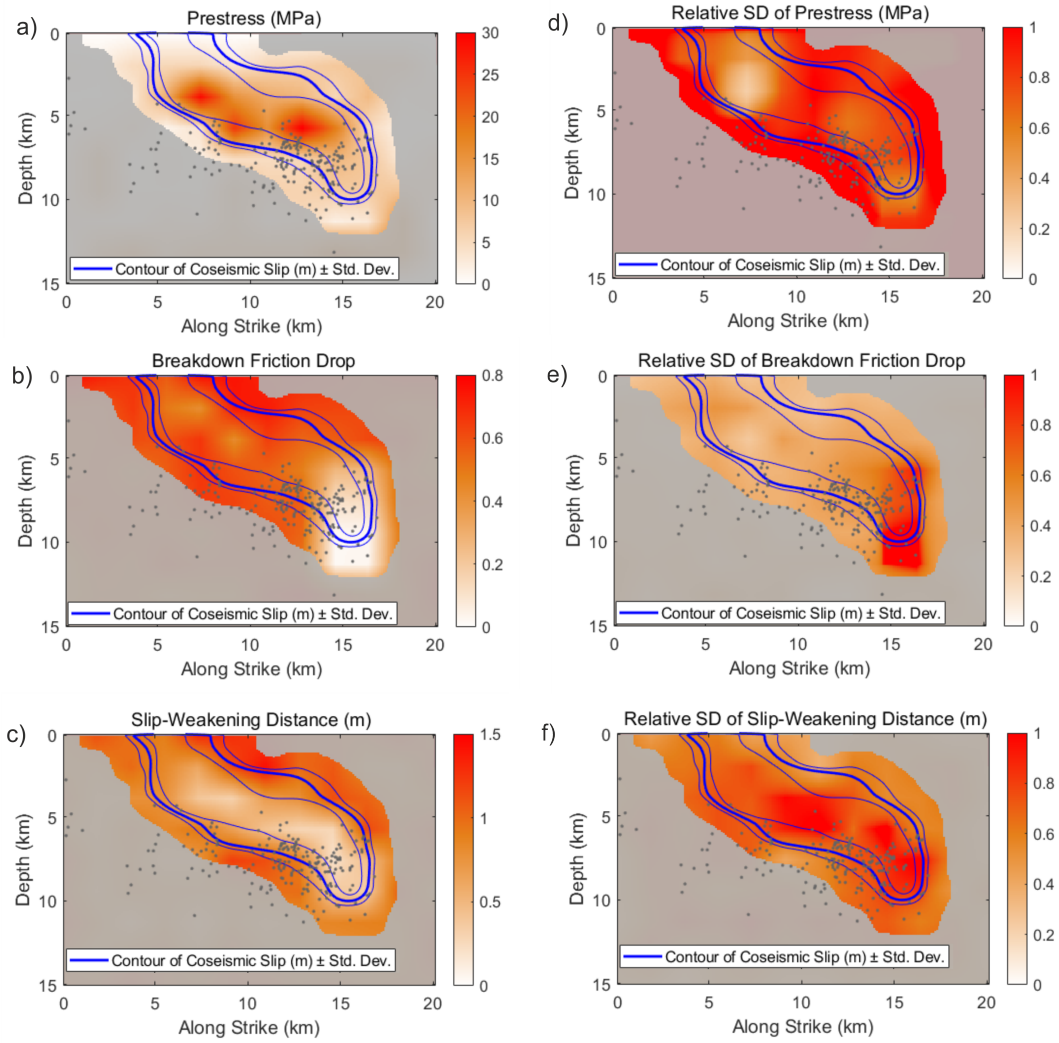

Figure 4.3: Spatial distribution of the dynamic parameters and their statistical properties. Panels in the left column (a-c) contain ensemble averages of prestress, breakdown friction drop, and slip-weakening distance. The right column panels (d-f) contain the relative SD of the respective quantities. Gray dots represent aftershocks (NCEDC) with fault-perpendicular distance <5 km. Blue lines indicate contours of the coseismic slip as in Figure 4.2.

4.3 Comparison of SW an FVW model ensembles

As we have already shown in Section 3.2, the models from both the SW and FVW inversions model the seismograms with comparable accuracy. We are now interested in what are the differences between the SW and the FVW model ensembles in terms of gross physical parameters (e.g., mean slip or seismic moment) and properties of the earthquake rupture they create (e.g., spatial distribution of stress drop, local development of slip rate). For consistency, we also imposed the condition of minimum seismogram VR (0.43) on the FVW ensemble.

We use the following definitions of gross physical parameters. We compute

slip-weighted spatial averages of slip and stress drop [Noda et al., 2013]. Ruptured area A_r is the fault area that achieved more than 5% of maximum slip in the given model. We define the centroid depth as the mean location of the seismic moment density:

$$h_c = \frac{\int_S [s(x,y)\mu(y)y]\mathrm{d}x\mathrm{d}y}{\int_S [s(x,y)\mu(y)]\mathrm{d}x\mathrm{d}y}, \tag{4.5}$$

where S denotes the fault area, and x and y denote the horizontal and vertical position on the fault, respectively.

We calculate [Ripperger et al., 2007] radiated energy E_r as:

$$E_r = \frac{1}{S}\Big[-\frac{1}{2}\int_S s_i(t)\Big(T_i^f - T_i^0\Big)dS - \int_0^{t^f} dt \int_S \dot{s}_i(t)\Big(T_i(t) - T_i^0\Big)dS\Big], \tag{4.6}$$

fracture energy E_g as:

$$E_g = \frac{1}{S}\Big[\int_S dS \int_0^{s^f} \Big(T_i(s) - T_i(s^f)\Big)ds_i\Big], \tag{4.7}$$

and radiation efficiency as the fraction of E_r and the sum of both energies:

$$\eta_{rad} = \frac{E_r}{E_r + E_g}. \tag{4.8}$$

Time-dependent traction, slip, and slip rate are denoted as $T_i(t)$, $s_i(t)$, and $\dot{s}_i(t)$, respectively. Symbol T_i^0 denotes initial stress, and t^f, s^f, and T_i^f denote final coseismic values of time, slip, and traction, respectively. Einstein summation applies in the following equations, where two same indices occur in the same term.

We show histograms of the gross physical parameters of both the SW and FVW model ensembles in Figure 4.4. Ensemble averages and SDs of the gross physical parameters can be found in Table 4.2.

The distribution of VR suggests that a lot of SW models has the seismogram VR closer to the lower boundary of VR = 0.43, in contrast with the FVW ensemble whose VR shows a bimodal distribution with maxima around 0.45 and 0.47. This difference between both ensembles might be a result of how the posterior sampling procedure performed with the different friction laws, because the FVW inversion has larger amount of free parameters and dataset enriched by postseismic data in comparison with the SW inversion.

Distributions in Figure 4.4 are usually unimodal, but in the SW case the stress drop, centroid depth and fracture energy show a bimodal distribution. Gross physical parameters from the FVW model ensemble are consistently larger than the SW ones, with the exception of the rupture area, which achieves very similar value for both ensembles. Relative uncertainties are larger in the case of the SW ensemble with no exceptions.

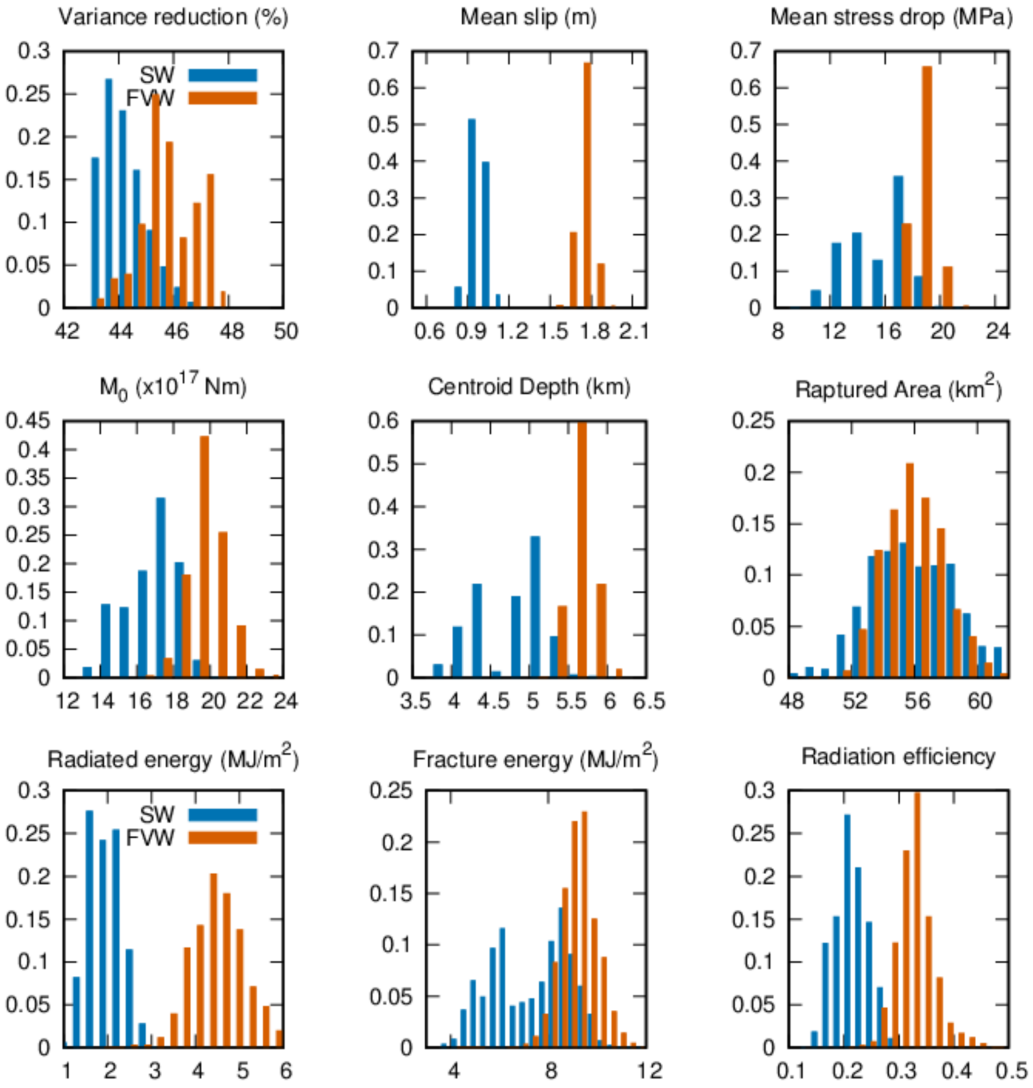

Figure 4.4: Histograms of gross physical parameters, see text for their definitions. Distributions from the SW and FVW inversion are shown as blue and red bars, respectively.

Law	SW	FVW
$\bar{s}$ (m)	0.99 ± 0.06	1.74 ± 0.05
$\Delta\bar{\sigma}$ (MPa)	15.5 ± 2.1	18.5 ± 0.7
M_0 (10^{18}Nm)	1.69 ± 0.14	1.98 ± 0.10
h_c (km)	4.78 ± 0.43	5.65 ± 0.16
A_r (km^2)	56.3 ± 3.1	55.9 ± 0.2
E_r (MJ/m^2)	1.98 ± 0.35	4.5 ± 0.7
E_g (MJ/m^2)	7.3 ± 1.3	9.12 ± 0.8
η_{rad}	0.214± 0.084	0.33 ± 0.08

Table 4.2: Ensemble averages and uncertainties of gross physical parameters for the model ensembles inferred withthe SW and FVW inversions.

The spatial distributions of both kinematic and dynamic parameters from the SW (Figures 4.2 and 4.3) and FVW (Figures 3.3 and 3.8) inversions share many similarities. Namely we see a very similar spatial structure of both slip and stress drop with two distinct patches at 6 km and 3.5 km depths and small surface rupture in the southern (left) portion of the fault. This suggests the available data resolve this basic picture independently of the chosen friction law.

To study the differences between both ensembles in more detail, we compare the contours of coseismic slip from the SW ensemble with both coseismic and postseismic slip from the FVW ensemble in Figure 4.5. While the slip contours mostly overlap, there are discrepancies in the vertical positioning of the slip. The SW models occupy shallower depths than the FVW ones, especially in the southern half of the fault. This also manifests in Table 4.2 as the difference between the SW and FVW average centroid depth h_c, where the SW model's centroid is positioned 900 m closer to the surface and with larger uncertainty than the FVW centroid.

SW slip is less constrained, which is clearly visible when comparing the distance between the SD contour lines and the line denoting the average slip in Figure 4.5, and the relatively large SD of centroid depth in Table 4.2. As the size of the ruptured area is well constrained in both friction models, the higher uncertainty of the shallower border of the SW rupture leads to a similar uncertainty of the deeper border.

We suppose that the difference in the position of the coseismic slip is due to the absence of afterslip modeling in the SW inversion. As seismic and aseismic slip are mostly spatially separated [Marone et al., 1991], the area of shallow afterslip effectively blocks the spread of significant coseismic slip in the FVW inversion, see Figure 4.5. The only comparable constraint on the SW inversion is the zero coseismic slip in the NLAR and NWIT alignment fields, which only prevents very shallow slip at their positions.

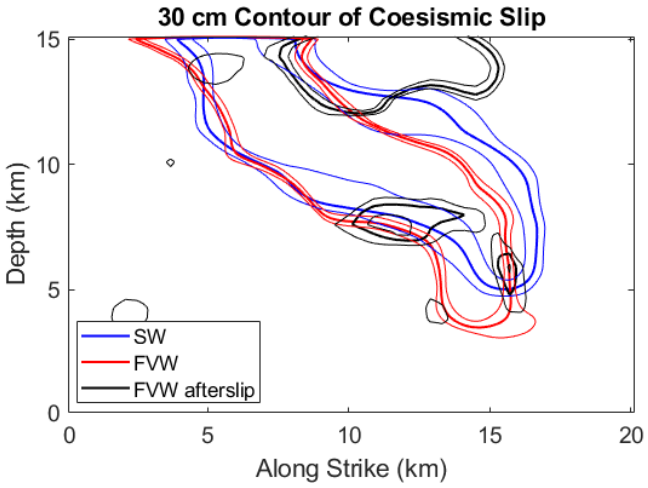

Figure 4.5: Contours of 30 cm slip of the coseismic SW and FVW slip and the FVW afterslip, see legend. Thick lines delineate ensemble averages and thin lines represent their SD.

Next, we investigate the impact of the depth of the slip (quantified as the centroid depth) on seismic moment and stress drop. We plot the values of stress drop and seismic moment from both ensembles as a scatter plot against centroid depth in Figure 4.6. It demonstrates a clear trade-off between the centroid depth and both seismic moment and stress drop, which are both higher for deeper models. While the trade-off occurs in both inversions, it is more pronounced in the SW one, see the slope of the linear regression lines in Figure 4.6. The SW seismic moment and stress drop ranges from 1.4 $\times 10^{18}$ to 2.1 $\times 10^{18}$ Nm and from 10 to 20 MPa, respectively. The intervals in the FVW ensemble are smaller, with the seismic moment from 1.7 $\times 10^{18}$ and 2.25 $\times 10^{18}$ Nm and stress drop from 17 to 21 MPa.

The physical mechanism behind the trade-offs of the seismic moment and stress drop with depth is the attenuation of seismic waves due to geometric spreading. To fit the seismogram amplitude with similar accuracy, the deeper earthquake needs to be larger in terms of seismic moment and stress drop. This mechanism is significant in the case of local stations used in the inversion as the difference in depth between earthquakes significantly changes the wave travel-distance (often more then 10%). The FVW model ensemble centroid depth is much better constrained, leading to a weaker trade-off between seismic moment and h_c and overall lower SDs. This result underscores the importance of afterslip modeling as it may improve the resolution of coseismic slip.

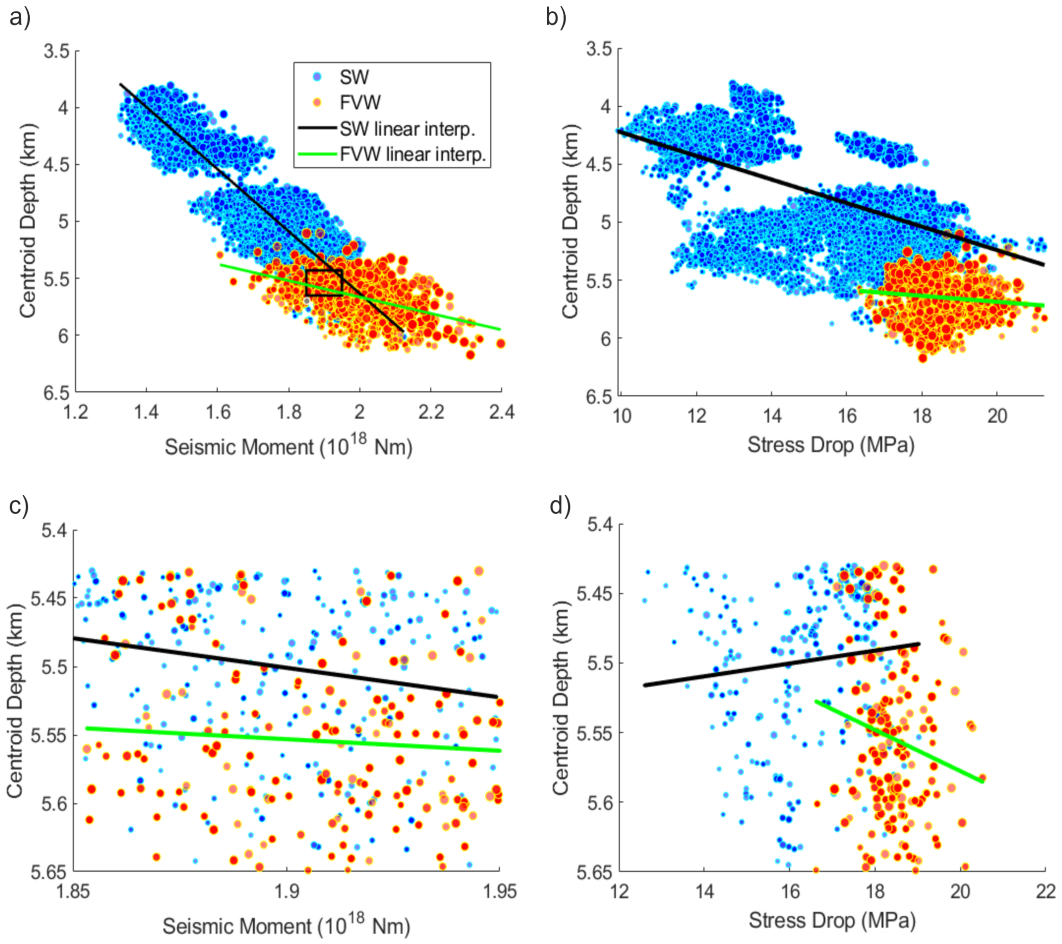

Figure 4.6: Ensemble scatter plot of (a) coseismic moment and (b) stress drop versus centroid depth. SW and FVW models are denoted by blue and red dots, respectively, with diameter proportional to the model variance reduction. The black rectangle in (a) denotes a selection of models, whose scatter plots are shown in panels (c) and (d), respectively. Lines shown linear regressions of the respective ensembles, see legend in panel a.

The fact that the SW models are less spatially constrained poses a challenge to further detailed comparison. It manifests as high uncertainty of both gross parameters and the spatial distributions of kinematic and dynamic parameters. The SW models with shallow centroid depth have coseismic slip at portions of the fault that ruptured aseismically in the FVW inversion. As we already presented ample evidence for the occurrence of near-surface aseismic slip in Chapter 3, we consider the SW models coseismically rupturing the shallow aseismic part to contradict the observations. We notice in Figure 4.6, that there is a large amount of SW models with the centroid depth of around 5.5 km, overlaying with FVW models even in terms of the seismic moment (though still with slightly different stress drop). We will next focus on this group of deeper-positioned SW models.

4.4 Detailed comparative analysis of models with similar centroid depth

To facilitate a more detailed comparison, we select models with centroid depth below 5.3 km, which we identified as a representative cut-off, enveloping the majority of the FVW models. Models fulfilling this condition create subset ensembles with sizes of 3221 (SW) and 6682 (FVW) models.

We compare the slip contours of the full and subset ensembles in Figure 4.7. It shows that the model subsets are much better spatially aligned, specifically the SW subset does not occur on the shallow postseismically slipping part of the fault.

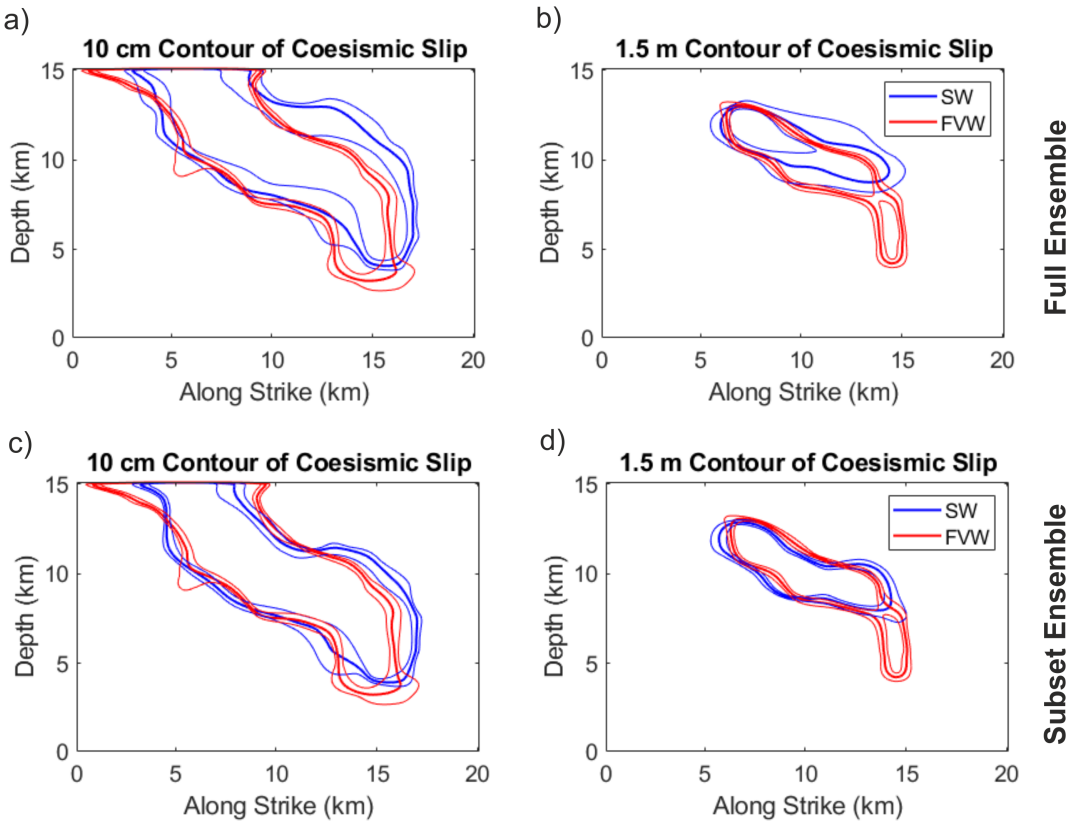

Figure 4.7: Contours of coseismic slip from the SW (red) and FVW (blue) inversions. Panels (a, b) show results for the whole ensemble and panels (c, d) for the subset ensemble with centroid depth constrained to >5.3 km. The left and right panels show contours at 10 cm and 1.5 m, respectively. Thick and thin lines represent the ensemble average and SD, respectively.

We show histograms of gross physical parameters of the subset ensembles in Figure 4.8 and the ensemble averages and uncertainties in Table 4.3. As we specifically chose the cut-off depth to accept the majority of the FVW models in the subset ensemble, the distributions of FVW gross parameters remained practically the same. On the contrary, the SW subset is less than 10% of the full SW ensemble, populated with models with $h_c = (5.6 \pm 0.4)$ km. This constraint

has a significant impact on other physical parameters. Specifically, the ensemble average of the seismic moment grew by 10%, while its SD dropped by 65%, and mean stress drop grew by 5% and its SD dropped by 10 %. Energy, both fracture and radiated, is also higher, though only by 2-3%. The distributions in Figure 4.8 are mostly unimodal, except for fracture energy. Models with higher fracture energy ($\sim$8MJ/m^2) are represented in the subset ensemble more with respect to the full ensemble distribution from Figure 4.4, where the lower and higher E_g models were represented equally.

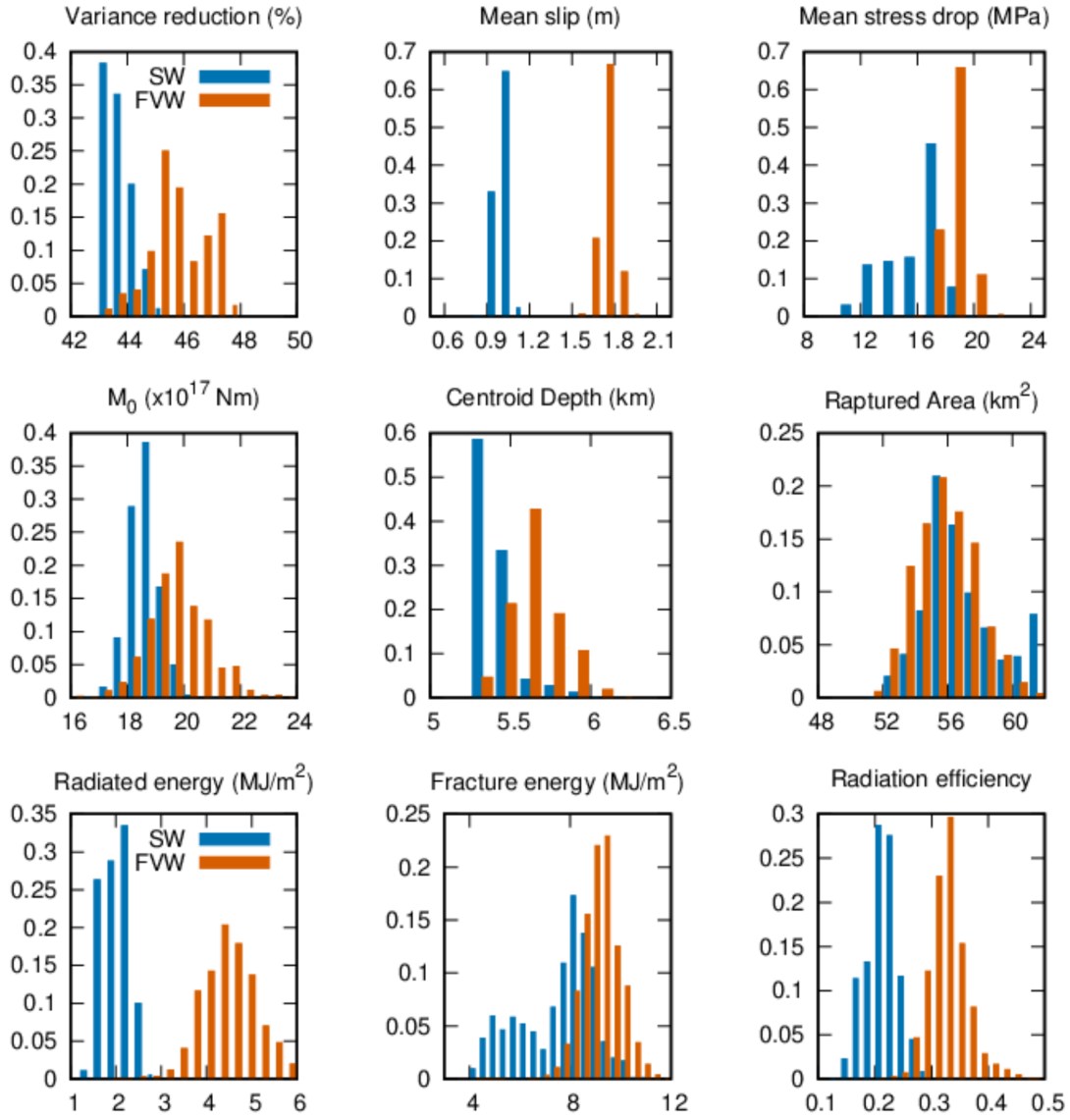

Figure 4.8: Histograms of gross physical parameters for the subset ensembles with centroid depth constrained to >5.3 km. SW and FVW inversion results are shown as blue and red bars, respectively.

Law	SW full	FVW full	SW subset	FVW subset
$\bar{s}$ (m)	0.99 ± 0.06	1.74 ± 0.05	1.01 ± 0.05	1.74 ± 0.05
$\Delta\bar{\sigma}$ (MPa)	15.5 ± 2.1	18.5 ± 0.7	15.9 ± 1.9	18.5 ± 0.7
M_0 (10^{18}Nm)	1.69 ± 0.14	1.98 ± 0.10	1.86 ± 0.05	1.98 ± 0.1
h_c (km)	4.78 ± 0.43	5.65 ± 0.16	5.60 ± 0.39	5.65 ± 0.16
A_r (km^2)	56.3 ± 3.1	55.9 ± 0.2	58.0 ± 3.2	55.8 ± 1.9
E_r (MJ/m^2)	1.98 ± 0.35	4.5 ± 0.7	2.02 ± 0.29	4.50 ± 0.72
E_g (MJ/m^2)	7.3 ± 1.3	9.12 ± 0.8	7.52 ± 1.46	9.19 ± 0.80
η_{rad}	0.214± 0.084	0.33 ± 0.08	0.212± 0.07	0.33 ± 0.09

Table 4.3: Ensemble averages and uncertainties of gross physical parameters for model ensembles with SW and FVW friction for both the full ensemble and the subset ensemble with centroid depth constrained to >5.3 km.

We also point out an interesting phenomenon – the SW subset seismic moment is higher than the full ensemble one, while the mean slip and ruptured area remain quite similar. The subset models occur at lower depths with higher S-wave velocity and therefore higher shear modulus μ. Figure 4.9 shows the depth profile of μ calculated from the adjusted GIL7 model used for the simulations. The model has a step increase in μ at 5 km depth. While the average centroid depth $h_c = (4.78 \pm 0.43)$ km of the full ensemble is positioned in the medium with lower μ, the deeper models from the subset ensemble are positioned below the step, with 30% higher μ. The seismic moment of the deeper-positioned models is thus higher even without any change in slip or ruptured area, as it is proportional to slip-averaged μ. A similar effect might be the driving effect of higher stress drop for the subset (deeper) models.

While our conclusions from the last section still hold and the SW models generally show lower values of slip, stress drop, fracture and radiated energy, and energy efficiency than the FVW models, the differences between the subset ensembles are significantly smaller than for the full ensembles. Especially in the case of the seismic moment, the difference between the SW and FVW ensemble averages is well within their uncertainties. Opposite to that, the differences in energies and energy efficiency hold the same for both the full and subset ensemble, suggesting that this difference is dictated by the choice of the friction law.

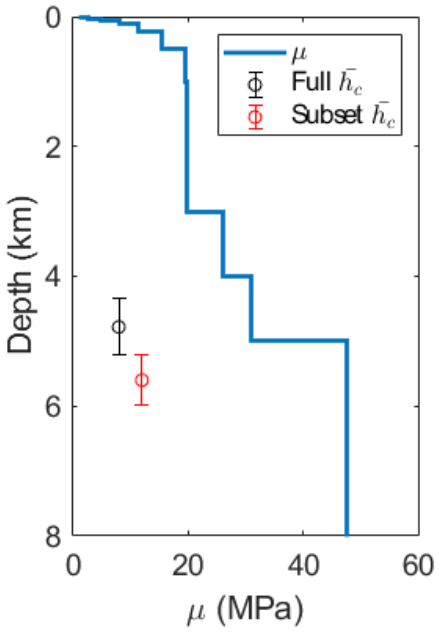

Figure 4.9: Depth profile of the shear modulus μ from the adjusted GIL7 velocity model used in the modeling. Positions of the SW full and subset ensemble centroid depths with their uncertainty are shown as black and red error bars, respectively.

We now compare the spatial distributions of the subset ensemble averages of kinematic quantities (slip, stress drop, rise time, and rupture velocity) from the SW and FVW inversions in Figure 4.10. Both subsets have a very similar distribution of slip and stress drop if we neglect the nucleation-induced higher deep stress drop in the FVW case, as this is most probably given by the difference between the nucleation procedures. There is a difference in the structure of the major slip and stress drop patch at 6 km depth, which are both continuous in the FVW case but divided into two parts in the SW models.

While the mean rupture velocity is very similar in both SW and FVW cases, there are differences in their spatial structure. The rupture velocity in the SW case is more heterogeneous at the 6 km depth with two small patches of almost supershear rupture velocity ($\sim$3.7 km/s) at places with maximum stress drop. The most striking difference between the SW and FVW models is in the spatial distribution of rise time, which is defined as the time interval between the times when the slip rate crosses the threshold of 1 cm/s. The FVW inversion has the rise time of 1-1.5 s over the whole fault with an increase towards 1.5 s at shallow depths. The SW inversion has the rise time comparatively high ($\sim$4.5 s) at greater depths and decreases to $\sim$1 s near the surface.

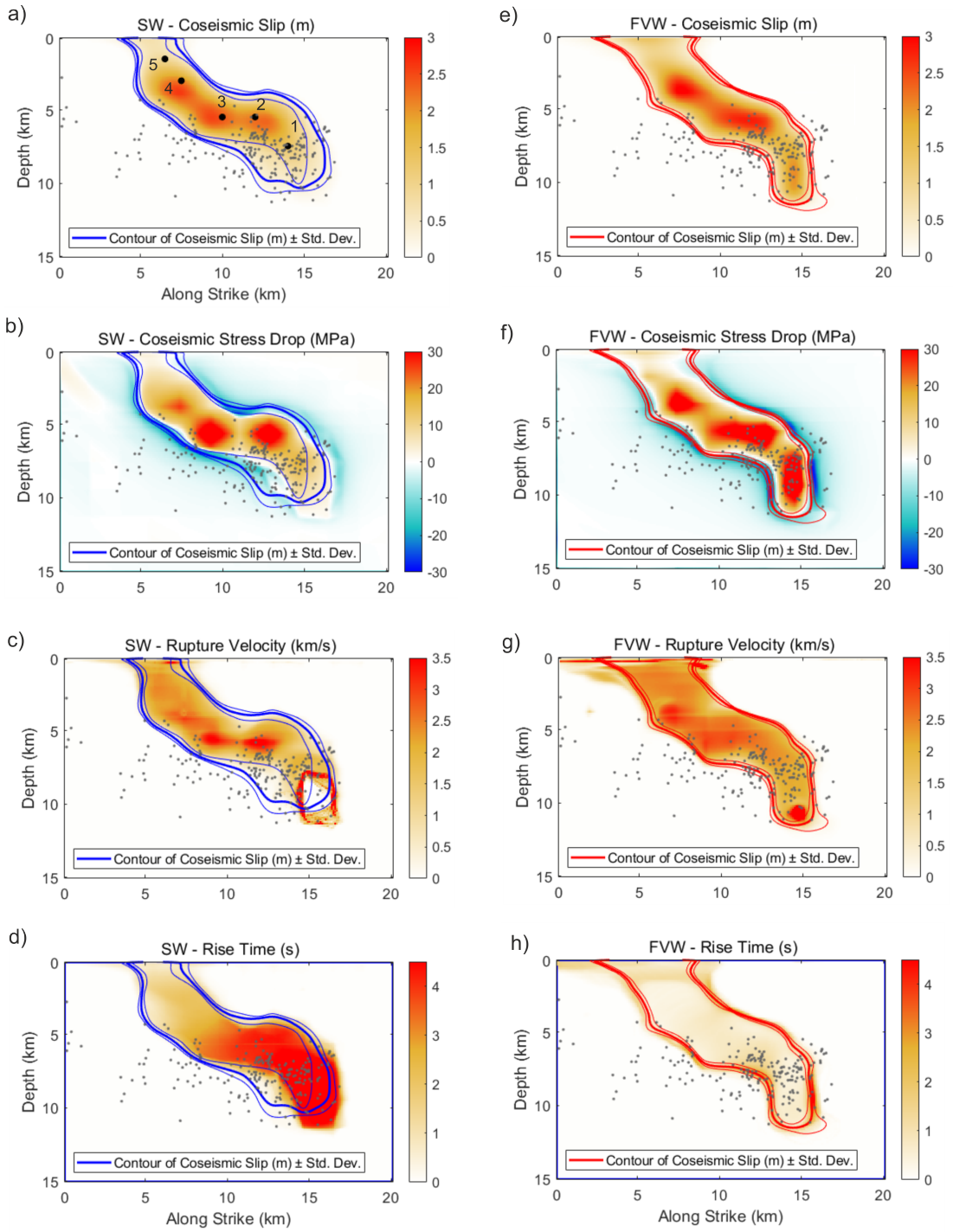

Figure 4.10: Spatial distributions of selected kinematic parameters and their statistical properties for the subset ensembles with centroid depth constrained to >5.3 km. The left column (a-d) shows the SW inversion ensemble averages of slip, stress drop, rupture velocity, and rise time, while the right column (e-h) shows the same for the FVW inversion. Gray dots represent aftershocks (NCEDC) with fault-perpendicular distance <5 km. Black dots with numbers in (a) denote positions for the point comparisons in Figure 4.11. Blue and red lines indicate the contours of SW and FVW slip and their uncertainties, respectively.

Figure 4.11 compares the evolution of horizontal slip rate and shear stress with time and shear stress with slip for a chosen SW and FVW model. We choose two

similar models with $h_c = 5.6$ km and $M_0 = 1.9 \times 10^{18}$ Nm. On-fault positions of the five points we chose are denoted in Figure 4.10. To remove the arbitrary effect of the choice of the dynamic, or weakened friction coefficient, we adjusted values of stress in the central and right columns by subtracting its minimum value. The general properties of the rupture are quite similar for both SW and FVW models. The rupture is pulse-like (the duration of the slip rate is significantly lower than the duration of the earthquake), with comparable mean rupture speeds. At greater depths, the SW slip rate duration is longer and with more complicated temporal evolution showing two distinct peaks. This occurrence starts near the first high-stress drop patch, where the rupture accelerates to a very high (close to super shear) speed. Significant differences occur when looking at the maximum values of slip rate and shear stress, with maxima twice larger in the FVW case than for the SW model.

The maximum slip rates >10 m/s in the FVW models are not considered typical for natural earthquakes. Nevertheless, its duration is over a very short interval of time and space and has thus minimum impact on seismograms. Moreover, in reality, it would be likely diminished by the onset of plasticity, which is not included in our model.

Healing in the FVW case can be observed at several places on the fault (namely points 1 and 4), where the stress increases with continuing slip. The graphs of the temporal evolution of stress show that the majority of the healing occurs right at the end of the slip rate pulse, which is driven by the choice of the slip-law evolution equation.

Additionally, near-surface point 5 shows a case, where the SW model slip is lower than local D_c, which is considered atypical in dynamic modeling. In our experience this is a common occurrence only in the near-surface layer, where the rupture needs to decelerate to not cause a major breakage of the free surface and with large slip [e.g., Gallovič et al., 2019b, Tinti et al., 2021].

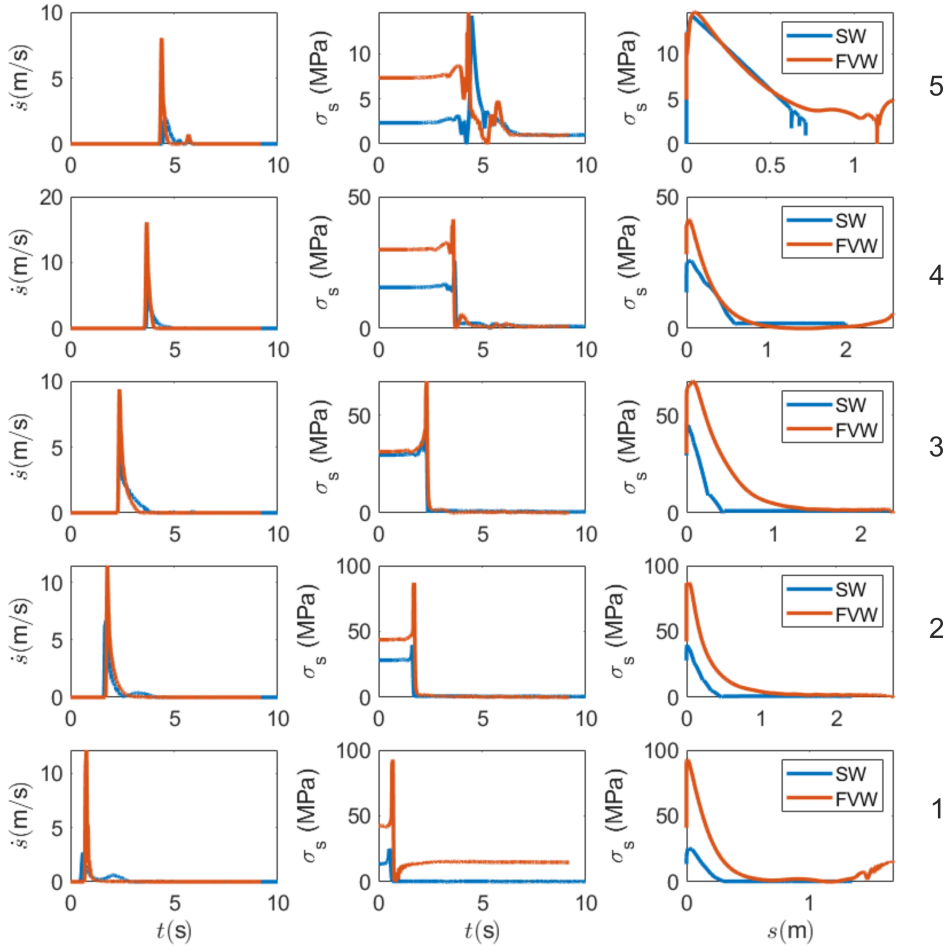

Figure 4.11: Evolution of slip rate and shear stress with time (left and central panel columns, respectively) and shear stress with slip (right column) at five chosen points on the fault (numbered dots in Figure 4.10 for their positions). In the central and right columns, zero corresponds to the respective minimum shear stress. Numbers on the right side of panels denote the point.

We show the spatial distributions of mean dynamic parameters in Figure 4.12 for the subset ensemble of the SW models. We see several differences when comparing with the full SW ensemble results (Figure 4.3). There are clear features such as the division of the heightened prestress at 6 km depth into two patches. The relative SD of all three dynamic parameters drops significantly in the rupture area. We suppose that these differences are due to the more constrained position of the earthquake rupture depth in the case of the subset ensemble.

The slip-weakening distance D_c and the characteristic slip L are interesting dynamic parameters to compare, as models with classical RS friction were reported to have L approximately 15 times smaller than slip-weakening equivalent distance D_{eq}^0 [Cocco and Bizzarri, 2002]. Our simulations show instead similar values of L and D_c (see Figure 4.13) with L being higher by one order of magnitude than expected. We consider this to be due to the inclusion of the fast-velocity-weakening effect that effectively lowers the D_{eq}^0, and thus allows larger L while

keeping D^0_{eq} the same. We also note that the spatial distribution of D_c seems much more heterogenous than the distribution of L.

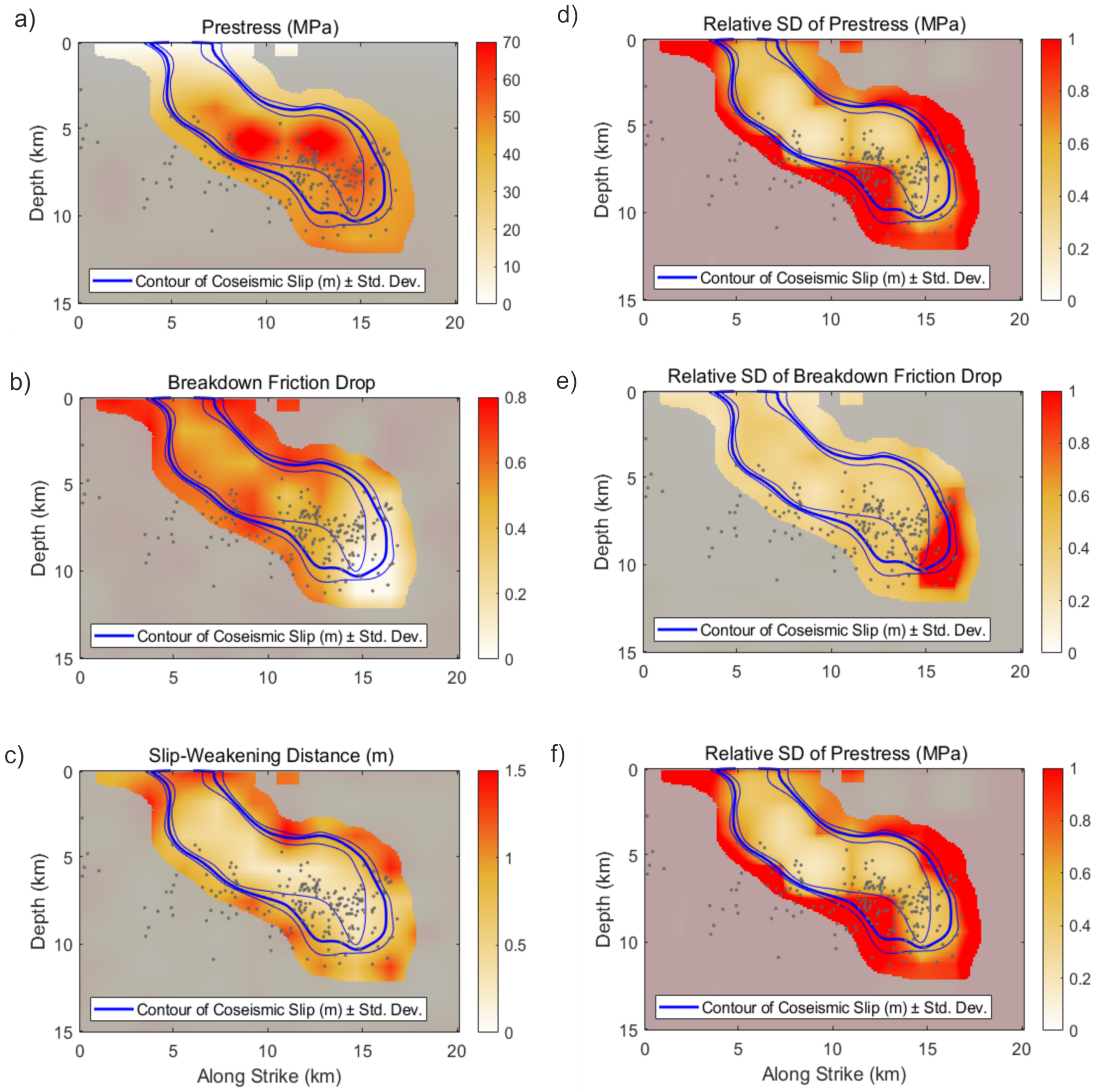

Figure 4.12: Spatial distributions of selected dynamic parameters and their statistical properties for the SW subset ensemble with centroid depth constrained to >5.3 km. The left column (a-c) panels show the ensemble averages of prestress, breakdown friction drop, and slip-weakening distance, while the right column (d-f) shows the relative SD of the same quantities. Gray dots represent aftershocks (NCEDC) with fault-perpendicular distance <5 km. Blue lines indicate the contours of SW subset slip and its uncertainties.

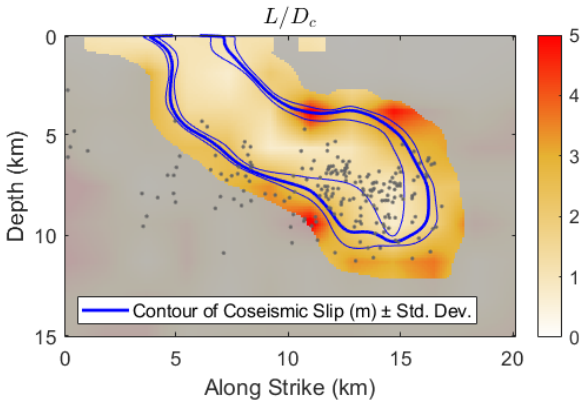

Figure 4.13: Spatial distribution of the ratio between the subset ensemble average of L and D_c being close to 1 within the rupture. Gray dots represent aftershocks (NCEDC) with fault-perpendicular distance <5 km. Blue lines indicate the contours of SW subset slip and its uncertainties.

5. Conclusions

This Thesis contributes to the development of inverse physics-based modeling of the earthquake source. Our study of the 2014 Napa earthquake in Chapter 3 reconciles and refines previous disjunct kinematic analyses of its coseismic and postseismic slip. We show how the stressing and frictional conditions on the fault govern the spatial separation between the shallow co- and postseismic slip. We determine that the earthquake created a rather narrow oblique rupture with postseismic slip spreading southwards, especially in the shallow area. This faulting complexity is driven by frictional rheology, supporting the hypothesis about the significant impact of heterogeneous lithology on rupture propagation [Floyd et al., 2016]. A particular, otherwise unrevealable feature, is that the coseismic rupture partially propagated through deep and shallow areas with velocity-strengthening frictional rheology (usually not supporting earthquake propagation), where postseismic afterslip occurred subsequently. We demonstrate that the deep afterslip was accompanied by off-fault aftershocks. We point out that since the co- and postseismic slip are only partially overlapping on the fault, the joint modeling allows us to constrain dynamic parameters on a larger portion of the fault than with coseismic data only.

Comparisons of the dynamic inversions with fast-velocity-weakening and slip-weakening friction laws in Chapter 4 lead to interesting conclusions. We see many similarities between the models, especially in the spatial distribution of slip and stress drop, or pulse-like evolution of the slip rate. In this sense, the results of the dynamic inversion seem to be better constrained than various kinematic inversions. Finding common properties of dynamic models across various friction laws is encouraging as the true friction law governing the tectonic faults remains elusive. We note that the elastodynamic equation is the common factor between both dynamic inversions, and can play a key role in constraining the source properties. The obvious advantage of the rate-and-state framework is the ability to model the aseismic slip unfolding after the earthquake. We show that this capability might be relevant even when estimating coseismic quantities (such as the distribution of slip, or the value of seismic moment), due to the tendency of seismic and aseismic slip to occur on the fault with limited overlap. The location of the aseismic slip can thus act as an additional constraint on the coseismic slip and other physical parameters of the earthquake.

The mathematical complexity and nonlinearity of the dynamic inversion make it a technically demanding task, which we identify as a critical reason why it is presently understudied. The requirements are not only in high computational demands but also in both the quantity and quality of data used in the inversion. The physics-based inverse modeling presented in this Thesis is enabled by the current technology both on the modeling and data-collection ends. We took advantage of modern hardware and developed highly-efficient GPU-optimized code FD3D_TSN [Premus et al., 2020]. Both FD3D_TSN and the whole Bayesian inversion package fd3d_pt_tsn are freely available at `https://github.com/JanPremus/fd3d_TSN` and `https://github.com/fgallovic/fd3d_tsn_pt`, respectively. Speed-up of the computation time of the forward modeling by a factor of 10 decreased the total time of our inversion from years to a more manageable 2-3 months on

common hardware. Additionally, the wealth of scientific recordings of the 2014 Napa earthquake is unique and almost unprecedented elsewhere in the world. We especially underscore the importance of the postseismic surface displacement measurements that acted as the major constraint on the shallow afterslip. The only earthquake of similar size with an equal or even better data set is the 2004 Parkfield earthquake also in California.

Limitations of our current approach mostly stem from the trade-off between the model complexity and its computational demands. The current version of the code can model only vertical and planar faults because it allowed us to use a very efficient finite difference method. Further expansion of the code towards modeling of, e.g., dipping faults would significantly expand the group of events we could study. Finite difference methods with curvilinear grids are a typical way of introducing non-planar faults, but they come with a high computational burden. To our knowledge, only Cruz-Atienza et al. [2007] introduced a stable non-planar fault into the regular, partially staggered grid code. An intriguing alternative to achieve the desired geometry of the problem is to dip the free surface instead of the fault, using a vacuum formulation for the free surface, e.g., from Graves [1996]. This idea was recently tested by Pitarka [2020] with promising results. We note, that the introduction of the dipping fault through this method would increase the computational burden of the forward model by a factor of 2-3 because it would be required to simulate the whole domain instead of the current half and the domain would have to be larger to encompass the whole fault and free surface.

The computational burden when introducing other model complexities would be even higher, which currently impedes the progress of physics-based inversions. A possible remedy might be improving the inversion method to decrease the number of visited forward models. Concerning the Bayesian formulation, we see an untapped potential in the prior distributions of dynamic parameters that are currently set in all control points as the same wide homogenous distributions. Potential improvements to these prior distributions include carefully assimilating information from preceding kinematic inversions and previous general knowledge of rupture dynamics. Machine learning might provide a great tool for the assimilation, e.g., to filter out models that would lead to clearly too small or too large ruptures.

Any effort to decrease the computational requirements of the physics-based source inversions may promote their further spread. Dynamic inversions then have the potential to substitute the kinematic inversions and become a routine tool for studies of larger earthquakes. Although the recent dynamic inversions were only performed with the relatively simple dynamic source model, the Bayesian methodology is suitable for incorporating more advanced physics-based models, encompassing a wider range of fault phenomena than coseismic slip. In the future, more physically-complex models in combination with the available decades of GPS measurements and thousands of years of information about historical earthquakes could then lead to inverse modeling of the long-term seismic cycle models and pave the way to understanding the full spatially-temporal scale of the fault processes.

Bibliography

K. Aki and P. G. Richards. *Quantitative Seismology*. University Science Books, Sausalito, California, 2002.

J. P. Ampuero and Y. Ben-Zion. Cracks, pulses and macroscopic asymmetry of dynamic rupture on a bimaterial interface with velocity weakening friction. *Geophys. J. Int.*, 173(2):674–692, 2008.

R. Ando and Y. Kaneko. Dynamic rupture simulation reproduces spontaneous multifault rupture and arrest during the 2016 M w 7.9 Kaikoura earthquake. *Geophys. Res. Lett.*, 45:12875–12883, 2018.

D. J. Andrews. Rupture velocity of plane strain shear cracks. *J. Geophys. Res.*, 81(32):5679– 5687, 1976.

K. Bai and J.-P. Ampuero. Effect of seismogenic depth and background stress on physical limits of earthquake rupture across fault step overs. *J. Geophys. Res.: Solid Earth*, 122:10280–10298, 2017.

M. Barall. A grid-doubling finite-element technique for calculating dynamic three-dimensional spontaneous rupture on an earthquake fault. *Geophys. J. Int.*, 178 (2):845–859, 2006.

M. Barall and R. A. Harris. Metrics for comparing dynamic earthquake rupture simulations. *Seismol. Res. Lett.*, 86(1):223–235, 2015.

S. Barbot, N. Lapusta, and J.-P. Avouac. Under the hood of the earthquake machine: Toward predictive modeling of the seismic cycle. *Science*, 336:707–710, 2012.

W. Barnhart, J. Murray, S.-H. Yun, J. Svarc, S. Samsonov, E. Fielding, B. Brooks, and P. Milillo. Geodetic constraints on the 2014 Mw 6.0 South Napa earthquake. *Seism. Res. Lett.*, 86:335–343, 2015.

N. Beeler, T. Tullis, and D. Goldsby. Constitutive relationships and physical basis of fault strength due to flash heating. *J. Geophys. Res.*, 113:B01401, 2008.

J.-P. Berenger. A perfectly matched layer for the absorption of electromagnetic waves. *J. Comput. Phys.*, 114(2):185–200, 1994.

A. Bizzarri. What does control earthquake ruptures and dynamic faulting? a review of different competing mechanisms. *Pure Appl. Geophys.*, 166(5):741–776, 2009.

A. Bizzarri. How to promote earthquake ruptures: Different nucleation strategies in a dynamic model with slip-weakening friction. *Bull. Seismol. Soc. Am.*, 100 (3):923–940, 2010.

A. Bizzarri and M. Cocco. A thermal pressurization model for the spontaneous dynamic rupture propagation on a three–dimensional fault: 1. Methodological approach. *J. Geophys. Res.*, 111:B05303, 2006.

M. Bouchon. The state of stress on some faults of the San Andreas System as inferred from near-field strong motion data. *J. Geophys. Res.*, 102(B6):11731–11744, 1997.

C. Boulton, L. Yao, D. R. Faulkner, J. Townend, V. G. Toy, R. Sutherland, S. Ma, and T. Shimamoto. High-velocity frictional properties of Alpine fault rocks: Mechanical data,microstructural analysis, and implications for rupture propagation. *J. Struct. Geol.*, 97:71–92, 2017.

W. F. Brace and J. D. Byerlee. Stick slip as a mechanism for earthquakes. *Science*, 153:990–992, 1966.

B. A. Brooks, S. E. Minson, C. L. Glennie, J. M. Nevitt, T. Dawson, and R. Rubin. Buried shallow fault slip from the South Napa earthquake revealed by near-field geodesy. *Sci. Adv.*, 3(7):e1700525, 2017.

S. Bunichiro, H. Noda, and M. J. Ikari. Quasi-Dynamic 3D Modeling of the Generation and Afterslip of a Tohoku-oki Earthquake Considering Thermal Pressurization and Frictional Properties of the Shallow Plate Boundary. *Pure and Applied Geophysics*, 176:3951–3973, 2019.

J. Burjánek and J. Zahradník. Dynamic stress field of a kinematic earthquake source model with k-squared slip distribution. *Geophys. J. Int.*, 171:1082–1097, 2007.

R. Burridge. The numerical solution of certain integral equations with non-integrable kernels arising in the theory of crack propagation and elastic wave diffraction. *Phil. Trans. Roy. Soc. Lond.*, 265:353–381, 1969.

E. Caballero, A. Chounet, Z. Duputel, J. Jara, C. Twardzik, and R. Jolivet. Seismic and aseismic fault slip during the initiation phase of the 2017 Mw = 6.9 Valparaíso earthquake. *Geophys. Res. Lett.*, 48:e2020GL091916, 2021.

J. Chen, A. R. Niemeijer, and C. J. Spiers. Microphysically derived expressions for rate-and-state friction parameters, a, b, and Dc. *J. Geophys. Res.: Solid Earth*, 122:9627–9657, 2017.

M. Cocco and A. Bizzarri. On the slip-weakening behavior of rate-and-state dependent constitutive laws. *Geophys. Res. Lett.*, 29(11):GL013999, 2002.

F. Collino and Ch. Tsogka. Application of the perfectly matched absorbing layer model to the linear elastodynamic problem in anisotropic heterogeneous media. *Geophysics*, 66:294–307, 2001.

S. M. Corish, Ch. R. Bradley, and K. B. Olsen. Assessment of a nonlinear dynamic rupture inversion technique applied to a synthetic earthquake. *Bull. Seismol. Soc. Am.*, 97:901–914, 2007.

F. Cotton and O. Coutant. Dynamic stress variations due to shear faults in a plane-layered medium. *Geophys. J. Int.*, 128:676–688, 1997.

P. A. Cowie and C. H. Scholz. Growth of faults by the accumulation of seismic slip. *J. Geophys. Res.*, 97:11085–11095, 1992.

V. M. Cruz-Atienza, J. Virieux, and H. Aochi. 3D finite-difference dynamic-rupture modeling along nonplanar faults. *Geophysics*, 72(5):123–137, 2007.

Y. Cui, E. Poyraz, K. B . Olsen, J. Zhou, K. Withers, S. Callaghan, J. Larkin, C. D. Choi, A. Chourasia, Z. Shi, et al. Physics-based seismic hazard analysis on petascale heterogeneous supercomputers. In *SC '13: Proc. of the International Conf. on High Performance Computing, Networking, Storage and Analysis*, pages 1–12, 2013.

G. Cultrera, A. Cirella, E. Spagnuolo, A. Herrero, E. Tinti, and F. Pacor. Variability of kinematic source parameters and its implication on the choice of the design scenario. *Bull. Seismol. Soc. Am.*, 100(3):941–953, 2010.

T. M. Daley, B. M. Freifeld, J. Ajo-Franklin, S. Dou, R. Pevzner, V. Shulakova, et al. Field Testing of Fiber-Optic Distributed Acoustic Sensing (DAS) for Subsurface Seismic Monitoring. *Lead. Edge*, 32(6):699–706, 2013.

L. A. Dalguer and S. M. Day. Staggered-grid split-node method for spontaneous rupture simulation. *J. Geophys. Res.*, 112:B02302, 2007.

S. Das. A numerical method for determination of source time functions for general three-dimensional rupture propagation. *Geophys. J. Int.*, 62(3):591–604, 1980.

S. Das and K. Aki. A numerical study of two-dimensional spontaneous rupture propagation. *Geophys. J. R. Astr. Soc.*, 50:643–668, 1977.

S. Das and B. Kostrov. Diversity of solutions of the problem of earthquake faulting inversion; application to SH waves for the great 1989 Macquarie Ridge earthquake. *Phys. Earth Planet. Inter.*, 85(3-4):293–318, 1994.

E. G. Daub. Meet a new code: Daub finite difference. In *Presentation at the March 2016 SCEC Rupture Dynamics Code Validation Workshop*, Pomona, California, 2016.

S. M. Day. Three-dimensional finite difference simulation of fault dynamics: Rectangular faults with fixed rupture velocity. *Bull. Seismol. Soc. Am.*, 72:705–727, 1982.

S. M. Day, L. A. Dalguer, N. Lapusta, and Y. Liu. Comparison of finite difference and boundary integral solutions to three-dimensional spontaneous rupture. *J. Geophys. Res.*, 110:B12307, 2005.

J. de la Puente, J.-P. Ampuero, and M. Käser. Dynamic rupture modeling on unstructured meshes using a discontinuous Galerkin method. *J. Geophys. Res.*, 114:B10302, 2009.

S. B. DeLong, A. Donnellan, D. J. Ponti, R. S. Rubin, J. J. Lienkaemper, C. S. Prentice, T. E. Dawson, G. Seitz, D. P. Schwartz, K. W. Hudnut, C. Rosa, A. Pickering, and J. W. Parker. Tearing the terroir: Details and implications of surface rupture and deformation from the 24 August 2014 M6.0 South Napa earthquake, California. *Earth Space Sci.*, 3:416–430, 2016.

B. Delouis, D. Giardini, P. Lundgren, and Salichon. Joint inversion of InSAR, GPS, teleseismic, and strong-motion data for the spatial and temporal distribution of earthquake slip: Application to the 1999 Izmit mainshock. *Bull. Seismol. Soc. Am.*, 92:278–299, 2002.

G. Di Toro, D. L. Goldsby, and T. E. Tullis. Friction falls towards zero in quartz rock as slip velocity approaches seismic rates. *Nature*, 427:436–439, 2004.

J. H. Dieterich. Time-dependent friction as a possible mechanism for aftershocks. *J. Geophys. Res.*, 77(20):3771–3781, 1972.

J. H. Dieterich. Modeling of rock friction: 1. experimental results and constitutive equations. *J. Geophys. Res.*, 84(B5):2161– 2168, 1979.

D. S. Dreger, M.-H. Huang, A. Rodgers, T. Taira, and K. Wooddell. Kinematic finite-sourcemodel for the 24 August 2014 South Napa, California, earthquake from joint inversionof seismic, GPS, and InSAR data. *Seismol. Res. Lett.*, 86: 327–334, 2015.

E. M. Dunham and J. R. Rice. Earthquake slip between dissimilar poroelastic materials. *J. Geophys. Res.*, 113:B09304, 2008.

E. M. Dunham, D. Belanger, L. Cong, and J. E. Kozdon. Earthquake ruptures with strongly rate-weakening friction and off-fault plasticity, part 1: Planar faults. *Bull. Seismol. Soc. Am.*, 101:2296–2307, 2011.

Z. Duputel, J. Jiang, R. Jolivet, M. Simons, L. Rivera, J.-P. Ampuero, B. Riel, S. E. Owen, A. W. Moore, S. V. Samsonov, F. Ortega Culaciati, and S. E. Minson. The Iquique earthquake sequence of April 2014: Bayesian modeling accounting for prediction uncertainty. *Geophys. Res. Lett.*, 42:7949– 7957, 2015.

J. Díaz-Mojica, V. M. Cruz-Atienza, R. Madariaga, S. K. Singh, J. Tago, and A. Iglesias. Dynamic source inversion of the M6.5 intermediate-depth Zumpango earthquake in central Mexico: A parallel genetic algorithm. *J. Geophys. Res.: Solid Earth*, 119:7768–7785, 2014.

B. Erickson, J. Jiang, M. Barall, N. Lapusta, E. M. Dunham, R. Harris, L. S. Abrahams, K. L. Allison, J.-P. Ampuero, S. Barbot, et al. The community code verification exercise for simulating sequences of earthquakes and aseismic slip (SEAS). *Seismol. Res. Lett.*, 91(2A):874–890, 2020.

E. L. Evans, J. P. Loveless, and B. J. Meade. Geodetic constraints on San Francisco Bay area faultslip rates and potential seismogenic asperities on the partially creeping Hayward fault. *J. Geophys. Res. Solid Earth*, 117:B03410, 2012.

G. Festa and J. Vilotte. The Newmark scheme as velocity-stress time staggered: An efficient PML implementation for spectral element simulations of electrodynamics. *Geophys. J. Int.*, 161:789–812, 2005.

M. A. Floyd, R. J. Walters, J. R. Elliott, G. J. Funning, J. L. Svarc, J. R. Murray, A. J. Hooper, Y. Larsen, P. Marinkovic, R. Bürgmann, I. A. Johanson, and T. J. Wright. Spatial variations in fault friction related to lithology from rupture and

afterslip of the 2014 South Napa, California, earthquake. *Geophys. Res. Lett.*, 43(13):6808–6816, 2016.

C. Frohlich. *Deep Earthquakes*. Cambridge University Press, 2006.

J. I. Fukuda, K. M. Johnson, K. M. Larson, and S. I. Miyazaki. Fault friction parameters inferred from the early stages of afterslip following the 2003 Tokachi-oki earthquake. *J. Geophys.Res. Solid Earth*, 114:B04412, 2009.

E. Fukuyama and T. Mikumo. Dynamic rupture analysis: Inversion for the source process of the 1990 Izu-Oshima, Japan, earthquake. *J. Geophys. Res.*, 98:6529–6542, 1993.

P. M. Fulton, E. Brodsky, J. J. Mori, and F. M. Chester. Tohoku-Oki Fault Zone Frictional Heat Measured During IODP Expeditions 343 and 343T. *Oceanography*, 32:102–104, 2019.

A.-A. Gabriel, J.-P. Ampuero, L. A. Dalguer, and P. M. Mai. Source properties of dynamic rupture pulses with off-fault plasticity. *J. Geophys. Res.*, 118: 4117–4126, 2013.

A.-A. Gabriel, J.-P. Ampuero, L. A. Dalguer, and P. M. Mai. The transition of dynamic rupture styles in elastic media under velocity-weakening friction. *J. Geophys. Res.*, 117:B09311, 2012.

F. Gallovič. Heterogeneous Coulomb stress perturbation during earthquake cycles in a 3D rate-and-state fault model. *Geophys. Res. Lett.*, 35:L21306, 2008.

F. Gallovič and J.-P. Ampuero. A new strategy to compare inverted rupture models exploiting the eigen-structure of the inverse problem. *Seism. Res. Lett.*, 86:1679–1689, 2015.

F. Gallovič and L. Valentová. Earthquake stress drops from dynamic rupture simulations constrained by observed ground motions,. *Geophys. Res. Lett.*, 47: e2019GL08588, 2020.

F. Gallovič and J. Zahradník. Complexity of the Mw 6.3 2009 L'Aquila (Central Italy) earthquake: 1. Multiple finite-extent source inversion. *J. Geophys. Res.*, 117:B04307, 2012.

F. Gallovič, W. Imperatori, and P. M. Mai. Effects of three-dimensional crustal structure and smoothing constraint on earthquake slip inversions: case study of the Mw6.3 2009 L'Aquila earthquake. *J. Geophys. Res.*, 120:428–449, 2015.

F. Gallovič, L. Valentová, J.-P. Ampuero, and A.-A. Gabriel. Bayesian dynamic finite-fault inversion: 1. Method and synthetic test. *J. Geophys. Res.*, 124: 6949–6969, 2019a.

F. Gallovič, L. Valentová, J.-P. Ampuero, and A.-A. Gabriel. Bayesian dynamic finite-fault inversion: 2. Application to the 2016 Mw 6.2 Amatrice, Italy, earthquake. *J. Geophys. Res.*, 124:6970–6988, 2019b.

F. Gallovič, J. Zahradník, V. Plicka, E. Sokos, C. Evangelidis, I. Fountoulakis, and F. Turhan. Complex rupture dynamics on an immature fault during the 2020 Mw 6.8 Elazığ earthquake, Turkey. *Commun. Earth Environ.*, 1:40, 2020.

P. Galvez, A. Petukhin, P. Somerville, J. P. Ampuero, K. Miyakoshi, D. Peter, and K. Irikura. Multicycle simulation of strike-slip earthquake rupture for use in near-source ground-motion simulations. *Bull. Seismol. Soc. Am.*, 111: 2463–2485, 2021.

D. L. Goldsby and T. E. Tullis. Flash heating leads to low frictional strength of crustal rocks at earthquake slip rates. *Science*, 334(6053):216–218, 2011.

R. W. Graves. Simulating seismic wave propagation in 3D elastic media using staggered-grid finite differences. *Bull. Seismol. Soc. Am.*, 86(4):1091–1106, 1996.

R. W. Graymer, D. A. Ponce, R. C. Jachens, R. W. Simpson, G. A. Phelps, and C. M. Wentworth. Three-dimensional geologic map of the Hayward fault, northern California: Correlation of rock units with variations in seismicity, creep rate, and fault dip. *Geology*, 33:521–524, 2005.

R. W. Graymer, B. C. Moring, G. J. Saucedo, C. M. Wentworth, E. E. Brabb, and K. L. Knudsen. Geologic map of the San Francisco Bay region. Technical report, U.S. Geological Survey, Scientific Investigations Map 2918, 2006. URL `http://pubs.usgs.gov/sim/2006/2918/`.

M. Guatteri, P. M. Mai, and G. C. Beroza. A pseudo-dynamic approximation to dynamic rupture models for strong ground motion prediction. *Bull. Seism. Soc. Am.*, 94:2051–2063, 2004.

M. Hallo, K. Asano, and F. Gallovič. Bayesian inference and interpretation of centroid moment tensors of the 2016 Kumamoto earthquake sequence, Kyushu, Japan. *Earth, Planets and Space*, 69:134, 2017.

J. L. Hardebeck and D. R. Shelly. Aftershocks of the 2014 South Napa, California, earthquake:Complex faulting on secondary faults. *Bull. Seismol. Soc. Am.*, 106: 1100–1109, 2016.

R. Harris, M. Barall, R. Archuleta, E. Dunham, B. T. Aagaard, Jean Paul Ampuero, H. Bhat, V. Cruz-Atienza, L. Dalguer, P. Dawson, S. Day, Duan , G. Ely, Y. Kaneko, Y. Kase, N. Lapusta, Y. Liu, S. Ma, D. Oglesby, and E. Templeton. The SCEC/USGS dynamic earthquake rupture code verification exercise. *Seismol. Res. Lett.*, 80(1):119–126, 2009.

R. A. Harris. Large earthquakes and creeping faults. *Rev. Geophys.*, 55:169–198, 2017.

R. A. Harris, M. Barall, D. J. Andrews, B. Duan, S. Ma, E. M. Dunham, A.-A. Gabriel, Y. Kaneko, Y. Kase, B. T. Aagaard, et al. Verifying a computational method for predicting extreme ground motion. *Seismol. Res. Lett.*, 82 (5):638–644, 2011.

R. A. Harris, M. Barall, B. Aagaard, S. Ma, D. Roten, K. Olsen, B. Duan, D. Liu, B. Luo, K. Bai, et al. A suite of exercises for verifying dynamic earthquake rupture codes. *Seismol. Res. Lett.*, 89(3):1146–1162, 2018.

S. H. Hartzell, P. Liu, C. Mendoza, C. Ji, and K. M. Larson. Stability and Uncertainty of Finite- Fault Slip Inversions: Application to the 2004 Parkeld, California, Earthquake. *Bull. Seismol. Soc. Am.*, 97(6):1911–1934, 2007.

N. A. Haskell. Total energy and energy spectral density of elastic wave radiation from propagating faults. *Bull. Seismol. Soc. Am.*, 54(6A):1811–1841, 1964.

A. Heinecke, A. Breuer, S. Rettenberger, M. Bader, A.-A. Gabriel, C. Pelties, A. Bode, W. Barth, X.-K. Liao, K. Vaidyanathan, et al. Petascale high order dynamic rupture earthquake simulations on heterogeneous supercomputers. In *Proc. of the International Conference for High Performance Computing, Networking, Storage and Analysis SC14*, New Orleans, Louisiana, 2014.

K. Heki, S. Miyazaki, and H. Tsuji. Silent fault slip following an interplate thrust earthquake at the Japan Trench. *Nature*, 386:595–598, 1997.

G. Hillers, Y. Ben-Zion, and P. M. Mai. Seismicity on a fault controlled by rate- and state-dependent friction with spatial variations of the critical slip distance. *J. Geophys. Res.: Solid Earth*, 111:B01403, 2006.

T. Ichimura, S. Fujita, K.and Tanaka, M. Hori, L. Maddegedara, Y. Shizawa, and Kobayashi H. Physics-based urban earthquake simulation enhanced by 10.7 BlnDOF $\times$ 30 K time-step unstructured FE non-linear seismic wave simulation. In *SC14: International Conf. for High Performance Computing, Networking, Storage and Analysis*, New Orleans, Louisiana, 2014.

Y. Ida. Cohesive force across the tip of a longitudinal-shear crack and Griffith's specific surface energy. *J. Geophys. Res.*, 77(20):3796–3805, 1972.

S. Ide and M. Takeo. Determination of constitutive relations of fault slip based on seismic wave analysis. *J. Geophys. Res.*, 102(B12):27379– 27391, 1997.

A. Inbal, J. P. Ampuero, and J.-P. Avouac. Locally and remotely triggered aseismic slipon the central San Jacinto Fault near Anza, CA, from joint inversion of seismicity and strainmeter data. *J. Geophys. Res.: Solid Earth*, 122:3033–3061, 2017.

C. Ji, R. J. Archuleta, and C. Twardzik. Rupture history of 2014 Mw 6.0 South Napa earthquakeinferred from near-fault strong motion data and its impact to the practice of ground strong motion prediction. *Geophys. Res. Lett.*, 42: 2149–2156, 2015.

N. Kame, S. Fujita, M. Nakatani, and T. Kusakabe. Earthquake nucleation on faults with a revised rate- and state-dependent friction law. *Pure Appl. Geophys.*, 172:2237–2246, 2015.

Y. Kaneko and Y. Fialko. Shallow slip deficit due to large strike-slip earthquakes in dynamic rupture simulations with elasto-plastic off-fault response. *Geophys. J. Int.*, 186:1389–1403, 2011.

Y. Kaneko, N. Lapusta, and J.-P. Ampuero. Spectral-element modeling of spontaneous earthquake rupture on rate and state faults: Effect of velocity-strengthening friction at shallow depths. *J. Geophys. Res.*, 113:B0931, 2008.

M. Koller, M. Bonnet, and R. Madariaga. Modelling of dynamical crack propagation using time-domain boundary integral equations. *Wave Motion*, 16: 339–366, 1992.

D. Komatitsch, D. Michea, and G. Erlebacher. Porting a high-order finite-element earthquake modeling application to nvidia graphic cards using cuda. *J. Parallel Distr. Comput.*, 69(5):451–460, 2009.

D. Komatitsch, P. Le Loher, D. Michéa, G. Erlebacher, and D. Göddeke. Accelerating spectral-element and finite-difference wave propagation algorithms using a cluster of GPU graphics cards. In *Workshop Défis Actuels De La Modélisation Électromagnétique: Gestion De La Complexité, Multi-Échelle, Multi-Physique, Gestion Des Incertitudes, Statistiques*, Saint Malo, France, 2010. in French.

F. Kostka. *Dynamic models of the earthquake source.* Ph. D. thesis, Charles University, 2022.

F. Kostka, J. Zahradník, E. Sokos, and F. Gallovič. Assessing the role of selected constraintsin Bayesian dynamic source inversion: Application to the 2017 Mw 6.3 Lesvos earthquake. *Geophys. J. Int.*, 228:711–727, 2022.

B. Kostrov. Unsteady propagation of longitudinal shear cracks. *J. Appl. Math. Mech.*, 30(6):1241–1248, 1966.

B. V. Kostrov. Selfsimilar problems of propagation of shear cracks. *J. Appl. Math. Mech.*, 28(5):1077–1087, 1964.

L. Krischer, Y. A. Aiman, T. Bartholomaus, S. Donner, M. van Driel, K. Duru, K. Garina, K. Gessele, T. Gunawan, S. Hable, et al. Seismo-Live: An educational online library of Jupyter notebooks for seismology. *Seismol. Res. Lett.*, 89(6):2413–2419, 2018.

J. Kristek, P. Moczo, and M. Galis. A brief summary of some PML formulations and discretizations for the velocity-stress equation of seismic motion. *Studia Geophysica et Geodaetica*, 53:459–474, 2009.

J. Langbein, J. R. Murray, and H. A. Snyder. Coseismic and initial postseismic deformationfrom the 2004 Parkfield, California, earthquake, observed by Global Positioning System,electronic distance meter, creepmeters, and borehole strainmeters. *Bull. Seismol. Soc. Am.*, 96:S304–S320, 2006.

R. Langenheim, R. Graymer, R. Jachens, and D. Mclaughlin. Geophysical framework of the northern san francisco bay region, california. *Geosphere*, 6:594–620, 2010.

N. Lapusta, J. R. Rice, Y. Ben-Zion, and G. Zheng. Elastodynamic analysis for slow tectonic loading with spontaneous rupture episodes on faults with rate- and state-dependent friction. *J. Geophys. Res.*, 105:23765–23789, 2000.

N. Lapusta et al. Modeling earthquake source processes: from tectonics to dynamic rupture. Technical report, National Science Foundation (NSF), Southern California Science Center (SCEC),Seismological Laboratory at the California Institute of Technology, 2019.

S. Latour, Ch. Voisin, F. Renard, E. Larose, S. Catheline, and M. Campillo. Effect of fault heterogeneity on rupture dynamics: An experimental approach using ultrafast ultrasonic imaging: Experimental study of rupture dynamics. *J. Geophys. Res.: Solid Earth*, 118:5888– 5902, 2013.

A. Levander. Fourth-order finite-difference P-SV seismograms. *Geophysics*, 53: 1425–1436, 1988.

J. J. Lienkaemper, S. B. DeLong, C. J. Domrose, and C. M. Rosa. Afterslip behavior following the 2014 M 6.0 South Napa earthquake with implications for afterslip forecastingon other seismogenic faults. *Seism. Res. Lett.*, 87:609–619, 2016.

X. Liu and W. Xu. Logarithmic model joint inversion method for coseismic and postseismic slip: Application to the 2017 Mw 7.3 Sarpol Zahāb earthquake, Iran. *J. Geophys. Res.: Solid Earth*, 124:12034–12052, 2019.

R. B. Lohman, M. Simons, and B. Savage. Location and mechanism of the Little Skull Mountain earthquake as constrained by satellite radar interferometry and seismic waveform modeling. *J. Geophys. Res.*, 107:B6, 2002.

S. Ma, D. A. Lockner, D. E. Moore, R. Summers, and J. D. Byerlee. Frictional strength and velocity-dependence of serpentine gouges under hydrothermal conditions and their seismogeological implications. *Dizhen Dizhi*, 19:171–178, 1997.

R. Madariaga. Dynamics of an expanding circular fault. *Bull. Seismol. Soc. Am.*, 66:639–666, 1976.

R. Madariaga, K. Olsen, and R. Archuleta. Modeling dynamic rupture in a 3D earthquake fault model. *Bull. Seismol. Soc. Am.*, 88(5):1182–1197, 1998.

P. M. Mai, D. Schorlemmer, M. Page, J.-P. Ampuero, K. Asano, M. Causse, S. Custodio, W. Fan, G. Festa, M. Galis, F. Gallovic, W. Imperatori, M. Käser, D. Malytskyy, R. Okuwaki, F. Pollitz, L. Passone, H. N. T. Razafindrakoto, H. Sekiguchi, S. G. Song, S. N. Somala, K. K. S. Thingbaijam, C. Twardzik, M. van Driel, J. C. Vyas, R. Wang, Y. Yagi, and O. Zielke. The Earthquake-Source Inversion Validation (SIV) Project. *Seismol. Res. Let.*, 87(3):690–708, 2016.

C. Marone and C. H. Scholz. The depth of seismic faulting and the upper transition from stable to unstable slip regimes. *Geophys. Res. Lett.*, 15:621–624, 1988.

Ch. Marone, C. Scholz, and R. Bilham. On the mechanics of earthquake afterslip. *J. Geophys. Res.*, 96:8441–8452, 1991.

F. S. McFarland, J. J. Lienkaemper, and S. J. Caskey. Data from theodolite measurements of creep rates on San Francisco Bay Region faults, California: 1979–2013. Technical report, U.S. Geological Survey Open-File Report 2009, 2015.

G. C. McLaskey and B. D. Kilgore. Foreshocks during the nucleation of stick-slip instability. *J. Geophys. Res.*, 118:2982–2997, 2013.

T. I. Melbourne, F. H. Webb, J. M. Stock, and C. Reigber. Rapid postseismic transients in subduction zones from continuous GPS. *J. Geophys. Res.*, 107: B10, 2002.

D. Melgar, J. Geng, B. W. Crowell, J. S. Haase, Y. Bock, W. C. Hammond, and R. M. Allen. Seismogeodesy of the 2014 Mw6. 1 Napa earthquake, California: Rapid responseand modeling of fast rupture on a dipping strike-slip fault. *J. Geophys. Res.: Solid Earth*, 120:5013–5033, 2015.

D. Michéa and D. Komatitsch. Accelerating a three-dimensional finite-difference wave propagation code using GPU graphics cards. *Geophys. J. Int.*, 182: 389–402, 2010.

T. Mikumo and T. Miyatake. Dynamical rupture process on a three-dimensional fault with non-uniform frictions and near-field seismic waves. *Geophys. J. Int.*, 54(2):417–443, 1978.

A. Mirwald, V. M. Cruz-Atienza, J. Díaz-Mojica, A. Iglesias, S. K. Singh, C. Villafuerte, and J. Tago. The 19 September 2017 (Mw 7.1) intermediate-depth Mexican earthquake: A slow and energetically inefficient deadly shock. *Geophys. Res. Lett.*, 46:2054–2064, 2019.

P. Moczo, J. Robertsson, and L. Eisner. The finite-difference time-domain method for modeling of seismic wave propagation. *Advances in Geophysics*, 48:421–516, 2007.

D. Monelli and M. P. Mai. Bayesian inference of kinematic earthquake rupture parameters through fitting of strong motion data. *Geophys. J. Int.*, 173:220–232, 2008.

D. Monelli, M. P. Mai, S. Jónsson, and D. Giardini. Bayesian imaging of the 2000 Western Tottori (Japan) earthquake through tting of strong motion and GPS data. *Geophys. J. Int.*, 176(1):135–150, 2009.

D. E. Moore. Relationships between sliding behavior and internal geometry of laboratory fault zones and some creeping and locked strike-slip faults of California. *Tectonophysics*, 211:305–316, 1992.

J. Murray and J. Langbein. Slip on the San Andreas Fault at Parkfield, California, over two earthquake cycles, and the implications for seismic hazard. *Bull. Seism. Soc. Am.*, 96:S283–S303, 2006.

K. Nagata, M. Nakatani, and S. Yoshida. A revised rate-and-state-dependent friction law obtained by constraining constitutive and evolution laws separately with laboratory data. *J. Geophys. Res.*, 117:B02314, 2012.

S. Nielsen, G. Di Toro, T. Hirose, and T. Shimamoto. Frictional melt and seismic slip. *J. Geophys. Res.*, 113(B01308), 2008.

H. Noda and N. Lapusta. Stable creeping fault segments can become destructive as a result of dynamic weakening. *Nature*, 493:518–521, 2013.

H. Noda, N. Lapusta, and H. Kanamori. Comparison of average stress drop measures for ruptures with heterogeneous stress change and implications for earthquake physics. *Geophys. J. Int.*, 106(B11):26467–26482, 2013.

D. Oglesby, R. Archuleta, and S. Nielsen. Earthquakes on dipping faults: The effects of broken symmetry. *Science*, 280:1055–1059, 1998.

Y. Okada. Surface deformation due to shear and tensile faults in a half-space. *Bull. Seism.Soc. Am.*, 75:1135–1154, 1985.

K. Okubo, H. S. Bhat, E. Rougier, S. Marty, A. Schubnel, Z. Lei, E. E. Knight, and Y. Klinger. Dynamics, radiation, and overall energy budget of earthquake rupture with coseismic off-fault damage. *J. Geophys. Res.: Solid Earth*, 124: 11771–11801, 2019.

C. Pelties, J. De la Puente, J.-P. Ampuero, G. B. Brietzke, and M. Käser. Three-dimensional dynamic rupture simulation with a high-order discontinuous Galerkin method on unstructured tetra-hedral meshes. *J. Geophys. Res.*, 117:B02309, 2012.

C. Pelties, A.-A. Gabriel, and J.-P. Ampuero. Verification of an ADER-DG method for complex dynamic rupture problems. *Geosci. Model Dev.*, 7(3): 847–866, 2014.

H. Perfettini and J.-P. Ampuero. Dynamics of a velocity strengthening fault region: Implications for slow earthquakes and postseismic slip. *J. Geophys. Res.*, 113:B09411, 2008.

H. Perfettini and J.-P. Avouac. Postseismic relaxation driven by brittle creep: A possible mechanism to reconcile geodetic measurements and the decay rate of aftershocks,application to the Chi-Chi earthquake, Taiwan. *J. Geophys. Res.*, 109:B02304, 2004.

H. Perfettini and J. P. Avouac. The seismic cycle in the area of the 2011 Mw9.0 Tohoku-Oki earthquake. *Journ. Geophys. Res.: Solid Earth*, 119(5):4469–4515, 2014.

H. Perfettini, J. Schmittbuhl, and A. Cochard. Shear and normal load perturbations on a two-dimensional continuous fault: 1. Static triggering. *J. Geophys. Res.*, 108:2408, 2003.

S. Peyrat and K. B. Olsen. Which dynamic rupture parameters can be estimated from strong ground motion and geodetic data? *Pure Appl. Geophys.*, 161: 2155–2169, 2004.

S. Peyrat, K. Olsen, and R. Madariaga. Dynamic modeling of the 1992 Landers earthquake. *J. Geophys. Res.*, 193:1691–1712, 2001.

A. Piatanesi, E. Tinti, M. Cocco, and E. Fukuyama. The dependence of traction evolution on the earthquake source time function adopted in kinematic rupture models. *Geophys. Res. Lett.*, 31:L04609, 2004.

A. Pitarka. Rupture dynamics simulations of shallow crustal earthquakes on reverse slip faults. Technical report, Lawrence Livermore National Laboratory, 2020.

J. Premus, F. Gallovič, L. Hanyk, and A.-A. Gabriel. FD3D_TSN: A fast and simple code for dynamic rupture simulations with GPU acceleration. *Seism. Res. Lett.*, 91:2881–2889, 2020.

J. Premus, F. Gallovič, and J.-P. Ampuero. Bridging time scales of faulting: From coseismic to postseismic slip of the Mw 6.0 2014 South Napa, California earthquake. *Sci. Adv.*, 8:eabq2536, 2022.

S. Preuss, R. Herrendörfer, T. Gerya, J.-P. Ampuero, and Y. van Dinther. Seismic and aseismic fault growth lead to different fault orientations. *J. Geophys. Res.: Solid Earth*, 124(8):8867–8889, 2019.

T. Ragon, A. Sladen, Q. Bletery, M. Vergnolle, O. Cavalié, A. Avallone, J. Balestra, and B. Delouis. Joint inversion of coseismic and early postseismic slip to optimize the information content in geodetic data: Application to the 2009 Mw6.3 L'Aquila earthquake, Central Italy. *J. Geophys. Res.: Solid Earth*, 124:10522–10543, 2019.

J. R. Rice. Spatio-temporal complexity of slip on a fault. *J. Geophys. Res.*, 98: 9885–9907, 1993.

J. R. Rice. Heating and weakening of faults during earthquake slip. *J. Geophys. Res.: Solid Earth*, 111:B05311, 2006.

J. R. Rice and Y. Ben-Zion. Slip complexity in earthquake fault models. *Proc. Natl. Acad. Sci. U.S.A.*, 93:3811–3818, 1996.

J. R. Rice and S. T. Tse. Dynamic motion of a single degree of freedom system following a rate and state dependent friction law. *J. Geophys. Res.*, 91:B1, 1986.

J. Ripperger, J.-P. Ampuero, P. M. Mai, and D. Giardini. Earthquake source characteristics from dynamic rupture with constrained stochastic fault stress. *J. Geophys. Res.*, 112:B4, 2007.

J. O. A. Robertsson. A numerical free-surface condition for elastic/viscoelastic finite-difference modeling in the presence of topography. *Geophysics*, 61(6): 1921–1934, 1996.

A. J. Rodgers, R. Pankajakshan, B. Sjogreen, A. Petersson, and A. Pitarka. Hayward fault earthquake ground motion simulations on GPU-accelerated platforms with SW4-RAJA. In *Presentation at 2019 SCEC Annual Meeting*, Palm Springs, California, 2019.

O. Rojas, E. M. Dunham, S. M. Day, L. A. Dalguer, and J. E. Castillo. Finite difference modelling of rupture propagation with strong velocity-weakening friction. *Geophys. J. Int.*, 179(3):1831–1858, 2009.

D. Roten, K. B. Olsen, S. M. Day, Y. Cui, and D. Fäh. Expected seismic shaking in los angeles reduced by san andreas fault zone plasticity. *Geophys. Res. Lett.*, 41:2769–2777, 2014.

D. Roten, Y. Cui, S. M. Olsen, K. B. Day, W. H. Withers, K. Savran, P. Wang, and D. Mu. High-frequency nonlinear earthquake simulations on petascale heterogeneous supercomputers. In *SC '16: Proc. of the International Conf. for High Performance Computing, Networking, Storage and Analysis*, page 957–968, Salt Lake, Utah, 2016.

V. Rubino, A. Rosakis, and N. Lapusta. Understanding dynamic friction through spontaneously evolving laboratory earthquakes. *Nat. Commun.*, 8:15991, 2017.

A. Ruina. Slip instability and state variable friction laws. *J. Geophys. Res.*, 881: 10359– 10370, 1983.

S. Ruiz and R. Madariaga. Kinematic and Dynamic Inversion of the 2008 Northern Iwate Earthquake. *Bull. Seismol. Soc. Am.*, 103(2A):694–708, 2013.

M. Sambridge. A parallel tempering algorithm for probabilistic sampling and multimodal optimization. *Geophys. J. Int.*, 196:357–374, 2013.

M. Sambridge and K. Mosegaard. Monte Carlo methods in geophysical inverse problems. *Rev. Geophys.*, 40:3, 2002.

C. G. Sammis and Y. Ben-Zion. Mechanics of grain-size reduction in fault zones. *J. Geophys. Res.*, 113:B02306, 2008.

C. Scholz. Earthquakes and friction laws. *Nature*, 391:37–42, 1998.

C. Scholz. *The Mechanics of Earthquakes and Faulting*. Cambridge Univ. Press„ 2. edition, 2012.

G. Shao and C. Ji. What the exercise of the SPICE source inversion validation BlindTest 1 did not tell you. *Geophys. J. Int.*, 189(1):569–590, 2012.

Z. Shi and S. M. Day. Rupture dynamics and ground motion from 3-D rough-fault simulations. *J. Geophys. Res.: Solid Earth*, 118(3):1122–1141, 2013.

R. H. Sibson. Thickness of the seismic slip zone. *Bull. Seism.Soc. Am.*, 93(3): 1169–1178, 2003.

S. W. Smith and M. Wyss. Displacement on the San Andreas fault subsequent to the 1966 Parkfield earthquake. *Bull. Seismol. Soc. Am.*, 58:1955–1973, 1968.

P. Spudich and D. P. Miller. Seismic site effects and the spatial interpolation of earthquake seismograms: Results using aftershocks of the 1986 North Palm Springs, California, earthquake. *Bull. Seismol. Soc. Am.*, 80:1504–1532, 1990.

C. Stidham, M. Antolik, D. Dreger, S. Larsen, and B. Romanowicz. Three-dimensional structure influences on the strong-motion wavefield of the 1989 Loma Prieta earthquake. *Bull. Seismol. Soc. Am.*, 89:1184–1202, 1999.

D. Storchak, J. Harris, L. Brown, K. Lieser, B. Shumba, and D. Di Giacomo. Rebuild of the Bulletin of the International Seismological Centre (ISC)—part 2: 1980–2010. *Geosci. Lett.*, 7, 2020.

J. Tago, V. M. Cruz-Atienza, J. Virieux, V. Etienne, and F. J. Sánchez-Sesma. A 3D hp-adaptive discontinuous Galerkin method for modeling earthquake dynamics. *J. Geophys. Res.*, 117:B09312, 2012.

E. Tinti, P. Spudich, and M. Cocco. Earthquake fracture energy inferred from kinematic rupture models on extended faults. *J. Geophys. Res.*, 110:B12303, 2005.

E. Tinti, E. Casarotti, T. Ulrich, T. Taufiqurrahman, D. Li, and A.-A. Gabriel. Constraining families of dynamic models using geological, geodetic and strong ground motion data: The Mw 6.5, October 30th, 2016, Norcia earthquake, Italy. *Earth Planet. Sci Lett.*, 576:117237, 2021.

A. Tsutsumi and T. Shimamoto. High-velocity frictional properties of gabbro. *Geophys. Res. Lett.*, 24:699–702, 1997.

C. Twardzik, S. Das, and R. Madariaga. Inversion for the physical parameters that control the source dynamics of the 2004 Parkfield earthquake. *J. Geophys. Res.: Solid Earth*, 119:1205–1220, 2014.

C. Twardzik, M. Vergnolle, A. Sladen, and A. Avallone. Unravelling the contribution of early postseismic deformation using sub-daily GNSS positioning. *Sci. Rep.*, 9:1775, 2019.

C. Twardzik, M. Vergnolle, A. Sladen, and L. L. Tsang. Very early identification of a bimodal frictional behavior during the post-seismic phase of the 2015 Mw 8.3 Illapel, Chile, earthquake. *Solid Earth*, 12:2523–2537, 2021.

T. Ulrich, A.-A. Gabriel, J.-P. Ampuero, and W. Xu. Dynamic viability of the 2016 Mw 7.8 Kaikuoura earthquake cascade on weak crustal faults. *Nat. Comm.*, 10:1213, 2019.

C. Uphoff, S. Rettenberger, M. Bader, E. Madden, T. Ulrich, S. Wollherr, and A.-A. Gabriel. Extreme scale multi-physics simulations of the tsunamigenic 2004 Sumatra megathrust earthquake. In *SC '17: Proc. of the International Conference for High Performance Computing, Networking, Storage and Analysis*, Denver, Colorado, 2017.

M. Vallée and M. Bouchon. Imaging coseismic rupture in far field by slip patches. *Geophys. J. Int.*, 156(3):615–630, 2004.

R. Viesca and D. Garagash. Ubiquitous weakening of faults due to thermal pressurization. *Nat. Geosci.*, 8:875–879, 2015.

D. J. Wald, T. H. Heaton, and K. W. Hudnut. The slip history of the 1994 Northridge, California, earthquake determined from strong-motion, teleseismic, GPS, and leveling data. *Bull. Seismol. Soc. Am.*, 86(1B):S49–S70, 1996.

S. Wei, S. Barbot, R. Graves, J. J. Lienkaemper, T. Wang, K. Hudnut, Y. Fu, and D. Helmberger. The 2014 Mw 6.1 South Napa Earthquake: A unilateral rupture with shallow asperityand rapid afterslip. *Seism. Res. Lett.*, 86:344–354, 2015.

J. R. Wesling and K. L. Hanson. Mapping of the West Napa Fault Zone for input into the northern California Quaternary fault database. Technical report, U.S. Geological Survey Open File Report 05HQAG0002, 2008.

S. Wollherr, A.-A. Gabriel, and C. Uphoff. Off-fault plasticity in three-dimensional dynamic rupture simulations using a modal Discontinuous Galerkin method on unstructured meshes: implementation, verification and application. *Geophys. J. Int.*, 214(3):1556–1584, 2018.

S. Wollherr, A.-A. Gabriel, and P. M. Mai. Landers 1992 "reloaded": Integrative dynamic earthquake rupture modeling. *J. Geophys. Res.*, 124:6666–6702, 2019.

T. Yamashita. Generation of microcracks by dynamic shear rupture and its effects on rupture growth and elastic wave radiation. *Geophys. J. Int.*, 143(2):395–406, 2000.

A. Z. Zambom and R. Dias. A review of kernel density estimation with applications to econometrics. *Int. Econ. Rev.*, 5:20–42, 2013.

J. Zhou, Y. Cui, E. Poyraz, D. J. Choi, and C. C. Guest. Multi-GPU implementation of a 3D finite difference time domain earthquake code on heterogeneous supercomputers. *Procedia Comput. Sci.*, 18:1255–1264, 2013.

List of publications

1. [Premus et al., 2020]: J. Premus, F. Gallovič, L. Hanyk, and A.-A. Gabriel. FD3D_TSN: A fast and simple ode for dynamic rupture simulations with GPU cceleration. *Seism. Res. Lett.*, 1:2881–2889, 2020.

2. [Premus et al., 2022]: J. Premus, F. Gallovič, and J.-P. Ampuero. Bridging time scales of faulting: From coseismic to postseismic slip of the Mw 6.0 2014 South Napa, California earthquake. *Sci. Adv.*, 8:eabq2536, 2022.